

FILE COPY

Q

NAVAL POSTGRADUATE SCHOOL

Monterey, California

AD-A208 462



DTIC
ELECTE
JUN 06 1989
S D^{CG} D THESIS

EFFECT OF HEATING RATE TO TEST TEMPERATURE
ON SUPERPLASTIC RESPONSE IN AN
Al-8%Mg-1%Li-0.2%Zr ALLOY

by

Duncan O'Mara

March 1989

Thesis Advisor: T.R. McNelley

Approved for public release; distribution is unlimited

' 89 6 05 124

REPORT DOCUMENTATION PAGE

1a. REPORT SECURITY CLASSIFICATION UNCLASSIFIED		1b. RESTRICTIVE MARKINGS	
2a. SECURITY CLASSIFICATION AUTHORITY		3. DISTRIBUTION/AVAILABILITY OF REPORT Approved for public release; distribution is unlimited	
2b. DECLASSIFICATION/DOWNGRADING SCHEDULE			
4 PERFORMING ORGANIZATION REPORT NUMBER(S)		5 MONITORING ORGANIZATION REPORT NUMBER(S)	
6a. NAME OF PERFORMING ORGANIZATION Naval Postgraduate School	6b OFFICE SYMBOL 67	7a. NAME OF MONITORING ORGANIZATION Naval Postgraduate School	
6c. ADDRESS (City, State, and ZIP Code) Monterey, California 93943-5000		7b. ADDRESS (City, State, and ZIP Code) Monterey, California 93943-5000	
8a. NAME OF FUNDING SPONSORING ORGANIZATION	8b OFFICE SYMBOL (if applicable)	9. PROCUREMENT INSTRUMENT IDENTIFICATION NUMBER	
8c. ADDRESS (City, State, and ZIP Code)		10. SOURCE OF FUNDING NUMBERS	
		PROGRAM ELEMENT NO.	PROJECT NO.
		TASK NO.	WORK UNIT ACCESSION NO.
11. TITLE (Include Security Classification) EFFECT OF HEATING RATE TO TEST TEMPERATURE ON SUPERPLASTIC RESPONSE IN AN Al-8%Mg-1%Li-0.2%Zr ALLOY			
12. PERSONAL AUTHOR(S) Duncan F. O'Mara			
13a. TYPE OF REPORT Master's Thesis	13b. TIME COVERED FROM _____ TO _____	14. DATE OF REPORT (Year, Month, Day) 1989, March	15. PAGE COUNT 152
16. SUPPLEMENTARY NOTATION The views expressed in this thesis are those of the author and do not reflect the official policy or position of the Department of Defense or the U.S. Government.			
17. COSATI CODES		18. SUBJECT TERMS (Continue on reverse if necessary and identify by block number) Heating Rate Studies; Aluminum-Magnesium-Lithium Alloys; Superplastic Response (JES)	
19. ABSTRACT (Continue on reverse if necessary and identify by block number) <p>The effect of heating rate to tension test temperature on superplastic response in an Al-8%Mg-1%Li-0.2%Zr alloy was studied. A thermomechanical process (TMP) was used that involved warm rolling with controlled reheating between rolling passes. During the TMP, microstructural evolution was controlled by a continuous reaction (CRX). Previous work has shown that grain sizes as fine as 1 micron can be obtained with superplastic ductilities in excess of 1000% at 300°C and a strain rate of 1.7x10⁻² s⁻¹. In this work, superplastic response was studied using five heating rates, ranging from 7.1x10⁻³ °C/s to 2.4x10⁻¹ °C/s, following TMP. Heating rates greater than 10°C/s resulted in a discontinuous reaction (DRX) with a likely coarsening of grain size. Conversely, high ductilities and enhancement of superplasticity resulted from slower heating rates (<1°C/s) that facilitated recovery and CRX in a microstructure already highly refined by CRX during the TMP.</p>			
20. DISTRIBUTION/AVAILABILITY OF ABSTRACT <input checked="" type="checkbox"/> UNCLASSIFIED/UNLIMITED <input type="checkbox"/> SAME AS RPT <input type="checkbox"/> DTIC USERS		21. ABSTRACT SECURITY CLASSIFICATION Unclassified	
22a. NAME OF RESPONSIBLE INDIVIDUAL F. of. T.R. McNelley		22b. TELEPHONE (Include Area Code) (408) 646-2589	22c. OFFICE SYMBOL Code 69MC

Approved for public release; distribution is unlimited

Effect of Heating Rate to Test Temperature
on Superplastic Response in an
Al-8%Mg-1%Li-0.2%Zr Alloy

by

Duncan F. O'Mara
Lieutenant, United States Navy
B.S., Cornell University, 1972

Submitted in partial fulfillment of the
requirements for the degree of

MASTER OF SCIENCE IN MECHANICAL ENGINEERING

from the

NAVAL POSTGRADUATE SCHOOL
March 1989

Author:

Duncan F. O'Mara
Duncan F. O'Mara

Approved by:

Terry R. McNelley
Terry R. McNelley, Thesis Advisor

Anthony J. Healey
Anthony J. Healey, Chairman,
Department of Mechanical Engineering

Gordon E. Schacher
Gordon E. Schacher,
Dean of Science and Engineering

ABSTRACT

The effect of heating rate to tension test temperature on superplastic response in an Al-8%Mg-1%Li-0.2%Zr alloy was studied. A thermomechanical process (TMP) was used that involved warm rolling with controlled reheating between rolling passes. During the TMP, microstructural evolution was controlled by a continuous reaction (CRX). Previous work has shown that grain sizes as fine as 1 micron can be obtained with superplastic ductilities in excess of 1000% at 300°C and a strain rate of $1.7 \times 10^{-2} \text{ s}^{-1}$. In this work, superplastic response was studied using five heating rates, ranging from $7.1 \times 10^{-3} \text{ }^{\circ}\text{C/s}$ to $2.4 \times 10^{+1} \text{ }^{\circ}\text{C/s}$, following TMP. Heating rates greater than $10 \text{ }^{\circ}\text{C/s}$ resulted in a discontinuous reaction (DRX) with a likely coarsening of grain size. Conversely, high ductilities and enhancement of superplasticity resulted from slower heating rates ($<1 \text{ }^{\circ}\text{C/s}$) that facilitated recovery and CRX in a microstructure already highly refined by CRX during the TMP.



Accesion For	
NTIS	CRA&I <input checked="" type="checkbox"/>
DTIC	TAB <input type="checkbox"/>
Unannounced <input type="checkbox"/>	
Justification _____	
By _____	
Distribution / _____	
Availability Codes	
Dist	Avail and/or Special
A-1	

TABLE OF CONTENTS

I.	INTRODUCTION -----	1
	A. ALLOY DEVELOPMENT -----	1
	B. SUPERPLASTIC FORMING -----	4
	C. NPS RESEARCH -----	6
II.	BACKGROUND -----	9
	A. ALLOY ELEMENTS -----	9
	B. SUPERPLASTICITY -----	18
	C. GRAIN REFINEMENT BY THERMOMECHANICAL PROCESSING -----	26
	D. COMPETITION BETWEEN CRX AND DRX -----	33
	E. CURRENT RESEARCH -----	48
III.	EXPERIMENTAL -----	50
	A. MATERIAL PROCESSING -----	50
	B. ELEVATED TEMPERATURE TESTING -----	56
	C. TENSILE TESTING DATA REDUCTION -----	58
	D. HEATING RATE TO TEST TEMPERATURE -----	60
	E. EXPERIMENTAL DESIGN -----	68
	F. STATISTICAL ANALYSIS -----	76
IV.	RESULTS -----	78
	A. HEATING RATES -----	78
	B. TENSILE RESPONSE -----	86
V.	DISCUSSION -----	103
	A. HEATING RATE AND COMBINED REACTIONS -----	105
	B. ADDITIONAL CONSIDERATIONS -----	110

VI. CONCLUSIONS -----	111
VII. RECOMMENDATIONS -----	112
APPENDIX A: COMPUTER PROGRAM FOR DATA REDUCTION -----	113
APPENDIX B: HEATING RATE CURVE DATA -----	114
APPENDIX C: PHASE I TRUE STRESS-STRAIN DATA -----	122
LIST OF REFERENCES -----	135
INITIAL DISTRIBUTION LIST -----	141

LIST OF TABLES

3.1	SUMMARY OF ROLLING HISTORY -----	55
3.2	PHASE I EXPERIMENTAL MATRIX -----	70
3.3	PHASE II EXPERIMENTAL MATRIX -----	71
3.4	PHASE III EXPERIMENTAL MATRIX -----	73
B.1	10^{-1} °C/s HEATING RATE DATA -----	114
B.2	10^{-3} °C/s HEATING RATE DATA -----	115
B.3	10^{-2} °C/s HEATING RATE DATA -----	116
B.4	10^0 °C/s HEATING RATE DATA FOR III/2/A -----	117
B.5	10^{+1} °C/s HEATING RATE DATA -----	118
B.6	PHASE I MECHANICAL PROPERTIES DATA -----	119
B.7	PHASE II MECHANICAL PROPERTIES DATA -----	120
B.8	PHASE III MECHANICAL PROPERTIES DATA -----	121
C.1	FLOW STRESS DATA TAKEN AT 0.1 TRUE STRAIN -----	125
C.2	REDUCED DATA FOR SAMPLE I/1/A -----	126
C.3	REDUCED DATA FOR SAMPLE I/2/A -----	127
C.4	REDUCED DATA FOR SAMPLE I/3/A -----	128
C.5	REDUCED DATA FOR SAMPLE I/4/A -----	129
C.6	REDUCED DATA FOR SAMPLE I/5/B -----	130
C.7	REDUCED DATA FOR SAMPLE I/6/A -----	131
C.8	REDUCED DATA FOR SAMPLE I/7/A -----	132
C.9	REDUCED DATA FOR SAMPLE I/8/B -----	133
C.10	REDUCED DATA FOR SAMPLE I/9/A -----	134

LIST OF FIGURES

2.1	Aluminum-Magnesium Binary Phase Diagram -----	10
2.2	Aluminum-Lithium Binary Phase Diagram -----	13
2.3	Aluminum-Zirconium Binary Phase Diagram -----	14
2.4	TMP Using DRX for Grain Refinement -----	28
2.5	TMP for Grain Refinement Using CRX -----	31
2.6	Influence of Concentration and Temperature Upon Recrystallization Kinetics in a Deformed, Super-saturated Solid Solution Al-Mg System. Zone I: DRX Only. Zone II: DRX Sequentially Followed by Precipitation. Zone III: Simultaneous DRX and Precipitation Zone IV: CRX Dominates -----	35
2.7	Interaction of Driving Forces and Retarding Forces During Isothermal Aging, Resulting in Sequence of Simultaneous Combined Reactions -----	40
2.8	Time-Temperature-Reaction Diagram for Al-8%Mg-1%Li-0.2%Zr Alloy -----	43
2.9	Transition from DRX to CRX as a Function of True Rolling Strain -----	47
3.1	Billet Geometry After Upset Forging -----	52
3.2	Tensile Testing Sample Geometry -----	57
3.3	Phase IV Sample Layout for Fabrication from Block 1, Part 2, and Heating Rates Used for Each Sample During Testing -----	75
4.1	Standardized NPS Heating Rate (10^{-1} °C/s) -----	79
4.2	Standardized Heating Rate (10^{-3} °C/s) -----	80
4.3	Standardized Heating Rate (10^{-2} °C/s) -----	81
4.4	Standardized Heating Rate (10^0 °C/s) -----	82
4.5	Standardized Heating Rate (10^{+1} °C/s) -----	83

4.6	Ductility vs Strain Rates at a Nominal 10^{-1} °C/s; Data Obtained from Munro -----	87
4.7	Heating Rates Used in Phase I -----	88
4.8	Phase I Ductility vs Strain Rate Using Two Heating Rates That Differ by Four Orders of Magnitude. All Samples Prepared by Munro -----	89
4.9	Ductility vs Strain Rate Using Three Heating Rates That are Separated by Two Orders of Magnitude. Data Obtained from Munro and Phase I Data. All Samples Prepared by Munro -----	91
4.10	Ductility vs Strain Rate Using Three Heating Rates Separated by Two Orders of Magnitude. Data Obtained from Munro and Phase I. All Samples Prepared by Munro -----	92
4.11	Phase II Ductility vs Thickness of Sample Gauge Using Four Different Heating Rates. Strain Rate Used is $6.67E-3$ s ⁻¹ . Samples Fabricated from Block 2 (see Table 3.1) -----	95
4.12	Phase III Ductility Versus Heating Rates for Al-8%Mg-1%Li-0.2%Zr Alloy, with Sample Gauge Thickness Noted. Strain Rate Used is $6.67E-3$ /s. Samples Fabricated from Block 1, Part 1 (see Table 3.1). DRX Threshold for 7xxx Aluminum Indicated as 5 °C/s, from Bampton, et al., Who Also Report Rapid Grain Growth for Heating Rates Lower Than 1 °C/s -----	97
4.13	Phase IV Ductility as a Function of Thickness of Sample Gauge and Position of Sample, Rela- tive to its Origin in the Rolled Parent Metal. When Comparing within a Row, True Isothermal Conditions Exist. Samples were Fabricated from Block 1, Part 2 (see Table 3.1) -----	99
4.14	Phase IV Ductility as a Function of Heating Rate and Position of Sample, Relative to its Origin in the Rolled Parent Metal. When Comparing within a Row, True Isothermal Conditions Exist. Samples were Fabricated from Block 1, Part 2 (see Table 3.1) -----	100
5.1	Four Key Heating Rates Used in Tensile Testing ---	106

5.2	Time-Temperature-Reaction Diagram (Schematic) -----	107
5.3	T-T-R Diagram with Heating Rate Curves Super-imposed. T-T-R Curves are Schematic -----	109
C.1	Phase I True Stress vs True Strain at a Heating Rate of 2.4 (10^{+1}) °C/s -----	122
C.2	Phase I True Stress vs True Strain at a Heating Rate of 1.2 (10^{-1}) °C/s -----	123
C.3	Phase I True Stress vs True Strain at a Heating Rate of 7.1 (10^{-3}) °C/s -----	124

I. INTRODUCTION

A. ALLOY DEVELOPMENT

Since the development of commercial production methods in 1886, aluminum has been used in applications requiring good fabrication characteristics and a high strength-to-weight ratio. When alloyed and strengthened by the various methods available, one can produce aluminum alloys that are 30 times stronger than pure aluminum, and one third the weight of steel. The high energy costs required to produce aluminum from its ore (bauxite) have made this metal economically feasible only in those industries that place a premium on fabrication characteristics or the strength-to-weight ratio for their product. [Refs. 1,2]

The aerospace industry has been a major driving force for the aluminum industry since the 1930s, when the all-metal stressed wing became the standard for the aircraft industry and established the aluminum alloys as the airframe materials of choice. The extent to which aluminum alloys dominate in airframe applications can be illustrated by looking at two current aircraft. The aluminum alloy content, as a percentage of structural weight, of the Northrop F-20A is 71% and the Boeing 757 is 79%. [Ref. 3]

Aircraft performance requirements have increased continuously, resulting in greater demands on the aerospace

industry. In the past, improvements in engine and airframe design have been the most cost-effective means for meeting increasingly stringent specifications. In the future, significant gains in aircraft performance will be obtained by the use of new materials and new processes that allow reductions in structural weight while increasing airframe strength. Since life cycle costs (LCC) are directly affected by aircraft weight, any reduction in airframe weight can also result in reduced operational costs. It has been estimated that one pound of reduced structural weight in a large commercial aircraft will save 300-400 gallons of fuel over a 20 year life [Ref. 3:p. 319]. There are currently four areas that are being investigated to reduce structural weight: metal matrix composites, polymer matrix composites, new metallic materials and superplastic forming.

The composites, as a class, offer dramatic improvements over the accepted airframe aluminum alloys, and the aluminum industry has responded to the composites challenge by increasing research into newer metallic materials, especially new aluminum alloys, and new processes.

Al-Li alloys offer low density and a high elastic modulus, and were first used in the aerospace industry in 1957, when the Alcoa alloy X2020, an Al-Cu-Li alloy, was used in the RC-5A Vigilante aircraft. X2020 was found to have low fracture properties and was withdrawn from the market in 1974. Al-Li alloys were not used much thereafter until the fracture

toughness was improved. Currently, aluminum-lithium alloys offer great opportunity for the aluminum industry, since these alloys can offer immediate weight savings (10%) in airframes when directly substituted for the current alloys. New tooling and procedures that are required by composites are unnecessary. Further weight savings (up to 15%) can be realized by going beyond direct substitution and designing future airframes specifically for these aluminum-lithium alloys. Several Al-Li alloys are currently in production and are used in a wide range of aircraft, including the F-111, L-1011, S-3A, 737(Mod), 747F, F-20A, and 757-200. [Refs. 3,4,5].

The aluminum-magnesium alloys offer the potential for increased strength, lower density and improved corrosion resistance over other aluminum alloys. However, if the alloy contains greater than 6% magnesium by weight, decreases in ductility and stress corrosion resistance may occur. Research at NPS, which will be discussed in greater detail later, has lead to the development of processing steps that improve the stress corrosion resistance and ductility in high magnesium aluminum alloys. [Refs. 5,6]

Adding magnesium to Al-Li alloys further reduces density while having minimal effect on the elastic modulus. The Al-Mg-Li alloys were first studied in the U.S.S.R. during the 1960s, and led to the development of the first commercial Al-Mg-Li alloy, 01420, which was probably not very widely used [Ref. 7]. More recently, development of Al-Mg-Li alloys for

fusion reactor structural materials has been reported by the Technical Research Laboratory at Sumitomo Light Metal Industries, in Japan. The reports indicate that an Al-5%Mg-1%Li alloy exhibits optimum characteristics (high resistivity, medium strength and good formability) for fusion reactor applications. The addition of trace amounts of zirconium (Zr) as a grain refiner/recrystallization inhibitor results in the Al-Mg-Li-Zr alloys, which may have a calculated density of less than 2.5 g/cm³ and a Young's modulus of 78-84 GPa for some combinations of Mg and Li additions. [Refs. 8,9,10]

B. SUPERPLASTIC FORMING

Superplastic forming (SPF) is a relatively new process for sheet metal forming that lowers the cost and the weight of airframe structures by allowing parts to be fabricated from one sheet of material in one step. SPF was first used on titanium alloys, such as the industry standard alloy Ti-6%Al-4%V, for aerospace applications by Lockheed and Rockwell International. Now, SPF aluminum technology is being introduced into the aerospace industry.

Since the cost of the new aerospace aluminum alloys is generally higher than conventional alloys, reduction in scrap from production is an economically worthwhile goal. Quist et al., estimate that a Boeing 747 requires about 410,000 pounds of aluminum alloy for its production, with only 150-200,000 pounds actually becoming part of the airframe. The balance,

210-260,000 pounds, or 51-63%, is scrap. Boeing and British Aerospace both project that by 1995, aluminum-lithium alloys will make up a minimum of 33% of future airframe weight, even though aluminum-lithium alloys generally cost three times more to produce. Obviously, any method that markedly reduces the amount of scrap involved in production offers large economic benefits to the aerospace industry. [Ref. 3]

By using SPF technology very complicated parts can be fabricated from high strength aluminum alloys without wrinkling, distortion or post formed springback. A single sheet can be formed into a complex of ribs and stiffeners that is lighter and stronger than the assembly it replaces. In cases where more than three steps are required for conventional fabrication, SPF aluminum technology is more economical, even with no parts redesign. Since the SPF process minimizes material waste by nesting parts, it is estimated that savings in materials acquisition costs alone can average 30%. Further savings are realized by the reduction in machining, riveting, sub-assembly time, jigs, drawings and parts inventory. Additional savings are realized by using low cost single dies and low tonnage presses, instead of expensive matched dies and high tonnage presses. Prime candidates for the SPF process are components that have deep compound curves or highly detailed surfaces such as: enclosures, door stiffeners, access panels, ejector seat assemblies and equipment covers.

[Refs. 11,12,13]

One example of the simplification that is offered by the SPF process is the T-39 forward fuselage frame which was originally fabricated from 18 detail parts and 187 fasteners. By using the SPF process, only five detail parts and 20 fasteners are required. Another example is the Airbus 310-300 which now uses diffusion bonded, SPF aluminum access doors that weigh 50% less than the original machined aluminum doors. A third example is large bomber aircraft, which are considered to be the greatest beneficiary of this process. It has been estimated that every pound of airframe eliminated saves \$846 of total life cycle cost. Longer airframe life and increased damage tolerance (by almost one order of magnitude) is ensured, due to a reduced part count (rivets) and the reduction in rivet holes. For the B-1B bomber, structural aluminum parts fabricated by SPF are estimated to save 10-15% in weight and at least 50% in costs. A B-1B has 77,000 pounds of aluminum and titanium in its structure. Full implementation of SPF would result in total manufacturing savings of \$1,732,000 per aircraft, and a life cycle cost savings of \$3,194,000 per aircraft. [Refs. 14,15,16,17]

C. NPS RESEARCH

Under the auspices of the U.S. Naval Air Systems Command (NAVAIR), a considerable amount of research on superplasticity in aluminum alloys has been conducted at the Naval Postgraduate School (NPS). The primary focus of this research has been

on the moderate temperature superplastic response of aluminum alloys that have been thermomechanically processed also at moderate temperatures. Alloys studied at NPS have been the Al-Li alloy 2090, Al-Mg alloys containing 8-10% Mg, and Al-Mg-Li alloys containing 6-8% Mg, 0.5-2.0% Li and 0.1-0.2% Zr.

Salama studied three aluminum alloys, containing 8-10% Mg and 0.09-0.13% Zr, and reported on the effect of varying four processing variables (rolling strain, reheat time between rolling passes, reduction per pass, rolling temperature) on superplasticity in terms of a model for continuous recrystallization during deformation processing [Ref. 18].

Oster and Sanchez studied Al-8%Mg-0.5%Li and Al-8%Mg-1%Li alloys and reported on the microstructural evolution of these alloys, and the effect of the microstructure upon the alloys' superplastic mechanisms. Both reported that these alloys exhibited moderate superplasticity along with a loss in strength, when compared to the binary alloy equivalent [Refs. 19,20].

Ferris and Munro subsequently extended the research of Oster and Sanchez and studied four Al-Mg-Li-Zr alloys, containing 6-8% Mg, 0.5-2% Li, and 0.15-0.25% Zr. They also extended studies on process variables and reported on an excellent superplastic response in one of these alloys, the Al-8%Mg-1%Li alloy, that was in excess of 1,000%. This response was found at a relatively higher initial strain rate ($6.7E-3\text{ s}^{-1}$, $1.7E-2\text{ s}^{-1}$) than is usually reported for

superplasticity in aluminum alloys. Warm rolling and SPD temperature reported for this response was 300°C. It was also concluded that the heating rate to test temperature was significant in developing the fine-grained microstructure associated with superplasticity in these alloys [Refs.21,22].

The purpose of this thesis is to extend Munro's work on the Al-8%Mg-1%Li-0.2%Zr alloy and investigate the effect of another superplastic processing variable, time to reach test temperature (heating rate). It is hoped that this will give further insights to understanding the mechanisms of microstructure evolution and superplasticity in this alloy, and that this knowledge can be applied to improve other aluminum alloys.

II. BACKGROUND

Wrought aluminum alloys that contain as much as 8% Mg and less than 1.5% Li can be classed as non-heat treatable alloys. Their strengths are due primarily to the alloying elements, and also may be improved by deformation.

When an alloy element is present in excess of the solid solubility limit, a second phase may form. This second phase may be an intermetallic compound or a pure alloying element.

The solubilities of solutes in ternary alloys are often less than the solubilities found in the corresponding binary systems. Solute atoms, in excess of the solid solubility limits, may form metastable phases under non-equilibrium conditions.

A. ALLOY ELEMENTS

1. Magnesium

Magnesium readily goes into a substitutional solid solution with aluminum, since the atomic radii of the two elements are similar (the atomic radius of magnesium is 12% greater than that of aluminum). The solid solubility is not complete and the aluminum-magnesium binary phase diagram in Figure 2.1 [Ref. 23:pp. 105-108] shows that an Al-8%Mg alloy, at equilibrium, will have 6.7 wt. % Mg in solid solution at a temperature of 300°C. The remaining Mg will be present in the

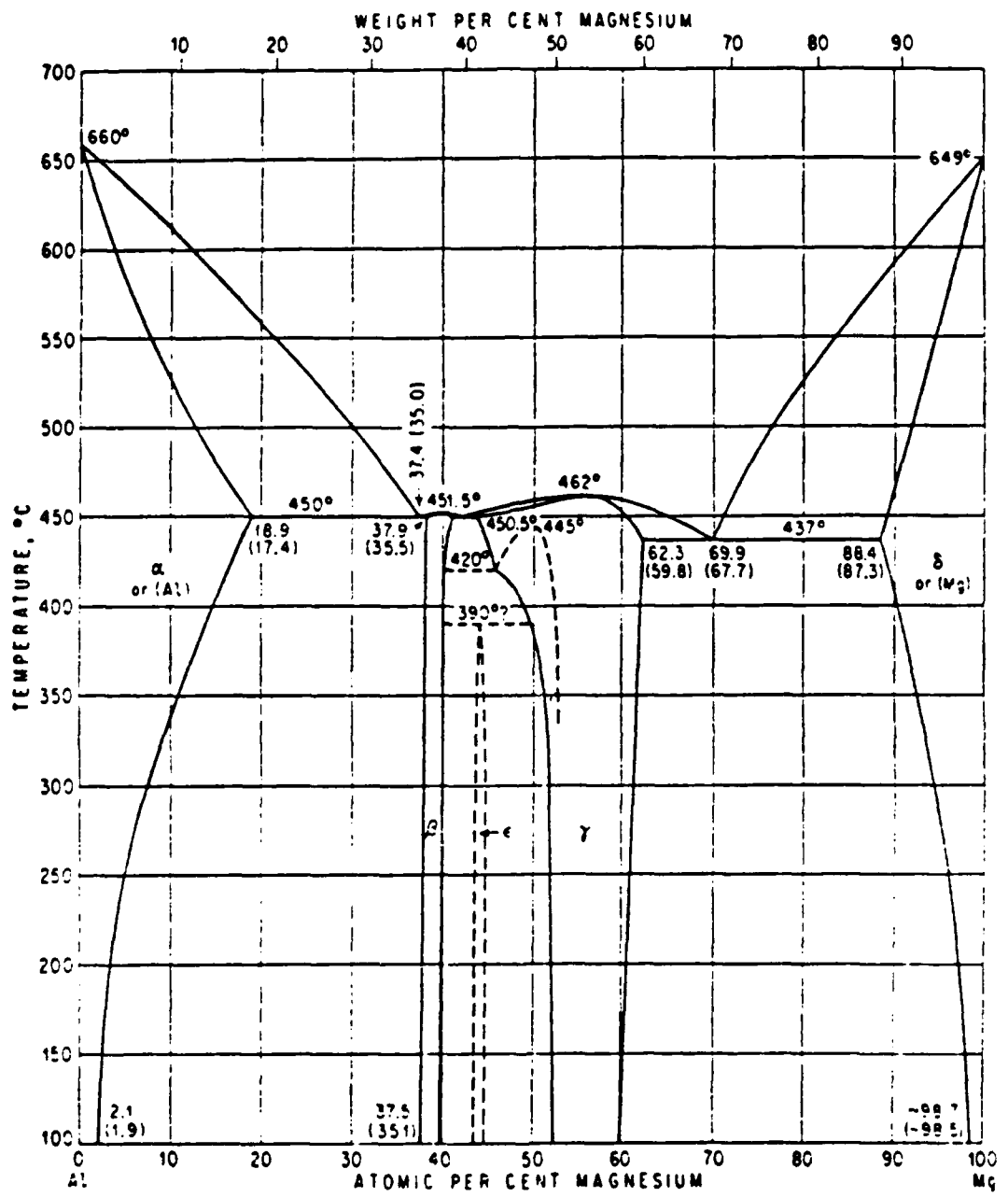


Figure 2.1 Aluminum-Magnesium Binary Phase Diagram

form of a brittle, intermetallic β phase (Al_8Mg_5). The β phase is found when the Mg content is greater than 2 wt. %, and is a complex f.c.c. structure with 1,173 atoms per cell ($a = 2.81$ nm) [Refs. 23,24].

For a homogenized, high-Mg alloy, annealing at 300°C without rolling causes the β phase to form at grain boundaries, with preference for the triple points [Refs. 25,26]. As a result of this grain boundary segregation of β , Al-Mg alloys containing greater than 5% Mg are prone to stress corrosion cracking, and are rarely used in the cold worked state [Ref. 24:p. 811]. By using processing steps developed at NPS, the β phase is found to precipitate uniformly throughout the microstructure, which minimizes stress corrosion susceptibility [Ref. 25:p. 48].

Any second phase such as the β phase may stabilize grains and sub-grains, depending upon its distribution, morphology and strength. Dislocation movement and boundary changes can be retarded by the presence of the β phase. Thus, the relatively large percentage of β that can precipitate in a high Mg alloy may have a significant effect in superplastic deformation (SPD).

2. Lithium

Lithium is one of only two elements, beryllium (Be) being the other, that simultaneously decreases the density of an aluminum alloy, while increasing the alloy's elastic modulus. The aluminum-lithium binary phase diagram in Figure

2.2 [Ref. 23:p. 104] shows that lithium at 300°C has a solid solubility of 1.2 wt. % in aluminum. Strengthening due to addition of lithium to aluminum maybe achieved by precipitation of a fine, evenly distributed metastable second phase, δ' (Al₃Li). The δ' phase has a cubic structure ($a = 0.401\text{ nm}$) and forms a coherent precipitate exhibiting a superlattice structure, due to the small misfit between the δ' and aluminum structures. The precipitation sequence for the δ' phase from a supersaturated solid solution (SSS) is:



If overaging is allowed, the incoherent δ phase is produced preferentially at the grain boundaries, leaving a weaker precipitate free zone (PFZ), which in turn reduces alloy strength. At concentrations of 0-1.6 wt. % lithium the δ' phase is not seen [Ref. 27]. However, at concentrations above 1.7 wt. %, the δ' phase cannot be prevented from forming, even with a rapid quench [Refs. 28,29]. Therefore, a low lithium content of 1.0 wt. % is expected to be as a solute.

3. Zirconium

Zirconium is used in small concentrations to stabilize the grain structure during casting and hot working. The solid solubility of zirconium in aluminum can be seen in Figure 2.3 [Ref. 23:p. 153] to be 0.11 wt.% at the peritectic temperature (660.5°C).

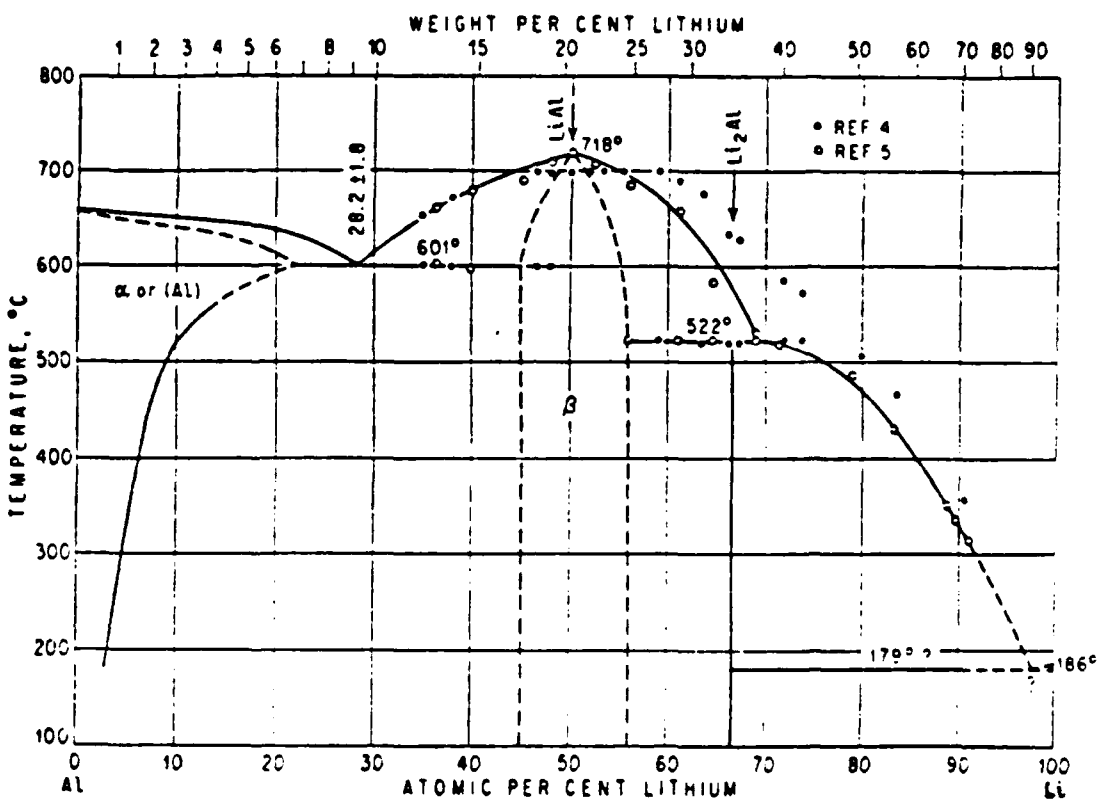


Figure 2.2 Aluminum-Lithium Binary Phase Diagram

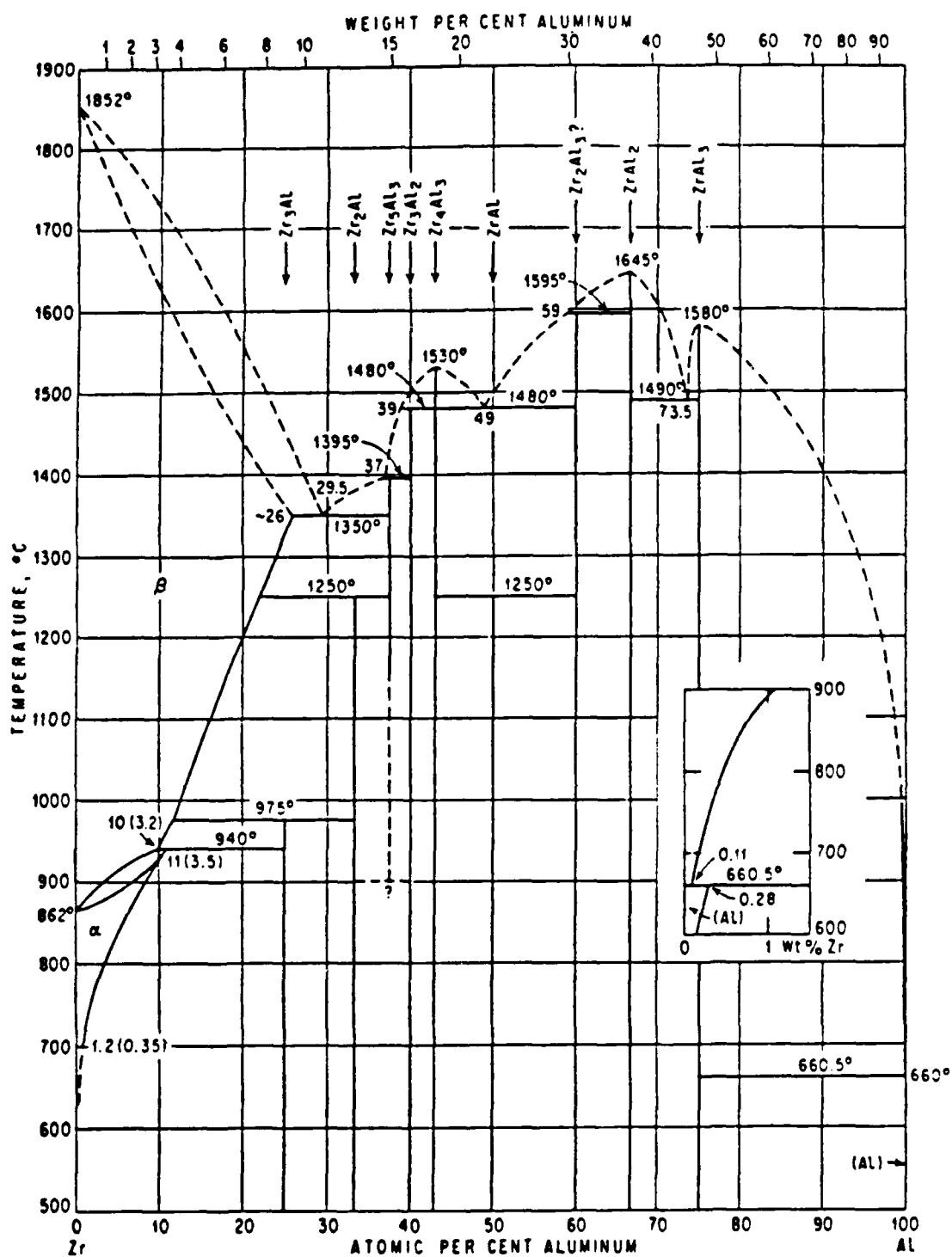


Figure 2.3 Aluminum-Zirconium Binary Phase Diagram

Zirconium forms a very fine metastable phase, secondary Al₂Zr, which is slow to coarsen at SPF temperatures, and therefore contributes to maintaining microstructural stability during SPF. [Ref. 30] The secondary Al₂Zr particles are a smaller, coherent cubic ($a = 0.405 \text{ nm}$). These secondary particles may possibly act as δ' co-precipitation sites, in addition to providing nucleation sites for aluminum matrix solidification [Refs. 24;31:p. 414]. The secondary Al₂Zr usually forms a coherent, spheroidal precipitate. But, non homogeneous secondary precipitations are common, due to low the diffusivity of zirconium in aluminum.

The disadvantage of using zirconium for grain refining is that high casting temperatures and rapid solidification are required in order to prevent the formation of coarse primary Al₂Zr. Primary Al₂Zr particles are large, non-coherent, tetragonal ($a = 0.4015 \text{ nm}$, $c = 1.732 \text{ nm}$), and average five microns in diameter. This coarse primary phase tends to produce undesirable cavitation during SPF, thus making it essential to maintain precise control of the casting variables [Ref. 30]. From the inset in Figure 2.3, it can be seen that a practical limit to adding Zr as an alloy is 0.4-0.5%, to keep casting temperatures above the liquidus limit while staying within manageable limits for casting temperature control (<850°C).

4. Al-8%Mg-1%Li-0.2%Zr Alloy

By using a high magnesium (8 wt. %) alloy, a high volume fraction of β exists that acts to stabilize boundary motion and grain coarsening during SPF. This stabilization is achieved primarily by pinning of continuously recrystallized grain boundaries [Ref. 32].

Ferris [Ref. 21:p. 21] reports that this alloy has a calculated density of 2.52 g/cm^3 , which is 2% less than the Al-Cu-Li alloy 2090 (2.57 g/cm^3) and 11% less than the superplastic Al-Zn-Mg-Cu alloy, 7475 (2.83 g/cm^3) [Refs. 13, 33].

For the Al-8%Mg-1%Li-0.2%Zr alloy, precipitation apparently follows the binary Al-Mg phase diagram (Figure 2.1) with Li acting as a third element [Ref. 22]. Instead of the magnesium forcing lithium out as δ' , Munro [Ref. 22] reports that lithium essentially acts to displace magnesium on an atom for atom basis, producing more β than the binary Al-Mg phase diagram predicts. No δ' precipitate was observed in this alloy, nor were any multi-constituent intermetallic compounds, such as Al_2MgLi . The conclusion from this is that the Al-8%Mg-1%Li-0.2%Zr alloy is a quasi-binary, which is in agreement with Mondolfo [Refs. 21:p. 75;22:p. 74;24:p. 806]

From Figure 2.1, the β solvus temperature (T_{solvus}) is 325°C for an Al-8%Mg alloy. However, using differential scanning calorimeter (DSC) testing indicates that the actual β solvus is 360°C (T_{DSC}) for the Al-8%Mg-1%Li-0.2%Zr alloy [Ref.

22:p. 33]. From this, the equivalent β volume fraction and magnesium content were calculated to be 15.5% and 12.7%, respectively. Lithium appears to do more than just displace magnesium atoms from solid solution, since the β particles were resistant to coarsening with the presence of Li during elevated temperature testing [Ref. 22:p. 75].

Secondary Al₃Zr is an effective inhibitor of recrystallization in Al-Li alloys and facilitates composite precipitation, where δ' particles nucleate on secondary Al₃Zr particles and in the Al-Li-Zr matrix [Ref. 34]. The possibility also exists that lithium in the alloy is incorporated into the sub-lattice of the Al₃Zr particles [Ref. 35].

Dinsdale, et al., [Ref. 36] reported on the effect of varying the content of zirconium in an Al-2%Mg-2%Li-x%Zr alloy. Cast ingots were homogenized and direct extruded, followed by solution treatment and water quenching, with aging to peak hardening as the final step. They concluded that increasing the concentration up to 0.2 wt. % Zr markedly reduced grain size, while producing a sub-grain structure. No sub-grains were observed from 0-0.05% Zr. Sub-grains were observed from 0.1-0.2% Zr, with sub-grain size decreasing as zirconium content increased. At 0.1% Zr, sub-grain size averaged 4-5 microns, and at 0.2% Zr, sub-grain size averaged 1-2 microns. Finally, they report that the addition of Zr seems to not only cause grain refinement; but, that zirconium additions inhibit recrystallization, thus producing large

numbers of low-angle boundaries. Noble, et al., [Ref. 37] report that of the grain refining additions studied (Zr, Mn, Fe+Ni) zirconium was the most effective in improving the room temperature strength, due to the formation of a sub-grain structure.

B. SUPERPLASTICITY

In the broadest sense, superplasticity refers to large elongations in the absence of localized necking. Deformation occurs at an elevated temperature, usually at 0.5 T_{melting} or greater. Superplasticity is usually defined as any elongation in excess of 200%. A recent record for elongation was cited by Sherby and Wadsworth [Ref. 38] as 7,550% in an aluminum-bronze alloy. However, the usual elongations reported are 300-1000%.

1. Phenomenological Description

The large elongations characteristic of superplasticity result from the suppression of necking. This suppression of necking is closely related to the strain rate sensitivity exponent (m), which can be found from the slope of a log flow stress vs. log strain rate plot. The general relation between flow stress and strain rate at a constant strain and temperature is

$$\sigma = C \dot{\epsilon}^m \quad (2.1)$$

where

$$m = (\delta \ln \sigma) / (\delta \ln \epsilon). \quad (2.2)$$

Since

$$\sigma = P/A \quad (2.3)$$

and, by definition

$$\dot{\epsilon} = -(1/A)(dA/dt) \quad (2.4)$$

then

$$\dot{\epsilon} = - (P/C)^{1/m} [1/A^{(1-m)/m}] \quad (2.5)$$

and combining

$$-(dA/dt) = (P/C)^{1/m} (A^{-(1-m)/m}) \quad (2.6)$$

where (A) is cross sectional area, (P) is the applied load, (C) is a material constant, and (m) is the strain rate sensitivity exponent. From Equation 2.6 one can see that dA/dt is strongly dependent upon (m) . When $m = 1$, dA/dt is independent of (A) , and any necking previously initiated stops progressing. When $m < 1$, the smaller the area A is, the more rapidly the area decreases and thus incipient necks may form and necking occurs. The closer (m) is to unity, the slower the necking process. Typically, superplastic materials have m -values of about 0.5, and this has become a criterion for superplasticity. [Ref. 39]

Early explanations of the superplastic phenomenon generally fall into one of two categories: diffusion dominated mechanisms or dislocation creep mechanisms. Currently, both mechanisms are credited with a role in superplasticity, since SPF is closely associated with temperature dependence. This temperature dependence has been related to the activation energy required for either grain boundary diffusion or lattice diffusion by Sherby and Wadsworth [Ref. 39:pp. 452-453]. Superplastic flow rate for grain boundary diffusion control has been proposed to be governed by

$$\dot{\epsilon} = K_1 (\sigma/E)^2 [(bD_{gb})/d^3] \quad (2.7)$$

and the superplastic flow rate for lattice self diffusion control is given by

$$\dot{\epsilon} = K_2 (\sigma/E)^2 [(D_v)/d^2] \quad (2.8)$$

where (b) is the Burgers vector of the dislocation, (D_{gb}) is the grain boundary diffusion coefficient, (D_v) is the lattice diffusion coefficient, (d) is the grain size mean linear intercept and (E) is the modulus of elasticity.

The importance of grain size (d) is emphasized here, since any grain growth has dramatic effect on strain rates. From Equations 2.2, 2.7 and 2.8, it can be seen that a small grain size (d) will result in a high strain rate and a greater likelihood of control of superplastic flow by superplastic mechanisms. [Refs. 39:p. 453;40]

Sherby and Ruano [Ref. 40] concluded that grain boundary sliding (GBS) accommodated by slip was the most likely mechanism being described by Equations 2.7 and 2.8. The superplastic flow in a fine grained material is proposed to be due to two separate processes, GBS and slip, occurring in two separate regions of the grain: the mantle, located in the outer periphery of the grain, and the core of the grain. Slip occurs in the core, while GBS accommodated by slip occurs in the mantle region. At high strain rates and low temperatures, the core process (slip) dominates, while at high temperatures and low strain rates, the mantle processes (GBS and slip) dominate [Refs. 40:p. 243;41:p. 7]. Thus, plastic flow is characterized by two processes in superplastic materials. If the mantle processes (GBS and slip) dominate, then GBS and grain rotation can occur. Grain rotation, along with GBS, is a central feature of superplasticity. This means that the mantle processes are associated with superplasticity, while the core process is associated with normal ductility.

[Refs. 18:p. 42;41:p. 7]

2. Structural Prerequisites for Superplasticity

The structural requirements for a material to be superplastic are, as noted before, a fine grain size (typically less than ten microns) and a second phase to inhibit grain growth at elevated temperatures. This second phase should be similar in hardness to the matrix phase to minimize cavitation at the particle-matrix interface, which decreases

low temperature ductility and impact resistance. If the second phase is dissimilar from the matrix phase, then it should be in the form of fine, hard particles evenly distributed throughout the matrix phase, to minimize cavitation during SPF.

Grain boundaries between grains should be high-angle (disordered) boundaries to facilitate grain boundary sliding, the primary deformation mode during superplastic flow. High-angle boundaries are usually characterized by misorientations of 10-15° or greater. Lower angle boundaries, which are commonly found after warm working, are not thought to slide as readily, if at all. To date, there is no consensus as to what the misorientation must be for superplastic flow.

Grain boundaries should be mobile, so that stress concentrations can be reduced. These stress concentrations build up during GBS, accumulating at obstructions and at triple points. After SPF, presence of equiaxed grains is evidence of grain boundary migration. Equiaxed grains allow many grain boundaries to experience shear and, hence, to slide. Elongated grain structures will show much less GBS when stressed parallel to the longitudinal direction of the grain, even though the grains are fine in size in the transverse direction. Testing in the transverse direction of such grain structures can lead to extensive GBS and superplasticity. [Refs. 39,40]

3. Microstructural Evolution

As a metal is deformed during warm working, dislocations are generated. These dislocations interact with other mobile dislocations and with dislocations initially present. The dislocations rearrange upon subsequent heating (anneal) by diffusion controlled processes. In a heavily deformed material, recovery may compete with recrystallization to remove dislocations. [Ref. 42]

a. Recovery

Recovery occurs when the defect concentration is reduced without movement of those grain boundaries present prior to deformation. Dislocations annihilate early in the heating (annealing) process, as dislocations of opposite sign attract each other. Dislocations of like sign are, meanwhile, repelling each other. [Ref. 42]

Polygonization occurs when edge dislocations of like sign line up one atop the other by processes of glide and climb, decreasing the elastic energy of the dislocations. The final grain structure consists of sub-grains separated by low-angle boundaries. [Ref. 42]

Dynamic recovery is the recovery process that occurs as the metal is actually being deformed. Cross slip and climb are the dominant mechanisms occurring most readily when temperatures are raised or in high stacking fault energy (SFE) metals like aluminum. Under conditions of rapid deformation during hot-working, dislocation climb is rapid,

and sub-grains continuously grow. Sub-grain boundaries are constantly being created, while others are eliminated. As a result, under hot working conditions, low angle boundaries dominate. Static recovery occurs solely as the result of the mutual interaction of the dislocations, while in the dynamic recovery process, the energy of the deformation process is added. [Ref. 39:p. 535]

The addition of magnesium to aluminum decreases the SFE to some degree, and therefore decreases the ease of the recovery process. However, the addition of a high magnesium content to solid solution does not prevent recovery from being the dominant process, in the competition between recovery and recrystallization. [Ref. 21:p. 15]

In summary, recovery is the process that covers the rearrangement of a high density of dislocations, by climb and glide, resulting in subgrains separated by low-angle boundaries. The dislocations remaining after recovery have decreased the lattice elastic energy by "clustering" in walls. The deformed crystal maintains its identity while changing dislocation density and distribution. [Ref. 43]

b. Recrystallization

In heavily deformed materials, recovery is generally interrupted by recrystallization, which is the process where new, relatively perfect grains are formed. These new crystals are nucleated at sites in the lattice that have a high stored strain energy. Recrystallization can be

either discontinuous or continuous, with discontinuous (nucleation and growth) recrystallization being the classical recrystallization path.

In discontinuous recrystallization (DRX), migrating high-angle boundaries sweep through the deformed structure, altering the crystal orientation of the deformed region through which the boundaries pass. New crystals are formed by nucleation around large inclusions or at prior grain boundaries. Both of these types of sites are regions of non-homogeneous deformation. The term "discontinuous" is used since this passage of a high-angle boundary causes a sudden change in defect density and lattice orientation. Control of grain size by the use large particles (> 1 micron) has been successfully used in the 7475 Al alloy, with grain sizes on the order of 10 microns. If such a recrystallized grain size is desired via DRX, then the average spacing of nucleating particles should be slightly less than ten microns to compensate for potential nucleation sites that are not activated. This spacing and particle size is found in the 7xxx alloys. [Refs. 44,45]

An alternative mode for recrystallization is the less understood continuous recrystallization (CRX) process, also known as *in situ* recrystallization. CRX proceeds by gradual sub-grain growth (coarsening) that leads to the formation of high-angle boundaries without a high-angle boundary passage through the crystal. The CRX process starts

with deformation producing elongated dislocation cells of small misorientation. With annealing, these cells gradually increase in size and several low-angle boundaries combine to form a high-angle boundary. This increasing misorientation between sub grains proceeds throughout the microstructure with no high-angle boundary motion. Nucleation of individual recrystallized grains does not occur in CRX. As a result, CRX is expected in alloys with high density of small particles. CRX enables a more highly refined microstructure to develop than does DRX. Grain size in Al-Li alloys, using CRX, are typically 2-4 microns. Finally, recrystallization via DRX results in change in texture due to the migration of the high-angle boundary. With CRX, texture is maintained by not having a boundary front migration. [Refs. 38,44,45]

C. GRAIN REFINEMENT BY THERMOMECHANICAL PROCESSING

CRX and DRX represent two different paths towards the common goal of the fine grain size desired for superplasticity. Three thermomechanical processing (TMP) schemes are currently used to achieve CRX or DRX.

1. TMP for DRX

TMPs that utilize DRX for grain size control are applicable to alloys with a high density of large particles ($d > 1$ micron). Alloys of this type have a Zener pressure (P_z) near 10 kPa [Ref. 44:p. 77]. The large particles provide nucleation sites for discontinuously recrystallizing grains.

DRX is rapid and does not require concurrent deformation at the recrystallizing temperature. The recrystallized grain size is not very sensitive to minor variations in alloy composition or in TMP parameters. [Refs. 44,45]

Grain size is, however, very sensitive to heating rate to recrystallization temperature in the DRX process. In the 7xxx series aluminum alloys, heating rates greater than 5 °C/sec are required in the final recrystallization stage [Ref. 46:p. 193]. At slower heating rates, the resulting recrystallized grain size is coarse, due to activation of fewer, more highly favored nucleation sites at lower temperatures (300-360°C) when compared to the grain size attained with higher heating rates. These fewer nuclei then have time to grow and preclude nucleation at many sites at higher temperatures. [Refs. 44:p. 57;46:p. 198]

The DRX process commonly used is the so-called "Rockwell" process for 7075 Al, and is schematically shown in Figure 2.4 [Ref 45:p. 76]. The key to this process is the introduction of micron-sized particles in a refined dispersion to create nucleation sites for recrystallization. Each of the four steps has a role in producing the fine grain size (but not as fine as with CRX).

Solution treatment homogenizes the alloy, putting all Zn, Mg and Cu into solid solution. The Al-Cr particles ($d = 1$ micron) are not dissolved, and are uniformly dispersed.

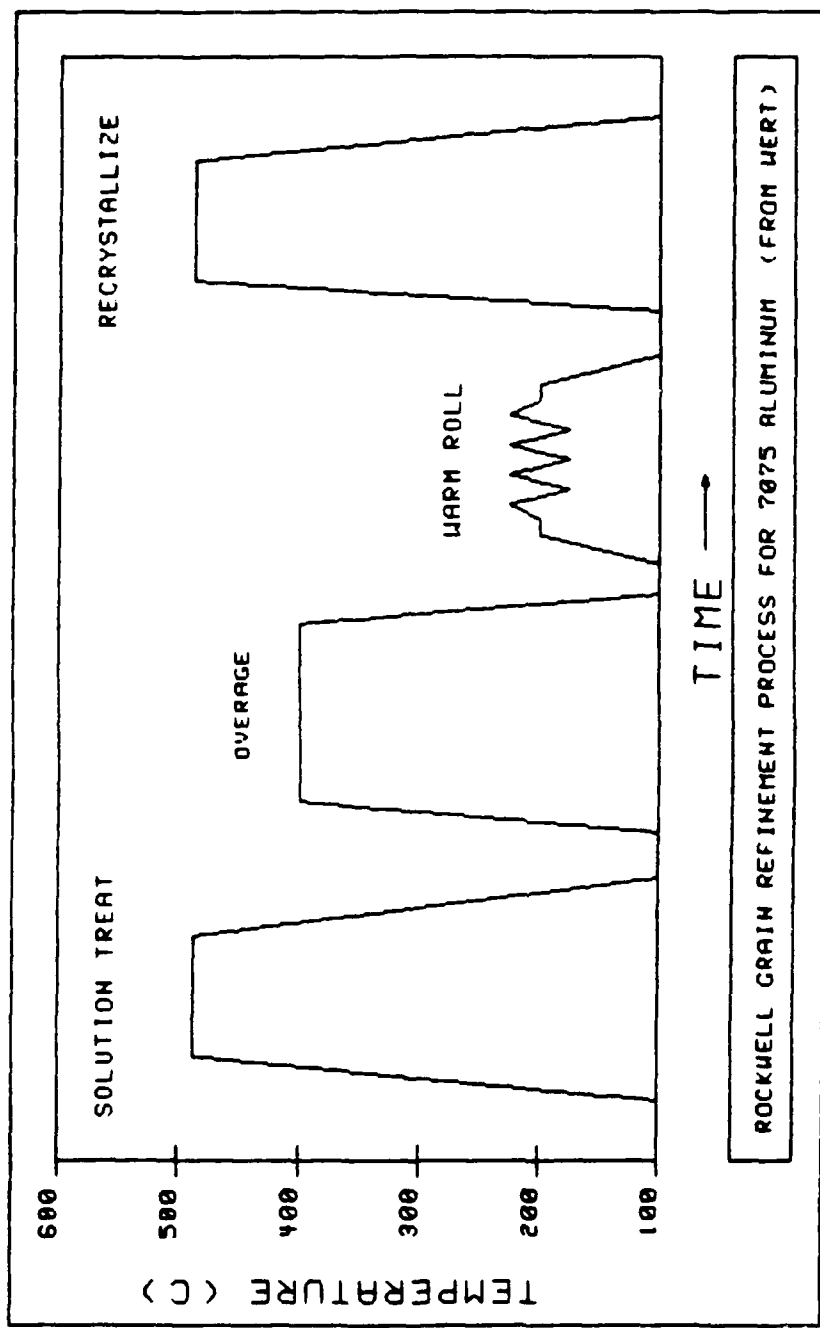


Figure 2.4 TMP Using DRX for Grain Refinement (from Wert)

Overaging at $T = 400^\circ\text{C}$ results in precipitate particles capable of acting as nucleation sites for recrystallization. The particles must be about 0.75 microns or larger if they are to be effective as nucleation sites. Warm rolling introduces defects (dislocations) into the alloy, with a high defect density around the dispersed hard particles.

Recrystallization starts when nucleation occurs in regions of high defect density around the particles. The recrystallized grains consume the defect zone and then grow into the matrix, while the precipitates also dissolve.

Peak SPD ductility with the 7075 Al alloy is that attained using an initial strain rate of $2\text{E-}4 \text{ s}^{-1}$ and at a test temperature of 516°C ($0.95 T_{\text{melting}}$) [Ref. 22:p. 19]. A well-known problem with this alloy and process is the fact cavitation, resulting from tensile separation of grain boundaries, occurs during SPD. Back pressure applied during the SPF process has been used successfully to minimize the cavitation.

2. TMP for CRX (SUPRAL)

One TMP has been developed for the Al-Cu-Zr alloys (SUPRAL) by Superform Metals Ltd. that utilizes CRX for grain size control. For this process, Wert [Ref. 44:p. 76] reports that a very high density of very fine particles is required to provide a Zener pressure of 40 kPa or greater, which is supplied by high densities of Al₂Zr dispersoids, and that CRX requires either a prolonged anneal or concurrent deformation

at elevated temperatures. Particles should be less than one micron in diameter. CRX in this alloy is sensitive to variations in process parameters and alloy composition. Despite the care required in this process, much finer grain size can be obtained with CRX than with DRX.

Nes [Ref. 47] reports that the SUPRAL alloys are recrystallized during the initial stages of the SPF process, by a strain-induced continuous reaction. No recrystallization heat treatments are used prior to deformation.

Since this is a proprietary process, the exact details are unknown. However, the basic steps in this process can be summarized below. The alloy is cast at a very high temperature to ensure the presence of the ultra fine dispersion of Al₃Zr. It is then warm worked at a low temperature (100-200 °C), just sufficiently high to avoid cracking, and with cross rolling for texture control. The alloy is then slowly heated to 500°C where polygonization and static recovery occur. At the same time, the onset of CRX occurs, with a further enhancement of CRX occurring upon the initiation of SPD. [Ref. 47]

3. TMP for CRX (NPS Procedure)

The TMP for CRX used with this alloy was devised by Munro, and is shown in Figure 2.5 [Ref. 22:p. 29]. A key difference between the SUPRAL process and the one used at NPS is that CRX occurs during the reheating between warm rolling passes [Ref. 48].

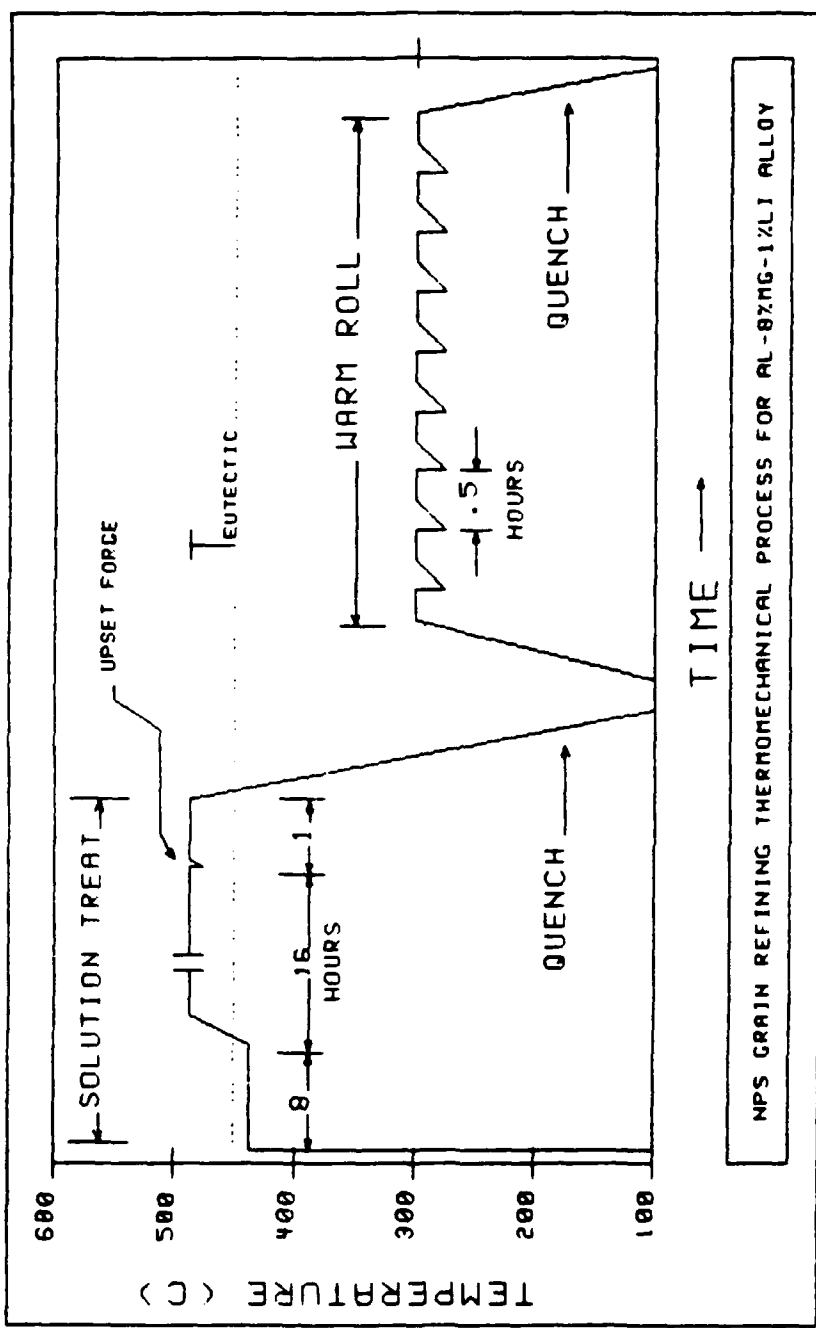


Figure 2.5 TMP for Grain Refinement Using CRX (from Munro)

Solution treatment is performed at two temperatures. For eight hours, the solution treatment is at 440°C, 10°C below the eutectic temperature to minimize hot cracking by driving any eutectic present back into solid solution. The remainder of the solution treatment is at 480°C, for 16 hours. Upset forging at 480°C further homogenizes the alloy, and prepares it for the subsequent warm rolling.

The warm rolling is performed at 300°C, with approximately isothermal conditions being maintained by reheating between passes, alternating sample ends entering the rolling mill with each pass and by minimizing time out of the furnace. Warm rolling reduces the tendency of β particles to precipitate at grain boundaries and triple points by providing nucleation sites for the β phase to disperse more homogeneously. Since the rolling takes place at temperatures below the solvus temperature, the β precipitates as dislocation structures form. [Refs. 5,26]

During the warm rolling and reheating cycles, dynamic and static recovery take place. Recrystallization (CRX) occurs progressively during the heating between each of the warm rolling passes, resulting in refinement of the grain structure with each new rolling pass [Ref. 48]. When the final rolling pass has been completed and the material is cold-water quenched, an extremely fine grain size (1-3 microns) and a very fine β phase (0.5-1.0 microns) is the

result in the Al-8%Mg-1%Li-0.2%Zr alloy, with a high level of stored energy also present [Ref 22:p. 54].

Two features that differentiate this TMP from the TMP used for DRX are the absence of overaging and recrystallization steps, and a lower temperature (300°C , $0.7 T_{\text{melting}}$) for superplastic flow.

D. COMPETITION BETWEEN CRX AND DRX

In order for CRX to occur, suppression of the more rapid DRX process is essential, with boundary drag pressures sufficient to retard the rapid high-angle boundary front migration that is characteristic of DRX. A dense dispersion of fine particles (Al_3Zr) provide the necessary boundary drag ($P_z > 40 \text{ kPa}$). Drag sufficient to stop or slow DRX would logically also have some negative effect on CRX, if not for boundary tension. [Ref. 44:pp. 71-77]

Drag pressure is a direct function of boundary interfacial energy, with drag pressure high on high-angle boundaries, slowing or stopping their migration and effectively inhibiting DRX, while the drag pressures on the low-angle boundaries are low, allowing CRX to proceed. In addition, there is evidence that sub-grain boundary migration occurs as particles coarsen. While a high drag force slows DRX, the alternate straining and annealing may provide additional energy for the CRX process.

[Ref. 44]

CRX is difficult to observe, probably due to the very delicate balance required for CRX to proceed. Suppression of DRX must occur, while low-angle boundary migration continues. Factors that can have an effect include: degree of supersaturation, dislocation density and distribution, homogeneity of alloy, temperature and possibly heating rate.

1. Influence of Concentration

Salama [Ref. 18:pp. 49-52] and Cahn [Ref. 43:pp. 1633, 1662] have both addressed the influence of concentration and temperature upon the recrystallization. In Al-Mg alloys, the precipitate (β) phase is liable to form, coarsen or dissolve during the anneal which will, in turn, have an effect upon grain boundary migration. At a high concentration of solute, or a low temperature, precipitation will occur during recrystallization. The precipitation will then impede boundary migration. The extent and type of recrystallization in turn depends upon the competition between these two reactions, and this implies sensitivity to temperature for a given solute concentration. [Ref. 43:pp. 1650-1653]

Figure 2.6 is an adaptation from Salama [Ref. 18:p. 52] that illustrates the effects temperature and solute concentration may have upon the competition between DRX and CRX in the Al-Mg system. The following reactions occur as the α phase of an Al-Mg alloy is cooled from the solidus temperature: Zone I, normal (DRX) recrystallization only; Zone II, recrystallization (DRX) followed by precipitation; Zone III,

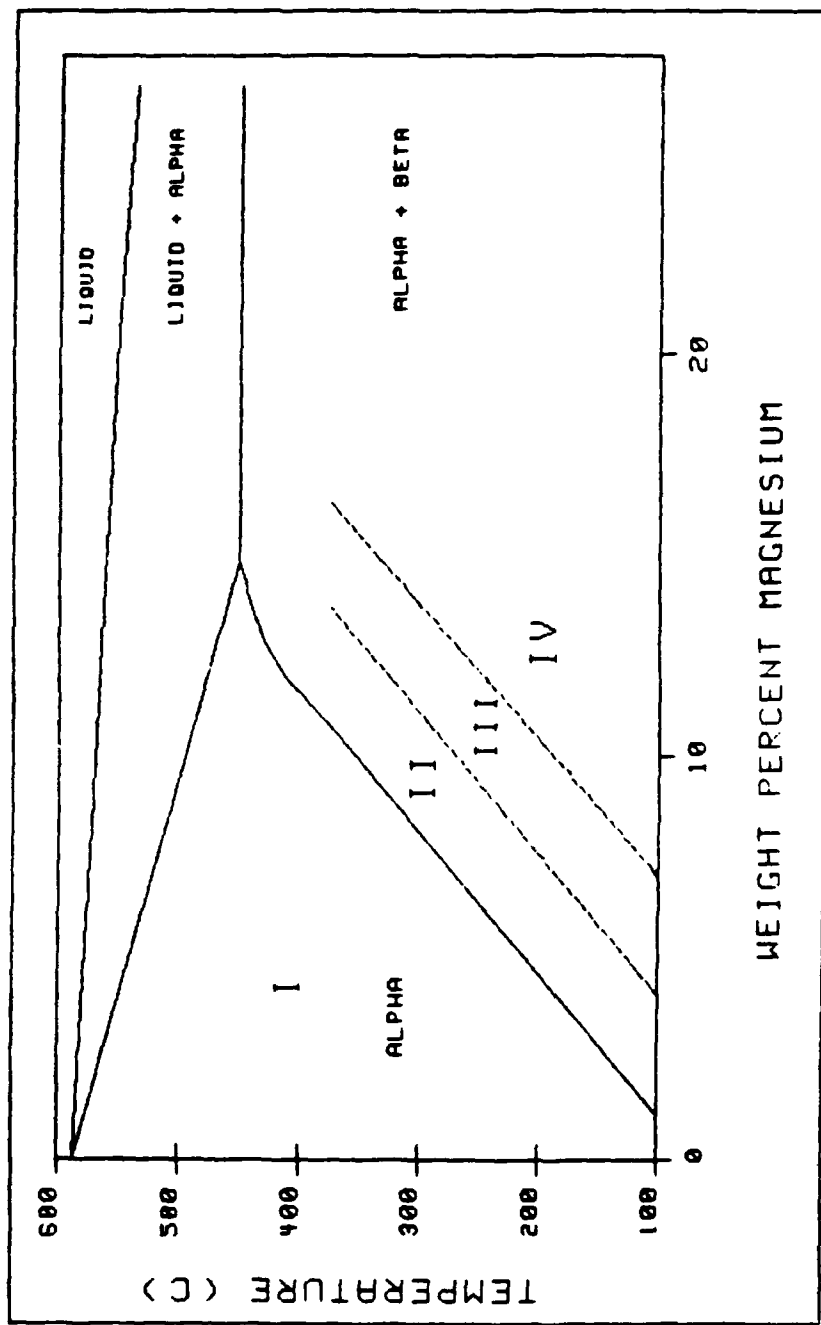


Figure 2.6 Influence of Concentration and Temperature Upon Recrystallization Kinetics in a Deformed, Supersaturated Solid Solution Al-Mg System.
 Zone I: DRX Only. Zone II: DRX Sequentially Followed by Precipitation. Zone III: Simultaneous DRX and Precipitation. Zone IV: CRX Dominates (adapted from Salama, p. 52)

simultaneous DRX and precipitation; Zone IV, CRX dominates. Zones II and III are probably very small and are located near the solvus line. This assumption is corroborated by Cahn [Ref. 43:p. 1662] who refers to the dramatic effect decreasing temperature by 1-2°C (representing only a 0.1% volume fraction change) has upon secondary recrystallization in an Al-Cu alloy. Results reported by Munro for this alloy at 350°C suggest that the boundary between Zones III and IV lies somewhere below 350°C [Ref. 22:p. 71].

2. Combined Reactions

Hornbogen [Ref. 49] elaborates further, by addressing the influence defect density (p) and time (t), in addition to concentration (x) and temperature (T), have upon combined reactions. Combined reactions are defined as reactions that occur in all solids where the thermal equilibrium is approached by more than one elementary reaction. Examination of the free energy diagram of any binary alloy system will show that there are stable and metastable phases. For metastable phases, various reaction mechanisms exist that are partially controlled by the free energy diagram, as well as by diffusion kinetics (nucleation, growth). The mechanics of these reactions can be either abrupt (discontinuous) or gradual (continuous). For the discontinuous reaction, a front exists for nucleation and diffusion to occur at a rapid rate. As this front moves through the structure, lattice defects are

absorbed. The requirements for this reaction are met by high-angle grain and phase boundaries.

A continuous reaction occurs in the absence of a discontinuous reaction; that is, if the reaction front does not exist, can not form, or is held back by sufficient drag forces. A continuous reaction is favored by a high density of nucleation sites, or by pre-existing centers of growth (subgrains). A continuous process is growth with a continuous variation of composition and defect density across the material.

The velocity (v) of a reaction front is described by the relationship:

$$v = m \Sigma f \quad (2.9)$$

where (m) is the mobility factor and (Σf) is the sum of the forces acting at the reaction front. The sum of the forces (Σf) is described by the relationship:

$$\Sigma f = (f_D + f_R - f_s - f_p) \quad (2.10)$$

where (f_D, f_R) are driving forces due to Decomposition or Recrystallization and (f_s, f_p) are retarding forces caused by particles or by segregation. A discontinuous reaction can occur if a reaction front exists and if the driving forces dominate over the retarding forces; that is, $\Sigma f > 0$. Conversely, if the retarding forces dominate over the driving

forces, then $\Sigma f < 0$ and a continuous reaction is possible, even though a reaction front exists.

The driving force (f_D) due to decomposition (precipitation) is defined as the energy gained by change in chemical composition and is expressed as:

$$f_D = (RTx_1) \ln(x_0/x_1) (V_m)^{-1} \quad (2.11)$$

where (RT) is thermal energy, (V_m) is molar volume, and (x_0/x_1) is the ratio of solid solution concentrations before and after the reaction. Inspection of this equation reveals (f_D) is primarily influenced by solute concentration (x) and temperature (T).

The driving force (f_R) is the energy gained due to healing out of lattice defects (recrystallization) and is defined as:

$$f_R = \alpha G b^2 (p_0 - p_1) \quad (2.12)$$

where (.5 < $\alpha < 2$) and ($p_0 - p_1$) is the difference in dislocation density before and after the reaction. Inspection of this equation reveals that (f_R) is primarily influenced by dislocation density.

The retarding force (f_s) is due to the segregation of solid solution atoms into the reaction front and is defined as:

$$-f_s = U_s x_{eff} \quad (2.13)$$

where (U_s) is the specific energy for segregation into the reaction front and (x_{eff}) is the effective segregation into the reaction front.

The retarding force (f_p), also known as the Zener force (P_z), is caused by particles which block out parts of the reaction front and is defined as:

$$-f_p = K_1(E_{gb} V_p) (d)^{-1} \quad (2.14)$$

where (K_1) is a constant, (E_{gb}) is the grain boundary energy, (V_p) is the volume fraction of the second phase and (d) is the diameter of the particle. Inspection of this equation reveals that $(-f_p)$ is primarily influenced by the volume fraction of particles and the inverse of particle size.

The sum of these forces (Σf) has to be considered as a function of the time (t) of isothermal annealing at temperature (T), and is expressed as:

$$\Sigma f(T, t) = [f_D(T, t) + f_R(T, t) - f_s(T, t) - f_p(T, t)]. \quad (2.15)$$

Examination of this equation, along with Equations 2.11 and 2.14, reveals that the driving force for precipitation (f_D) and the retarding force due to particles ($-f_p$) are interrelated. With time (t) increasing and temperature (T) constant, concentration (x) changes due to the formation of particles which produce $(-f_p)$. If the retarding force due to segregation $(-f_s)$ is ignored, then the three forces $(+f_D, +f_R, -f_p)$ can interact to produce the sequence found in Figure 2.7.

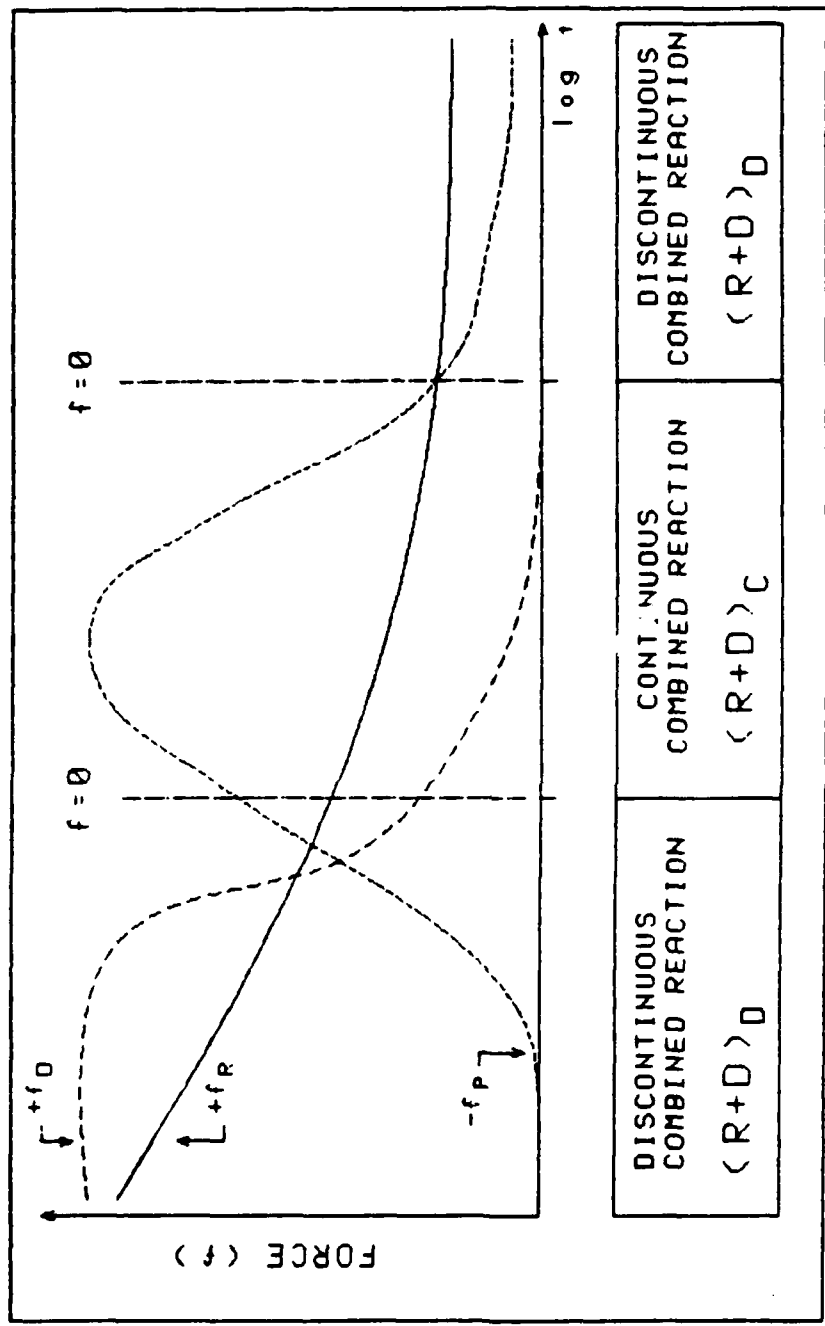


Figure 2.7 Interaction of Driving Forces and Retarding Forces During Isothermal Aging, Resulting in Sequence of Simultaneous Combined Reactions
(from Hornbogen, p. 963)

Finally, dislocation density (p) will affect an elementary reaction differently than a combined reaction. In a single elementary reaction (recrystallization), increasing the (p) always increases the rate of recrystallization, as predicted by Equation 2.12 , since the driving force ($+f_R$) is directly proportional to (p). However, in a discontinuous combined reaction, this may not be true, since dislocations can act as nucleation sites for particles, with the average particle spacing equal to dislocation spacing. Then from Equations 2.12 and 2.14 ,

$$[(\delta f_R)/(\delta p)] \propto -[(\delta f_p)/(\delta p)]^2. \quad (2.16)$$

Thus, increasing (p) causes the retarding force ($-f_p$) to rise faster than the driving force ($+f_R$) which stabilizes the structure against discontinuous reactions, if the volume portion (V_p) precipitates at the dislocations. Many dislocations, not individual ones, produce the sites that are required for rapid nucleation. This implies the presence of a critical dislocation density (p_c). When $p < p_c$, a combined discontinuous reaction is initiated or accelerated. When $p > p_c$, a continuous combined reaction is possible and the discontinuous reaction is retarded or inhibited.

The interplay of driving and retarding forces means that this process can be heterogeneous, with the continuous reaction occurring in high dislocation density zones while the discontinuous reaction continues in another area. Either

process can follow the other, as time progresses, as seen in Figure 2.7. Thus, these two combined reactions can coexist and superplastic response may be a function of not just one process but of a combination of the two processes.

3. Time-Temperature-Reaction Diagrams

The interplay of driving and retarding forces, as functions of temperature and time, is best visualized by constructing a Time-Temperature-Reaction (TTR) diagram. A TTR diagram presents, for one alloy composition, the different reaction mechanisms which can occur and their kinetics. Figure 2.8 is a schematic TTR diagram which is adapted from Hornbogen [Ref. 49:p. 962], and is modified to reflect the critical temperatures (approximated). Curve shape is largely determined by the activation energies of these processes. As such, the curves presented here are schematic since little data is available to calculate their shape. Four critical temperatures are required to understand the TTR diagram: equilibrium temperature, (T_{DSC}); triple point temperature, marking the boundary between sequential and simultaneous combined reactions; test temperature, (T); and the transition temperature (T_{CRX}), marking the boundary between discontinuous and continuous, simultaneous combined reactions.

Continuous recrystallization (R_c) and discontinuous recrystallization (R_d) can occur sequentially or simultaneously with a precipitation reaction (D), with one exception, which occurs at temperatures above the equilibrium temperature (T_e).

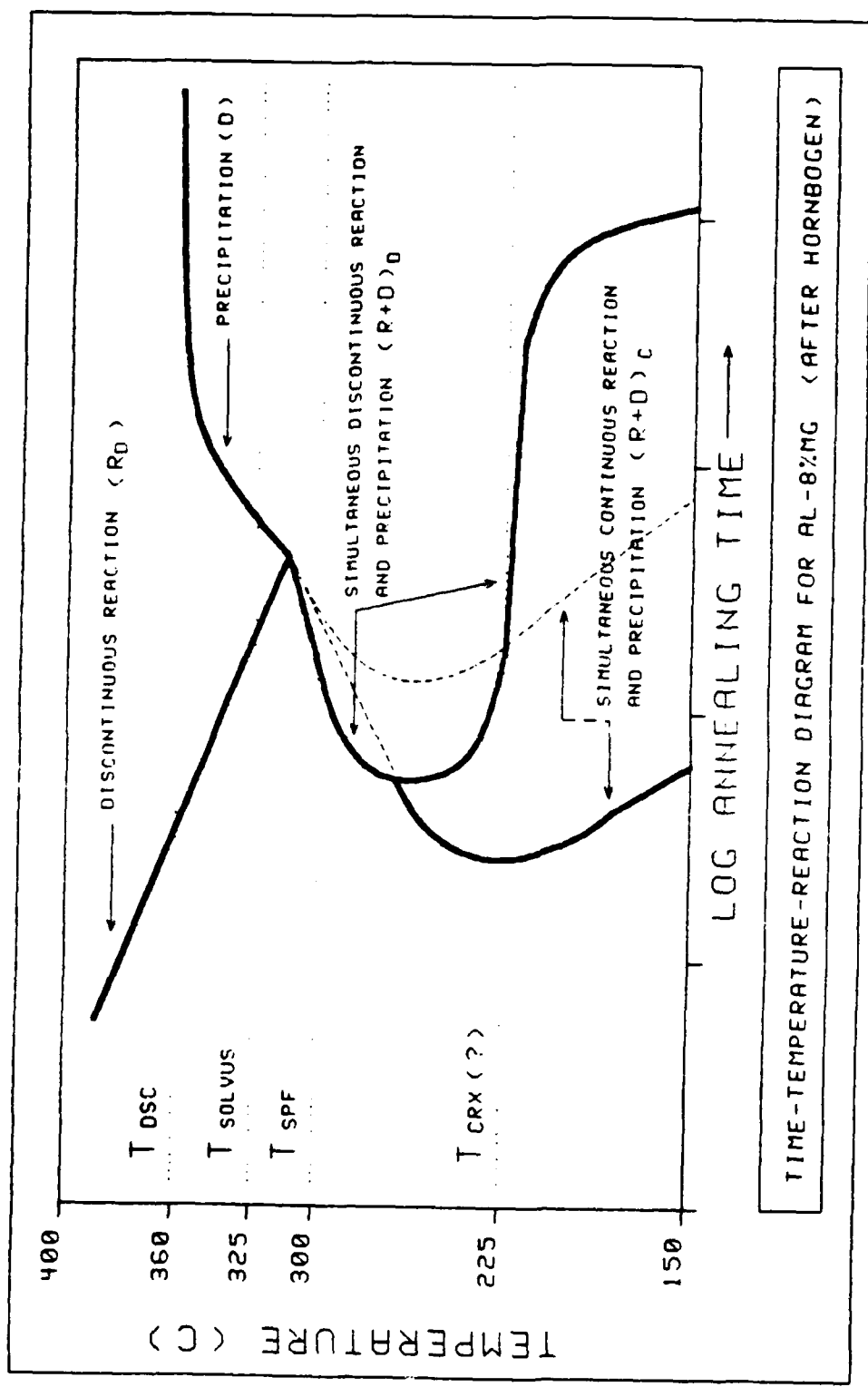


Figure 2.8 Time-Temperature-Reaction Diagram for Al-8%Mg-1%Li-0.2%Zr Alloy (adapted from Hornbogen)

For the Al-8%Mg-1%Li-0.2%Zr alloy, this is 360°C (T_{DSC}) [Ref. 22]. When the temperature (T) is greater than (T_{DSC}), no combined reaction occurs, sequential or simultaneous; only discontinuous recrystallization (R_d) occurs. At temperatures less than ($T < T_{DSC}$), combined reactions occur, either sequential or simultaneous.

The triple point temperature marks the boundary between sequential and simultaneous combined reactions. Above the triple point, sequential combined reactions occur. Below the triple point, simultaneous combined reactions take place. Increasing defect density (p) or decreasing solid solution concentration (x) decreases the triple point. Since this point is an unknown for the Al-8%Mg-1%Li-0.2%Zr alloy, it is located some where between 300 and 360 °C.

Based on a review of the DSC data from Munro, which shows the beginnings of an exothermic peak at 200°C that stabilizes at about 225°C, the transition temperature (T_{CRX}) is tentatively identified as 225°C [Refs. 22:p. 36; 42:p. 76; 43:p. 1597].

From Figure 2.8, it can be seen that a fast heating rate to test temperature, T_{SPF} (300°C), may initiate either a sequential ($R_d \rightarrow D$) or simultaneous combined ($(R+D)_d$) recrystallization. If the heating rate is slow enough, $(R+D)_c$ will occur. Additionally, other combined reactions can follow, resulting in a heterogeneous microstructure that is the result of competition between CRX and DRX.

4. Rolling Effects

As the billet is rolled, each pass results in a reduction in sample thickness. While the rolls are constant in size, their size relative to the sample's thickness increases. Large diameter rolls and high reductions tend to deform the bulk of the sample more than the surfaces, while small rolls and small reductions tend to deform the surfaces more than the bulk [Ref. 1:p. 344].

Since the amount of deformation (defect density, p) is a function of roll size, this implies that there is a variation in defect density across the sample thickness, which will lead to a variation in grain size. Bampton, et al., [Ref. 46:p. 198] found that rapid heating (greater than 5 °C/sec) produced finer grains near the surface, where the defect density was higher in 7075 Al, using the Rockwell process for DRX. With slower heating rates, a similar result may occur for CRX with a finer grain size found where defect density is highest, which is in agreement with Equation 2.17.

5. Ductility as a Function of Sample Thickness

In terms of the combined reactions model proposed, for CRX to occur, retarding forces have to dominate over the driving forces. For the Al-8%Mg-1%Li-0.2%Zr alloy, the large volume portion of finely distributed β particles found in the microstructure after TMP may help to increase retarding forces (see Equation 2.14). Retarding forces may also be increased

by increasing the true rolling strain (ϵ_{tr}). Since ϵ_{tr} is inversely proportional to sample thickness (t_{final}), decreasing t_{final} may cause greater ductility due to an enhancement of the CRX process, provided that sufficient reheating time between rolling passes is allowed for recovery and recrystallization to occur. Salama reported that increasing the true rolling strain from 1.5 to 2.5 increased ductility from 170% to 500% in an alloy (Al-10%Mg-0.1%Zr) tested at 300 °C [Ref. 18:pp. 105,114]. Munro reported a similar result in the Al-8%Mg-1%Li-.2%Zr alloy [Ref. 22:p. 20]. Salama attributed the enhancement of superplastic ductility to subboundaries better able to sustain grain boundary sliding as ϵ_{tr} is increased [Ref. 18:p. 133].

Equation 2.16 predicts that increasing defect density (ϵ_{tr}) can favor either DRX or CRX, depending on whether ϵ_{tr} is greater or less than a critical density. Figure 2.9 shows the two competing reactions (DRX/CRX) as functions of ϵ_{tr} . In addition, a linear superplastic response may be possible according to the model proposed, if the defect density is sufficient. The lower part of the curve, found at high true rolling strains, can be linearized as shown by the dotted tangent line. Thus, increasing ϵ_{tr} in this region may result in a linear increase in the percentage of CRX occurring with a corresponding linear increase in superplastic response, while at lower true rolling strains an exponential increase in CRX and ductility may occur with small increases in strain.

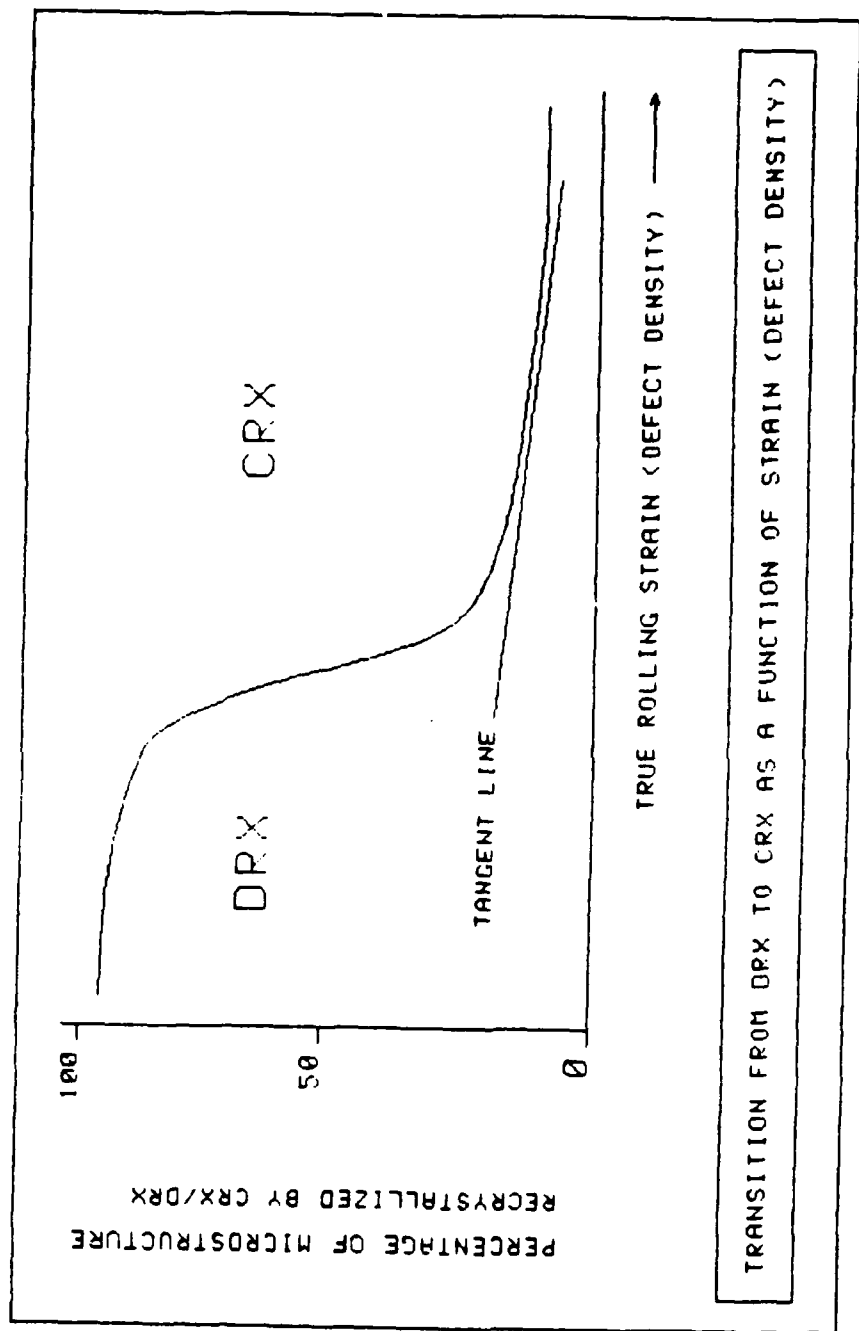


Figure 2.9 Transition from DRX to CRX as a Function of True Rolling Strain (adapted from Hornbogen, p. 966)

6. Average Grain Size and SPD Response

The grain size of a sample will probably not be uniform through out the sample. Rather, one should expect to find a variation throughout the sample depending upon which recrystallization process was favored, and for how long it was favored, in the various parts of the sample. Given a proven TMP and SPF scheme for an alloy, variations in superplastic response may still occur, due to CRX or DRX being favored over the other. These variations in superplastic response may be due to: defect density as a function of alloying (incomplete homogenization); defect density as a function of rolling strain (sample reduction variances); defect density as a function of changing rolling geometry; and variances in heating rate to SPD temperature. While Munro [Ref. 22] and Ferris [Ref. 21] both worked with the same alloy, Munro reported a much greater homogeneity of grain size than did Ferris. Ferris reported that his heating rate was significantly faster than Munro's, which is in accord with the background just developed.

E. CURRENT RESEARCH

From previous research at NPS, it has been established that CRX occurs during the TMP, specifically during the heating between rolling passes, and that the fine grained microstructure present after the last pass is the cumulative result of a series of deformation and recrystallization

cycles. Reheating the sample to test temperature initiates the final recrystallization process, resulting in a very fine grained microstructure capable of sustaining a superplastic response.

The focus of this study is to determine what happens to test samples as the heating rate to test temperature is varied, and interpret the responses in terms of the DRX and CRX processes. It is hoped that this information will give further insights to understanding the microstructural evolution that occurs during reheating.

III. EXPERIMENTAL

A. MATERIAL PROCESSING

The Al-Mg-Li-Zr alloy used in this study was prepared by the Naval Surface Weapons Center (NSWC), White Oak, Maryland. It was cast in a graphite mold at room temperature, under an argon atmosphere. Aluminum (99.99% pure) was induction melted in a graphite crucible. Magnesium and lithium were added as pure metal bars, with zirconium added using an Al-Zr master alloy. Several different alloy compositions were specified. [Ref. 50]

Analysis of the Al-8%Mg-0.5%Li-0.15%Zr alloy was performed by Anamet Laboratories, Berkeley, California. Five samples were taken from radial positions of a disk cut from the ingot's center, normal to its long axis. The samples were subjected to atomic absorption and x-ray analysis. Deviations from the nominal composition were within acceptable tolerances. The average Zr concentration was 0.23 weight percent, with Mg and Li averaging 8% and 0.5%, respectively. As a result, the other alloys prepared by NSWC are assumed to have nominal compositions of similar accuracy. For the alloy used in this study, composition is assumed to be Al-8%Mg-1%Li-0.2%Zr, weight percent. [Ref. 51]

1. Thermomechanical Processing

Two forging billets, each measuring 2.6 x 2.6 x 8 cm, were machined from the as-cast ingot. Thermomechanical processing (TMP) was in accordance with Figure 2.5. Solution treatment was performed in a preheated, equilibrated furnace with a heavy steel plate on the hearth to provide thermal mass and thus minimize the effect of drafts.

Upset forging was performed by a two man team, to minimize time out of the furnace. The forge platens were pre-heated and equilibrated at the solution treatment temperature (480°C) before the upset forging was conducted. Billets were removed from the furnace and sprayed with anti-seize compound just prior to upset forging to 30% of original billet height. The billets were cold-water quenched after a final one hour solution treatment. The billets were strongly agitated during the first few seconds of quenching. Figure 3.1 shows the two billets after forging, with the measurements made at the indicated locations. Measurements were made with a Starrett micrometer, averaged and recorded, as indicated in Figure 3.1. No problems such as cracking or non-uniform deformation were encountered, and minimal time was spent out of the furnace, due to the excellent release properties from the anti-seize spray.

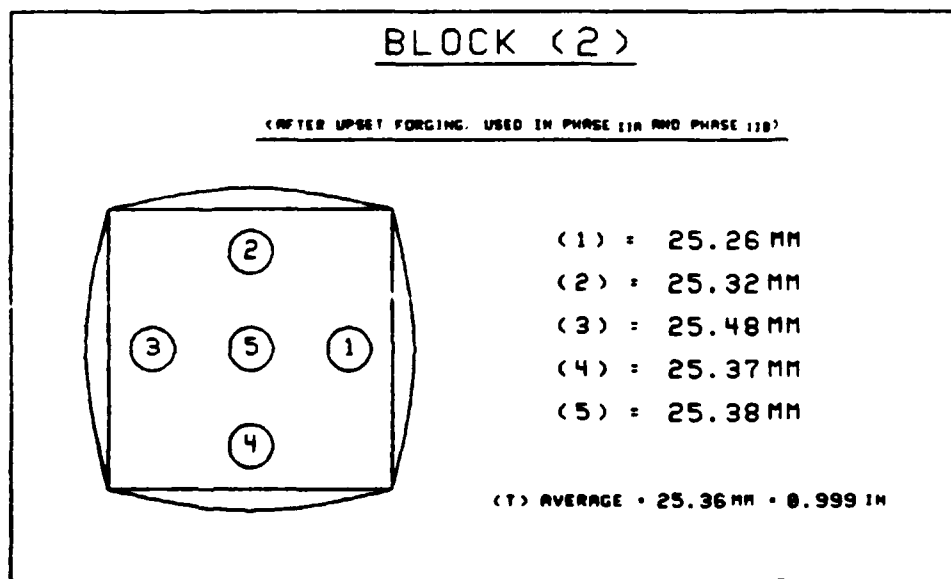
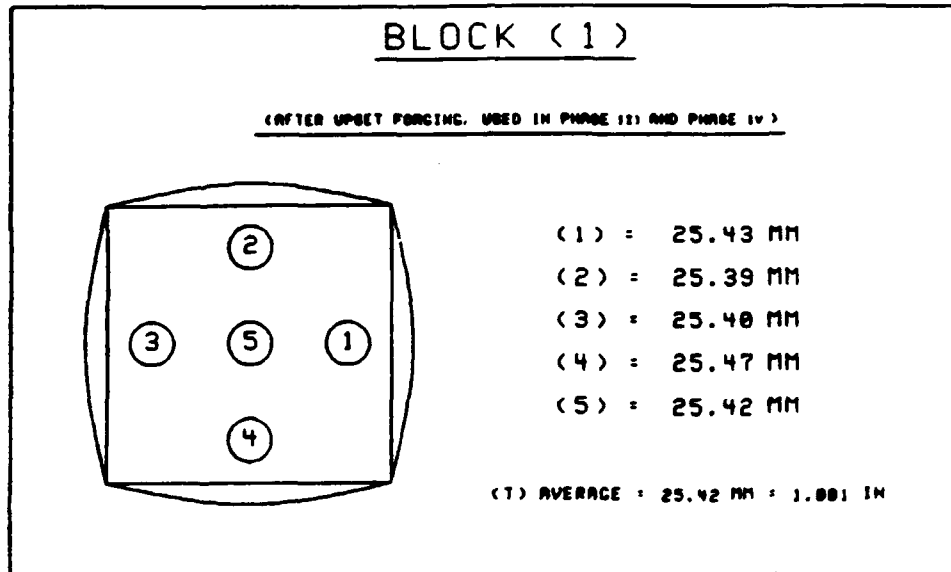


Figure 3.1 Billet Geometry After Upset Forging

A scheme for subsequent rolling was established based on the strain desired in the final rolled sheet. Knowing that the final true rolling strain (ϵ_{tr}) is defined as

$$\epsilon_{tr} = \ln (t_{initial}/t_{final}) \quad (3.1)$$

and knowing ϵ_{tr} (desired = 2.5) then,

$$t_{final} = t_{initial} (e^{-2.5}) \quad (3.2)$$

where (t_{final}) is the final billet thickness after rolling, and ($t_{initial}$) is the billet thickness after upset forging.

The billets were then placed in a calibrated furnace that had a large steel plate in it, for thermal mass to minimize variations due to drafts and to maximize recovery during the each of the 30 minute reheat periods.

Heated billets were placed in a two-high rolling mill, with 4.3 inch diameter rollers. Billets were reduced approximately 2.5 mm per pass, with the final pass adjusted to give a final ϵ_{tr} of 2.5. Rolling mill speed was set at medium. After the fifth rolling pass, when the billets had become significantly longer and thinner, curling began as the billet exited the rolls. To control this curling, a second man was stationed at the mill exit to place a wooden block flat on top of the billet as it rolled out. This kept the billet sheet relatively flat. After each pass through the rolling mill, the billet was placed back in the furnace with measurements made of the thickness per pass and recorded, using a dial

caliper for speed. The billet end entering the rolling mill was alternated with each pass in an effort to maintain isothermal conditions. A total elapsed time of no more than 45 seconds was maintained with the billet out of the furnace, with the exception discussed next.

Table 3.1 summarizes the rolling sequence and difficulties encountered in the two billets, Block 1 and Block 2. Rolling was faultless until the ninth step, when stalling occurred with Block 2 in the middle of the roll process. Emergency action was taken with the mill wrench to open up the mill as quickly as possible and put it back into the furnace until the mill was recalibrated. Another stall occurred at step 12, and the effort was terminated at the 14th step with a final rolling strain of 2.4. The last two passes for Block 2 were done at the slowest speed possible, to ensure maximum torque.

Block 1 stalled in the middle of the 10th, and last, pass. It was taken from the mill and quenched, to "freeze" the microstructure. During the removal process, Block 1 broke into two parts. Part 1 had completed the last rolling pass with a final rolling strain of 2.47. Part 2 was rolled one more time with a final rolling strain of 2.51.

Alligatoring occurred in both blocks, with Block 1 being the worst. Alligatoring in one end of Block 1 was over two inches long. Some alligatoring occurred in Block 2, but only for half an inch. No other rolling defects were noted.

TABLE 3.1
SUMMARY OF ROLLING HISTORY

Step Number	Reheat Time	Block 1	Block 2
1	30 min	roll	roll
2	30 min	roll	roll
3	30 min	roll	roll
4	30 min	roll	roll
5	30 min	roll	roll
6	30 min	roll	roll
7	30 min	roll	roll
8	30 min	roll	roll
9	30 min	roll	STALL
10	30 min	STALL & BREAK	calibrate
.	.	.	.
.	.	.	.
.	.	Part 1	Part 2
.	.	_____	_____
11	30 min	completed	roll
12	30 min		completed STALL
13	30 min		roll
14	30 min		roll
$\epsilon_{tr} =$		2.47	2.51

No stalling was reported by Munro or Ferris. The same mill speed was used by Groh and Regis with 2090 Al, with no stalling reported.

2. Tensile Sample Geometry

Tensile samples were prepared from the rolled billets by the NPS machine shop. Billet edges and ends were trimmed before cutting the sample blanks. Blanks were cut with the

longitudinal axis of the gauge section parallel to the rolling direction of the billet. Final shaping of the samples was performed on an end mill, in accordance with the dimensions in Figure 3.2. This tensile sample geometry has been standardized at NPS, which enables comparisons to be made between researchers. Tensile sample surfaces were not machined or prepared in any manner.

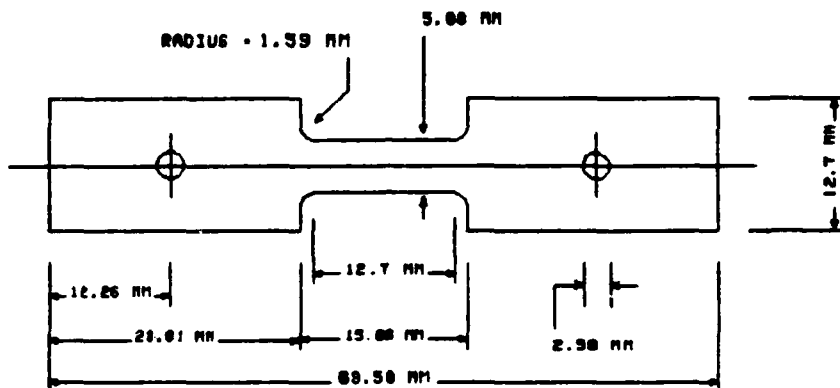
Thickness and width of all sample gauge sections were measured and recorded, using a Starrett micrometer (model 436 --25 mm). The gauge section was scribed with two lines 0.5 inches apart for measurement after SPD testing.

B. ELEVATED TEMPERATURE TESTING

Testing was performed in a constant crosshead velocity Instron tensile testing machine using a 1000 pound load cell. The Instron machine was calibrated in accordance with manufacturer's specifications before each series of tests. Samples were mounted in special wedge grips and grip extensions made by ATS, Butler, Pennsylvania from Inconel 718 [Ref. 52:pp. 30-31].

Once mounted in the Instron, the tensile sample, grips and portions of the grip extensions were enclosed in a Marshall three-zone clamshell furnace (model 2232) that was mounted on the Instron frame. Furnace temperature (300° C) was maintained using three separate controllers, one for each of the three heating element sets in the furnace. Monitoring of

TENSILE SAMPLE GEOMETRY (MM)



TENSILE SAMPLE GEOMETRY (IN)

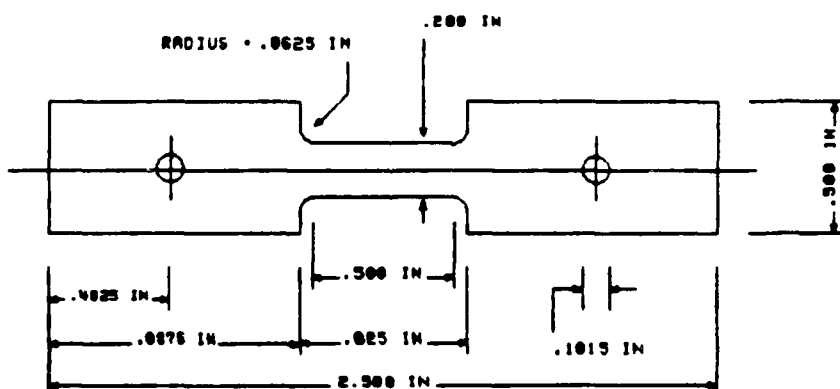


Figure 3.2 Tensile Testing Sample Geometry

temperatures in the furnace was done with four thin ($d = 1.57$ mm) type K Chromel-Alumel thermocouples. One thermocouple was placed on each of the grip sections holding the wedges, and one thermocouple was placed on a shoulder at each end of the sample's gauge section. Test temperature (300°C) was maintained to within $+/- 1\%$ accuracy in all cases, with variances from test temperature usually on the order of $+/- 1^\circ\text{C}$ ($+/- 0.33\%$).

Three crosshead speeds (v) were used: 0.02 in/min, 0.2 in/min and 2.0 in/min, corresponding to initial strain rates of $6.67\text{E-}4 \text{ s}^{-1}$, $6.67\text{E-}3 \text{ s}^{-1}$ and $6.67\text{E-}5 \text{ s}^{-1}$. Initial strain rates were calculated using the relation:

$$\dot{\epsilon} = d\epsilon/dt = v/(60 L_0), \quad (3.1)$$

where (v) is crosshead speed and (L_0) is initial gauge length (0.5 in). Chart speeds used were (respectively): 0.2 in/min, 2.0 in/min and 20.0 in/min, giving a constant magnification ratio ($MR = \text{chart/crosshead speed}$) of 10.

C. TENSILE TESTING DATA REDUCTION

Elevated tensile testing data reduction was performed in accordance with Spiropoulos [Ref. 53] and Chawla [Ref. 54]. Actual sample elongation was calculated using the following equation:

$$\% \text{Elongation} = 100(L_f - L_0)/L_0 \quad (3.2)$$

where (L_f) is the final measured gauge length and (L_o) is the initial gauge length (0.5 in). A "floating slope" was used to correct raw Instron data for machine variables, grip slippage and sample elasticity. A correction factor (c) was computed to compensate for machine and specimen stiffness, using the following relation:

$$c = (L_f - L_o)(MR)/X_{\text{measured}} \quad (3.3)$$

where (MR) is the magnification ratio, ($L_f - L_o$) is the actual measured elongation of the sample and (X_{measured}) is the distance on the strip chart x-axis, at zero load, from the intercept of the "floating slope" line to the end point of the test run, where the load drops off to zero. Engineering stress (S) was calculated using the relation:

$$S = P/A_o \quad (3.4)$$

where (P) is load (y-axis of strip chart) and (A_o) is the initial cross sectional area. Engineering strain (e) was calculated as:

$$e = (L_f - L_o)/L_o. \quad (3.5)$$

True strain (ϵ) is defined as:

$$\epsilon = \ln (1 + e). \quad (3.6)$$

And, true stress (σ) is defined as:

$$\sigma = S (1 + e). \quad (3.7)$$

Instron strip charts were examined, and data points were recorded in a computer raw data file. Raw data was reduced using the BASIC program found in Appendix A. Output of this data was used to generate true stress versus true strain plots, using the NPS mainframe EASYPLOT graphics program.

D. HEATING RATE TO TEST TEMPERATURE

The heating rate resulting from previous procedures used at NPS has been described as the time it takes to go from room temperature to test temperature. Sanchez [Ref. 20:p. 19] described the heating interval he used as the 45-60 minutes required to reach test temperature (300°C) equilibrium, after placing the tensile sample in a preheated furnace. Spiropoulos [Ref. 53:p. 33] described his heating rate in terms of the approximate 90 minutes required to reach equilibrium at test temperature (300°C) from a cold furnace for the first test, with subsequent tests requiring 30-40 minutes to reach equilibrium. Munro [Ref. 22] makes no specific comment on the heating rate used. Ferris [Ref. 21] theorizes that his Al-8%Mg-1%Li-0.2%Zr alloy samples' coarser microstructure might be due to a faster heating rate used, perhaps by three orders of magnitude, than Munro's.

1. Heating Rate Data Collection

Estimates of the heating rates used in previously cited studies were made using the following definition:

$$\dot{T} = (T_{SPF} - T_{ROOM})/t_{\Delta} \quad (3.10)$$

where (T_{SPF}) is the SPF test temperature in °C, (T_{ROOM}) is the room temperature in °C and ($t_{delt.}$) is the time required to go from T_{SPF} to T_{ROOM} in seconds (s). From this and assuming (T_{ROOM}) averages 22°C in the Instron machine room, previous heating rates can be approximated as ranging from 1.54E-1 °C/s (30 minutes) to 1.03E-1 °C/s (45 minutes).

All heating rates used in this study were determined by attaching a Type K Chromel-Alumel thermocouple along the length of a tensile test sample with thin ($d = 0.315$ mm) pieces of Chromel-Alumel wire. The thermocouple tip was placed so that it and 0.5 inches of the thermocouple was covering the length of the 0.5 inch gauge section. The sample used was of the same material to be used in tensile testing and fabricated from the discarded end of Block 1, Part 1, in accordance with Figure 3.2. No alligatoring was present which might introduce surface effects variables. A thin ($d = 1.57$ mm) thermocouple was used to minimize time response to temperature changes. Since the samples ranged in thickness from 2.0-2.3 mm, thermocouple size was well within guidelines recommending a diameter no greater than 1.5 times the sample's minimum gauge [Ref. 55:p. 711].

Heating rate data was recorded using a Hewlett-Packard HP-3852A Data Acquisition System, with an HP-9000 Series 300 computer for data analysis. Data analysis was performed by a HP BASIC program (TIME-TEMP) written by Mr. Thomas Kellogg, of NPS, which is available in that laboratory. Data output was

generated on an HP Think-Jet printer, and plotted on the NPS mainframe printer using the EASYPLOT routine.

2. Standardized NPS Heating Rate (10^{-1} °C/s)

For the purposes of this study, the baseline heating rate is the one generally described by Sanchez and Spiropoulos. The method for arriving at this heating rate is discussed in detail in the next paragraph.

The room temperature furnace is closed around empty grip extensions. Then the furnace is turned on and heating of the grip extensions and thermocouples commences until equilibration to test temperature is verified, which typically takes 90 minutes. The furnace element controllers are not touched thereafter, except for minor adjustments to achieve equilibration. The furnace is turned off when equilibration has occurred, before opening it up, by securing power to the controllers. This prevents the furnace from over heating and subsequently initiating a faster heating rate than desired. The sample is fitted in the room temperature grip wedges and placed in the bottom grip extension. Then the sample and wedges are levered up into the bottom grip extension, from the bottom, to ensure a tight fit for better heat transfer and to minimize grip slippage. Care is taken during the levering process to ensure that the sample is aligned vertically. The remaining grip wedges are fitted on the top section of the sample, and the crosshead is moved up until the wedges-and-sample assembly fits into the top grip extension. The

crosshead is lowered slowly, while monitoring the strip chart pen (making sure that it is on) until the assembly has seated. The furnace is then closed around the grip extensions, sealed with insulation and power is turned on. Test temperature (300°C) is generally reached in 30 minutes, with equilibration achieved in 45-60 minutes.

Adjustments to controller settings is occasionally required to compensate for heat losses from the top and bottom entries to the furnace. Fiberfax insulation applied around the top of the furnace minimizes losses due to drafts (chimney effect) and due to radiation/convection from the exposed top grip extension. Fiberfax applied as a collar in the top and bottom access areas of the furnace further minimizes heat losses, as long as care is taken to ensure there is no binding on the grip extensions. More adjustments (negative) to the bottom controller are typically required when elongations greater than 600% are occurring, since the bottom thermocouples are now exposed to two heating elements sets (middle and bottom) instead of just one set (middle).

During the heating cycle, the bottom thermocouples indicate a slower heating process than at the top. This may be due to the greater mass at the bottom (longer grip extension, large crosshead) and heat being convected upwards by the chimney effect, in spite of the Fiberfax.

3. Heating Rate Selection

In designing the experiment, it was decided that five heating rates would be used, with the standardized NPS heating rate a baseline. The four additional heating rates would give a spectrum spanning five orders of magnitude, +/- two from the baseline. General heating rates desired were: 10^{-3} , 10^{-2} , 10^{-1} , 10^0 , 10^{+1} °C/s.

A preliminary investigation was initiated to find standardized methods for achieving the four additional heating rates. For the two heating rates slower than the baseline (10^{-3} , 10^{-2}), the same heat source found in the standardized NPS heating rate was used, except preheating was not required. However, some heating source other than the clamshell furnace was required for the two faster heating rates (10^0 , 10^{+1}). Options considered were induction heating, salt baths and radiant heaters.

4. Standardized 10^{-3} °C/s Heating Rate

This heating rate follows the same methodology as described for the standardized NPS heating rate, except the sample was placed in a room temperature furnace. Analysis indicated that a $1(10^{-3})$ °C/s heating rate would require far too much time (+70 hours), so a heating rate closer to $1(10^{-2})$ °C/s seemed a more practical choice. A 12 hour heating time was arbitrarily selected as a goal, giving an approximate heating rate of $7(10^{-3})$ °C/s. Since the controllers are not

automated, a simple linearized scheme was used. Heating occurred in six 50°C steps, with two hours per step.

5. Standardized 10⁻² °C/s Heating Rate

The methodology for this heating rate was suggested by Spiropoulos, since 90 minutes heating time to 300°C from a cold furnace works out to an approximate heating rate of 5(10⁻²) °C/s. The furnace has a dummy sample placed in the grips for proper thermocouple positioning, and then is heated to test temperature. Once equilibration is verified, power is turned off. The actual sample is then placed in the cold furnace, and power is turned on, heating to test temperature in one step.

6. Standardized 10° °C/s Heating Rate

Extensive experimentation demonstrated that the most viable method for attaining this heating rate in the Instron apparatus was with a two step procedure. First, the sample would be heated at the rapid rate desired, air cooled, and then at a later time heated to test temperature in the clamshell furnace.

Since the driving force for microstructural changes such as recrystallization arise from the initial, fast heating rate, in this case from the radiant heater, then the slower heating rate used later should have little effect upon recrystallization, if the time in the radiant heater is sufficient for the reaction to finish. The theoretical basis

for this has already been developed in Chapter II. In addition, this concept has been validated by Bampton, et al. [Ref. 46].

Extreme care must be used with this method, since there are many variables that require control. Five direct variables have been identified during experimentation, all dealing with the equipment involved.

A RI Controls Quad Elliptical Radiant Heating Furnace, Model E4-10, was the heat source. Coolant flow was automatically controlled at a rate of 0.1 GPM/kW output. The inlet water temperature is a variable. However, temperature for this series of experiments was a consistent 19°C. More importantly, the quartz glass liner tube frequently begins to deform and become opaque at very high power settings which slows down the heating rate at a given power level.

Power to the radiant heater is controlled in two ways. Power level is controlled as a percentage of power available by a vernier dial, manually set. Power cutoff and reset are controlled by a thermocouple actuated controller. The combination of these two control mechanisms allows heating rates of the magnitude desired to be achieved. However, a certain amount of overshoot (to 310°C) occurs after reaching the desired temperature, with subsequent cycling around the desired temperature (+/- 8°C) as the power cycles on and off.

Better control of overshoot and thermal cycling was achieved by adding a fifth variable: a stainless steel sheet

metal liner inside the quartz glass tube. The additional thermal mass reduced the overshoot to 8°C or less, and cycling to one minute periods of +/- 3°C.

Samples were placed in the calibrated preheated radiant heater, and data points were manually recorded. A five minute reaction time was added to the time it took to reach test temperature (300°C). The five minutes (300 seconds) was arbitrarily chosen. It was anticipated that 300 seconds would be sufficient if DRX is occurring due to the fast heating rate. The sample was allowed to air cool after removal from the heater. Sample temperature was monitored using a thermocouple attached in the manner previously discussed, with a calibrated digital readout.

7. Standardized 10⁺¹ °C/s Heating Rate

For this heating rate, experimentation indicated that the best method was the same two step procedure, using a salt bath instead of the radiant heater. Thermocouples used in salt baths should be enclosed in suitable protective tubes for corrosion protection. However, this decreases the thermocouple's response to temperature changes, so no protective tube was used.

A nitrate-nitrite mixture salt bath was heated to test temperature and equilibrated for 15 hours. Samples were placed in the salt bath and held in the middle of the liquid for five minutes (300 seconds), measuring from the time the samples entered the liquid. Samples were air cooled after

removal from the salt bath, and the salt residue was removed by ultrasonic cleaning in soapy water. [Ref. 55:pp. 710-711]

Molten salt baths present hazards [Ref. 55:p. 711] which careful laboratory procedure will reduce. Good ventilation is essential with molten nitrate salt baths, due to the nitrous fumes produced. Overheat controls should be installed to prevent heating beyond 595°C. At the very least, controller settings and temperature scales should be double checked. Explosions have occurred from physical and chemical reactions. Therefore, samples must be clean, dry and free from cavities or pockets. Finally, most authorities do NOT advise using molten nitrate salt baths with aluminum alloys containing more than a few percent magnesium, especially if temperatures are sufficient to result in melting of the alloy. No reaction was observed with this 8% Mg alloy, but caution is strongly advised. Mild electric shocks were encountered when touching the thermocouple with bare hands as the thermocouple made contact with the metal pot, while still immersed in the molten liquid.

If the pot is suspected of weakness due to accelerated corrosion from the highly oxidizing salt, ensure that a dam is placed around the bath to contain any spills.

E. EXPERIMENTAL DESIGN

Four series, or phases, of experiments were conducted for this study. Each of the four phases was designed to meet at

least one specific objective. All four phases used a 300°C test temperature.

The first phase's objectives were two-fold: to repeat a portion of Munro's work and to determine what would happen to superplastic ductility if his heating rate to test temperature was varied by either increasing or decreasing the rate by two orders of magnitude. The procedures for the remaining three phases were designed after analysis each of the preceding phases.

A labelling system was developed and used in this study to ensure that each sample's processing history and testing parameters are known by looking at the sample's label. The nomenclature used consists of a three-part identifier. The first part identifies the testing phase, and therefore the experimental matrix to consult, and the sample's processing history. The second part identifies the sample's location within the experimental matrix; that is, what were the parameters used on the sample in question. The third part identifies the run number for a given set of parameters already identified in the second part; that is, was this the first, second or third try under the stated conditions. For example, sample I/8/B is the sample used in Phase I, under conditions defined by the number 8 position in the Phase I matrix, and was the second attempt (run) under those conditions. This labelling system will be used in the following descriptions of the experimental matrices used in this study,

and in Chapters IV and V when discussing results. The matrices appear in the following subsections.

1. Phase I

In this phase, experimental design centered on the fact that Munro reported exceptional ductility (1000+) with this alloy undergoing SPD at 300°C at an initial strain of 6.67 (10^{-3}) s^{-1} , using the nominal NPS heating rate (10^{-1} °C/s) [Ref. 22:p. 47].

A 3x3 matrix (Table 3.2) was designed around this result, using tensile test samples prepared by Munro. These samples were reported to have a nominal final rolling strain (ϵ_{tr}) of 2.45 to 2.8, using the NPS TMP previously described, with a reduction of 2.5 mm per rolling pass [Ref. 22:pp. 27-28]. Two variables were studied: the initial strain rate and the heating rate to test temperature.

TABLE 3.2
PHASE I EXPERIMENTAL MATRIX

Heating Rate	Strain Rate		
	6.67E-4	6.67E-3	6.67E-2
10^{+1} °C/s	I/1/A	I/2/A	I/3/A
10^{-1} °C/s	I/4/A	I/5/B	I/6/A
10^{-3} °C/s	I/7/A	I/8/B	I/9/A

2. Phase II

Based on results of Phase I, the Phase II matrix focused on heating rate alone, using the initial strain rate that gave the peak ductility, $6.67 \times 10^{-3} \text{ s}^{-1}$. Tensile test samples for this phase were machined from Block 2 material, which had a final rolling strain (ϵ_{tr}) of 2.41. Heating rates were those used in Phase I with a fourth rate added.

A subset of this phase was designed to determine the effect of varying equilibration time (t_{equil}) at test temperature. The most readily controlled and consistent heating rate ($10^{-2} \text{ }^{\circ}\text{C/s}$) was used. This experimental matrix is presented in Table 3.3.

TABLE 3.3
PHASE II EXPERIMENTAL MATRIX

Strain Rate = $6.67 \times 10^{-3} \text{ s}^{-1}$					
Heating Rate	Equilibration Time (t_{equil})				
	As Required	10 min	20 min	45 min	
$10^{-4} \text{ }^{\circ}\text{C/s}$	II/1/A				
$10^{-2} \text{ }^{\circ}\text{C/s}$		II/2/B	II/2/C	II/2/A	
$10^{-3} \text{ }^{\circ}\text{C/s}$	II/3/A				
$10^{+1} \text{ }^{\circ}\text{C/s}$	II/4/A II/4/B				

3. Phase III

This phase of experiments was conducted to determine if a transition in ductility seen in Phase II occurred at a heating rate of 10^0 °C/s, i.e., between 10^{+1} °C/s and 10^{-1} °C/s, as indicated in Phase II. The three samples in this phase were fabricated from Block 1, Part 1 material. The final rolling strain for these samples was 2.47.

Since rolling temperature during TMP varies with transfer of samples from the furnace to the mill, this phase was designed to eliminate that variable. The three samples were fabricated from a section of Block 1, Part 1, that was wide enough to allow three samples to be made from three sections that lay beside each other. That is, the three samples passed through the rolling mill at exactly the same time under exactly the same TMP conditions.

In addition, there was an inverse relationship noted in Phase II between sample gauge thickness and superplastic ductility; that is, the thinner the sample, the greater the ductility. The three samples in this phase were ranked according to thickness, where III/1/A was the thinnest and III/3/A was the thickest. If heating rate dominated over thickness, then the best ductility would be seen in the slowest heating rate and the worst ductility in the fastest heating rate. If thickness of sample dominated, then the best ductility would be seen in the thinnest sample. In essence, this series was a discriminator that was intended to determine

the design of the fourth and last phase of experiments, while eliminating the rolling variables.

The experimental matrix for Phase III is presented in Table 3.4. An initial strain rate of $6.67(10^{-3}) \text{ s}^{-1}$ was used for all samples. Phase III and Phase IV procedures were designed with the assistance of the Department of Operations Research at NPS.

TABLE 3.4
PHASE III EXPERIMENTAL MATRIX

Heating Rate	Sample Thickness	Sample
$10^{+1} \text{ }^{\circ}\text{C/s}$ (3)	2.275 mm (1)	III/1/A
$10^0 \text{ }^{\circ}\text{C/s}$ (2)	2.285 mm (2)	III/2/A
$10^{-1} \text{ }^{\circ}\text{C/s}$ (1)	2.315 mm (3)	III/3/A

4. Phase IV

The objectives of this final phase were to confirm that the heating rate of $10^0 \text{ }^{\circ}\text{C/s}$ was the transitional heating rate for ductility and to further explore the relationship between the sample location, relative to the rolling strip, and superplastic ductility.

The matrix for this phase is presented in Figure 3.3, with sample location, sample label and heating rate indicated in each schematic sample tab. Three heating rates (10^{-1} °C/s, 10^0 °C/s, 10^{+1} °C/s) were used for each of the three rows of three samples. The samples were fabricated from Block 1, Part 2 material, with a final rolling strain of 2.41. Each row represents a slightly different TMP, since the rolling mill is heating up as the block is cooling down as it passes through the rolls. Variables tested were: the location that a given heating rate was used within a row of samples, and rolling conditions for the metal sheet as it passed through the rolling mill. Heating rate distribution was fully randomized to ensure that all possible variations of heating rate distribution for the experimental matrix were considered. No matrix position was favored so that heating effects were separated from any positional effects upon ductility. Additionally, this enabled a detailed examination to be made of the assumption that isothermal conditions exist during rolling TMP. An ordered, non-randomized matrix can be represented as:

a	b	c
a	b	c
a	b	c

whereas a fully randomized 3x3 matrix can be represented as

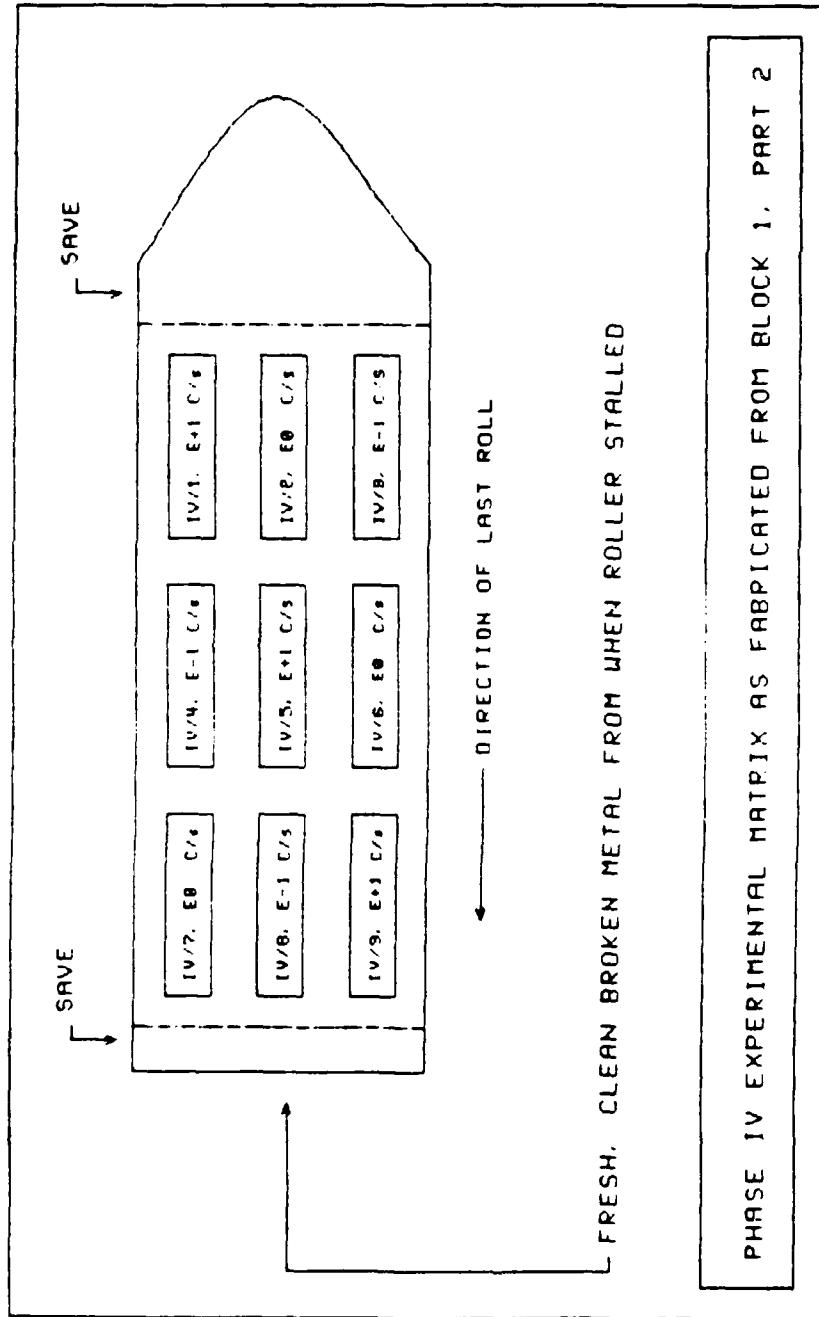


Figure 3.3 Phase IV Sample Layout for Fabrication from Block 1, Part 2, and Heating Rates Used for Each Sample During Testing

a b c
c a b
b c a

which ensures a complete distribution across the three locations in each row. In addition, this phase investigated the assumption that rolling is a uniform process by examining gauge thickness as a function of position.

F. STATISTICAL ANALYSIS

The validity of any study has to be protected by eliminating or minimizing errors and randomness during the experimental process and during data analysis. For this study, meticulous attention was paid to following the experimental methods. To this end, documentation of methods used has been extensive, since randomness in results is often caused by a lack of definition of methods. This can lead to poorly controlled or uncontrolled variables with subsequent changes in experimental conditions [Ref. 57:pp. 17,266].

In this study, data were analyzed graphically by plotting actual values against each other to determine what relationships existed. Precision data analysis was performed on a Hewlett-Packard HP-15C scientific calculator, using preprogrammed routines to calculate linear regressions and correlation coefficients. Data were also ranked in order of importance (ductility, heating rate) or size (thickness of sample gauge) and the coefficient of rank correlation was

calculated using Spearman's formula [Ref. 58], as a check on the precision calculations that were used for reporting purposes.

When data were taken from the Instron strip charts during data reduction, all points were generated by linearizing the curve. A straight edge was placed tangent to the curve, and data points were recorded for the locations where the straight edge and curve no longer coincided.

IV. RESULTS

A. HEATING RATES

Five heating rates were used to investigate the effect of heating rate on superplastic response of the Al-8%Mg-1%Li-0.2%Zr alloy as it was heated to test temperature (300°C) from room temperature. The procedures for achieving these five heating rates were standardized, with three heating rates (10^{-1} °C/s, 10^{-2} °C/s, 10^{-3} °C/s) attained using the Instron mounted clamshell furnace. The two fastest heating rates (10^{+1} °C/s and 10^0 °C/s) were beyond the capabilities of the clamshell furnace, and required different heating sources (salt bath for 10^{+1} °C/s and radiant heater for 10^0 °C/s). Subsequent, slower reheating to test temperature in the test facility was not expected have an undesirable effect upon recrystallization in the test samples. Only two of the five heating rates (10^{-1} °C/s, 10^{-2} °C/s) are commonly used at NPS. Figures 4.1-4.5 show typical thermocouple plots resulting from the five heating rates used. Heating rate values were calculated by computing the difference between 300 °C and the room temperature and then dividing the difference by the time taken to first attain 300 °C.

Figure 4.1 is representative of the most commonly used heating rate in research at NPS, where samples are placed in

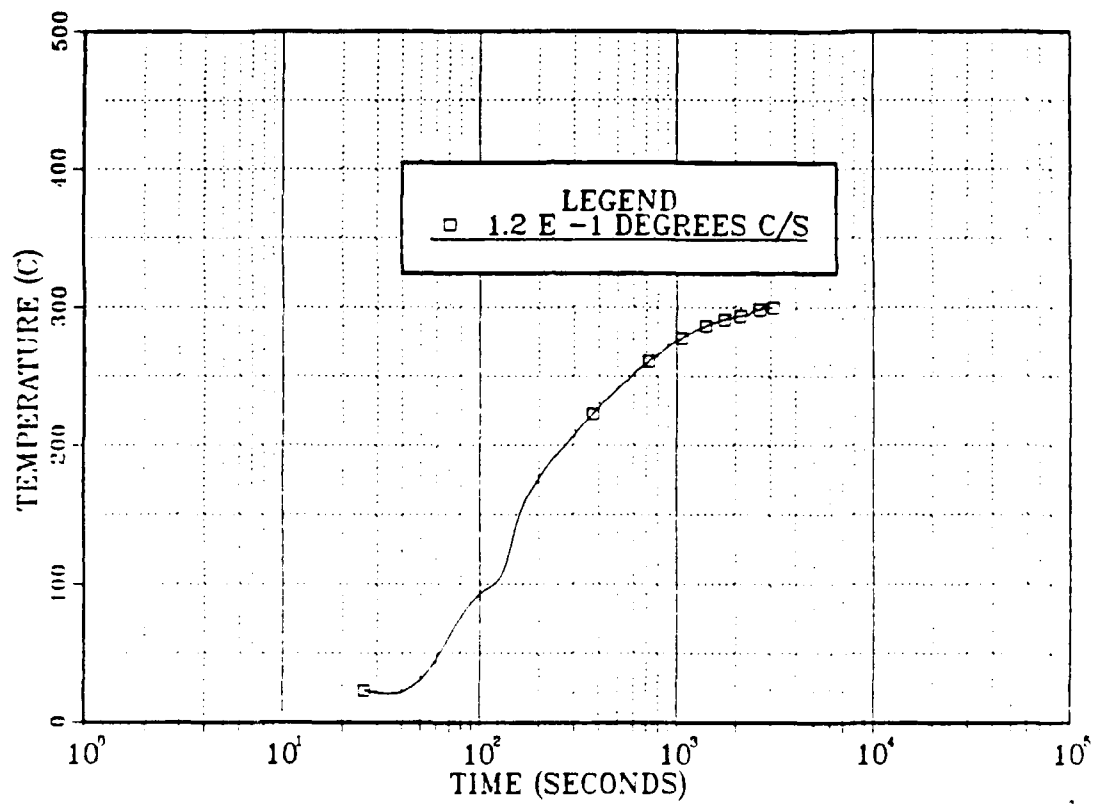


Figure 4.1 Standardized NPS Heating Rate ($10^{-1} \text{ } ^\circ\text{C/s}$)

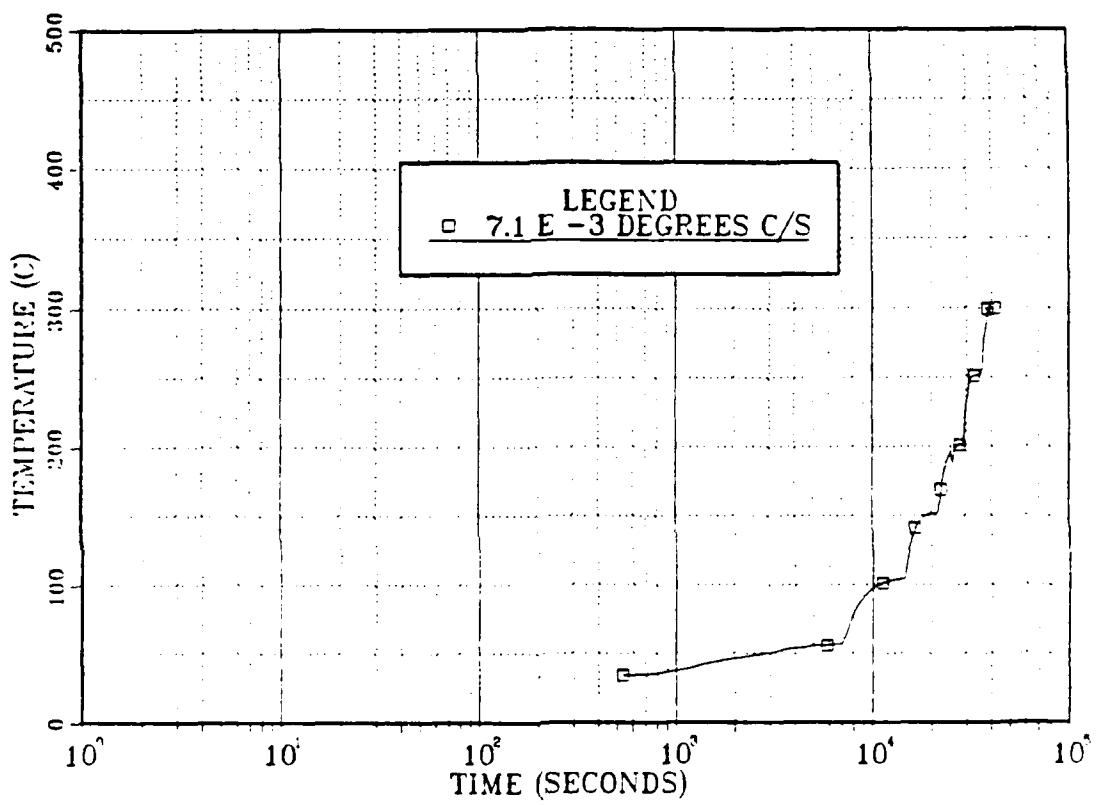


Figure 4.2 Standardized Heating Rate (10^{-3} °C/s)

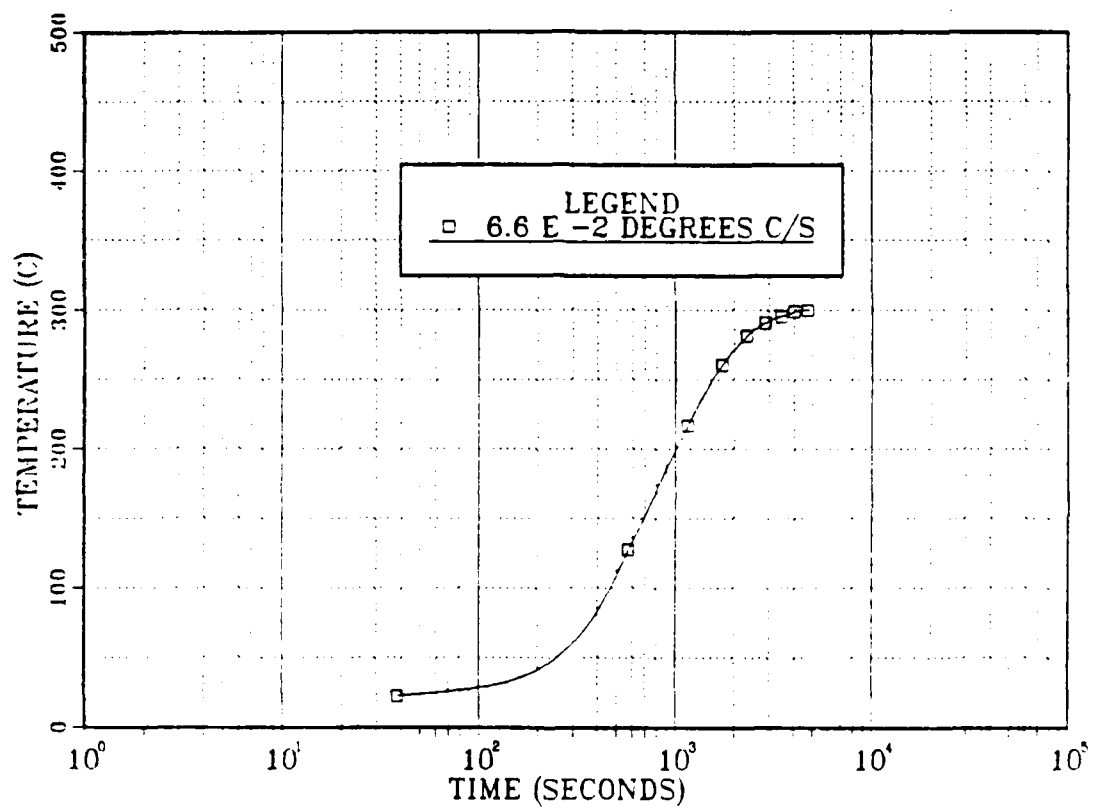


Figure 4.3 Standardized Heating Rate ($10^{-2} \text{ } ^\circ \text{C/s}$)

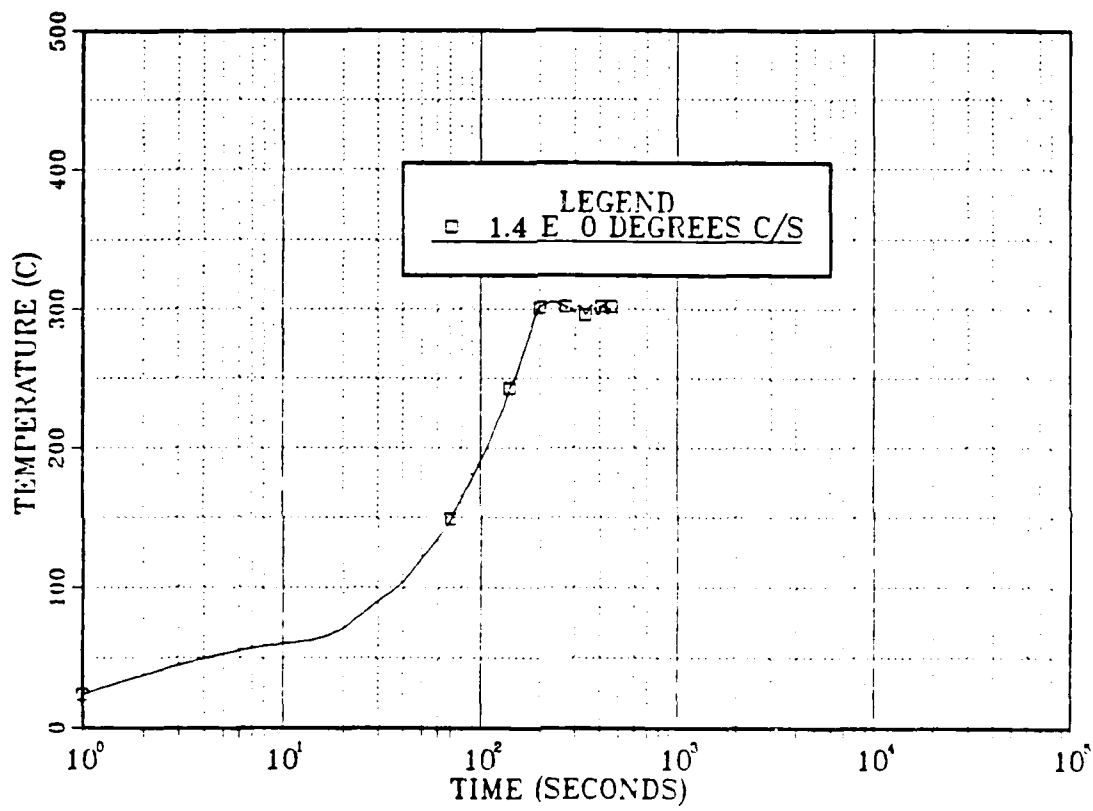


Figure 4.4 Standardized Heating Rate ($10^0 \text{ } ^\circ\text{C/s}$)

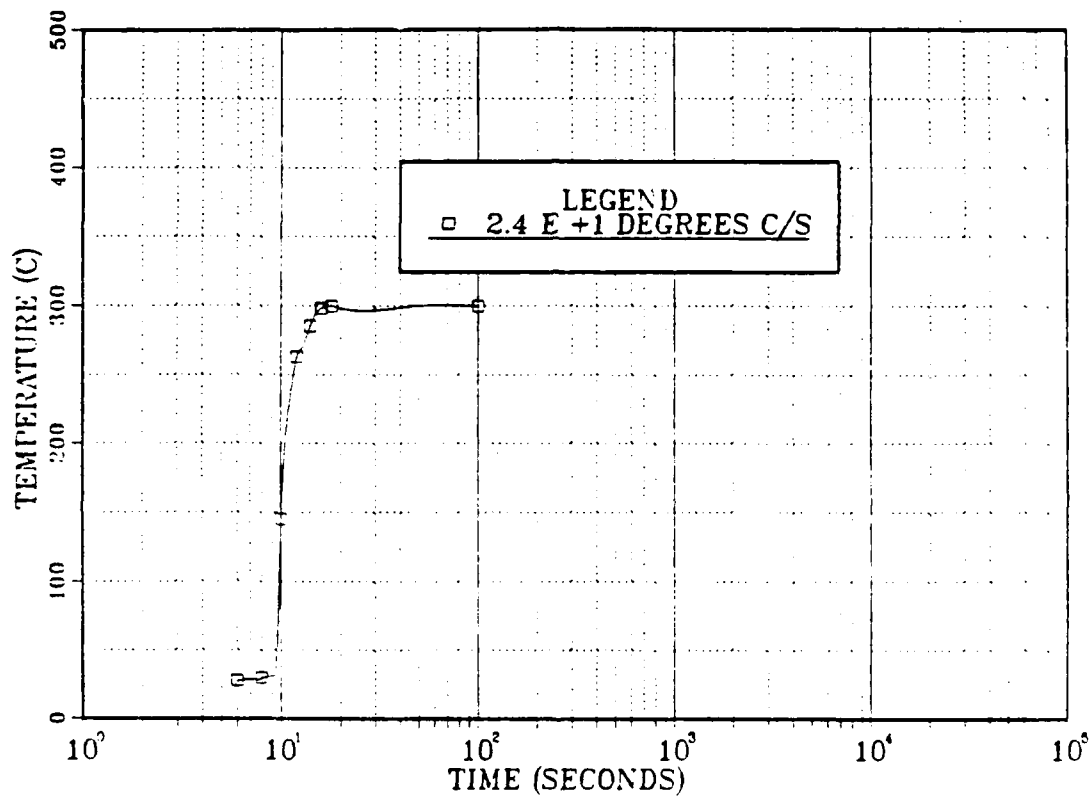


Figure 4.5 Standardized Heating Rate (10^{+1} °C/s)

the furnace after preheating and equilibrating to 300°C. Five runs were conducted and analyzed, with Figure 4.1 representing the fastest rate obtainable using the method described in Section III.B. This curve was obtained with all equipment pre-positioned for use, and with the cross-head elevated to allow immediate insertion of the top sample and wedges assembly into the hot upper grip. A second person assisted by holding hot equipment out of the way and by starting the data collection program at the instant the bottom sample and wedges assembly touched the bottom hot grips. The other four runs had heating rates slower than that of Figure 4.1. How much slower one run is from another depends primarily upon how long it takes the sample assembly to make solid contact with the hot upper and lower grips, and how long it takes before closing the furnace and turning on the power. In Figure 4.1, the deviation from a smooth curve, seen as a "notch" beginning at 100 °C, is due to the delay in seating the upper sample and wedges assembly firmly in the hot upper grip. Once firm contact is made, heat transfer proceeds rapidly. This "notch" can be quite large when insertion is slower, although the curve shape is the same. Using Figure 4.1 data (Appendix B, Table B.1), the standard NPS heating rate is taken as $1.2(10^{-1})$ °C/s.

Figure 4.2 represents the typical heating rate obtained by starting from a room temperature furnace and increasing temperature by 50 °C every two hours until equilibration at

300 °C. Due to the extended nature of this heating rate (12+ hours), only two data collection runs were performed. This data was checked during the actual testing with no significant deviations noted. The final step, from 250-300 °C, was adjusted during the last moments with little effect on the overall shape of the curve. Some precision was lost due to poor furnace controller response, when desired settings were not repeatable. From Figure 4.2 data (Appendix B, Table B.2), this standardized 10^{-3} °C/s heating rate is taken to be 7.1 (10^{-3}) °C/s.

Figure 4.3 is representative of a less commonly used NPS heating rate, where a sample, usually the first in a series of elevated temperature tests, is placed in a room temperature furnace and heated to test temperature (300 °C). The furnace controller settings have been previously calibrated and set, so that only minor equilibration adjustments are required. Six runs were made using this heating rate. This is the most consistent and repeatable heating rate standardized in this study. Consequently, it is ideal for studying the effect of varying equilibration time. From Figure 4.3 data (Appendix B, Table B.3), this heating rate is defined as $6.6(10^{-2})$ °C/s.

Figure 4.4 is fairly representative of over 25 calibration and data collection runs and is the actual heating rate used for sample III/2/A. This heating rate is attained by placing a room temperature tensile sample in a cold radiant furnace, in accordance with the method described in Section III.F. It

is the most inconsistent heating rate used in this study. Overshoot, cycling and time to reach test temperature all varied from run to run. From Figure 4.4 data (Appendix B, Table B.4), the standardized 10^0 °C/s heating rate is defined as $1.4 \cdot 10^0$ °C/s.

Figure 4.5 represents the typical heating rate obtained by placing a tensile sample in a 300 °C nitrate-nitrite salt bath, in accordance with the method described in Section III.G. As previously noted, this is a very rapid and extremely consistent heating rate rarely used in previous research at NPS, with considerable potential hazards associated with it. From Figure 4.5 data (Appendix B, Table B.5) the standardized 10^{+1} °C/s heating rate is $2.4 \cdot 10^{+1}$ °C/s.

B. TENSILE RESPONSE

1. Phase I

This phase of experimentation attempts to repeat a portion of Munro's work. A portion of the results obtained by Munro is shown in Figure 4.6, as a baseline for comparison with Phase I results.

Subsequently, three heating rates to 300 °C were compared in this phase (see Figure 4.7), and it is assumed that the rate 10^{-1} °C/s is reasonably representative of that used by Munro. A marked decrease in superplastic ductility is evident when the heating rate is increased from 10^{-3} °C/s to 10^{+1} °C/s, as shown in Figure 4.8. A comparison between the

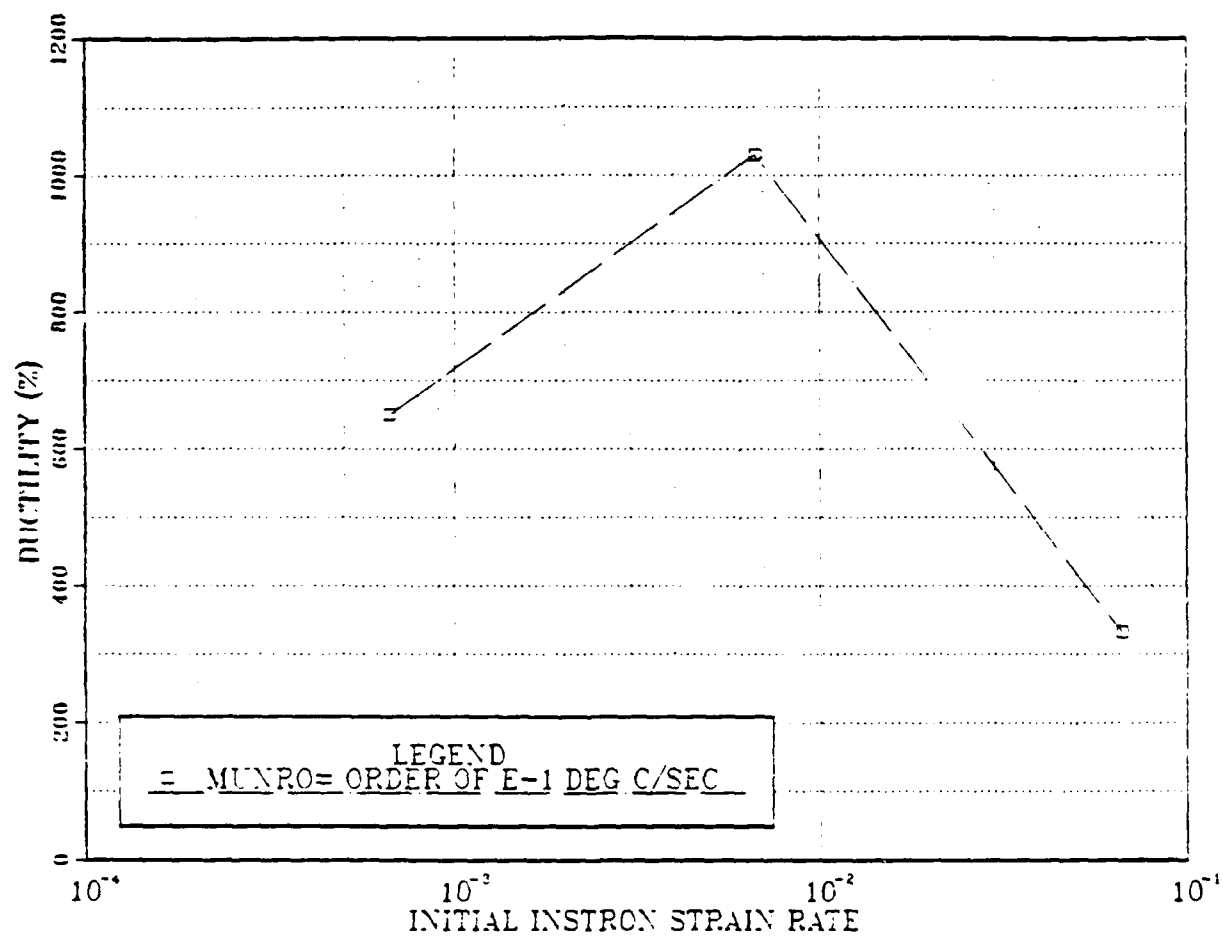


Figure 4.6 Ductility vs Strain Rates at a Nominal 10^{-1} °C/s;
Data Obtained from Munro [Ref. 22:p. 44]

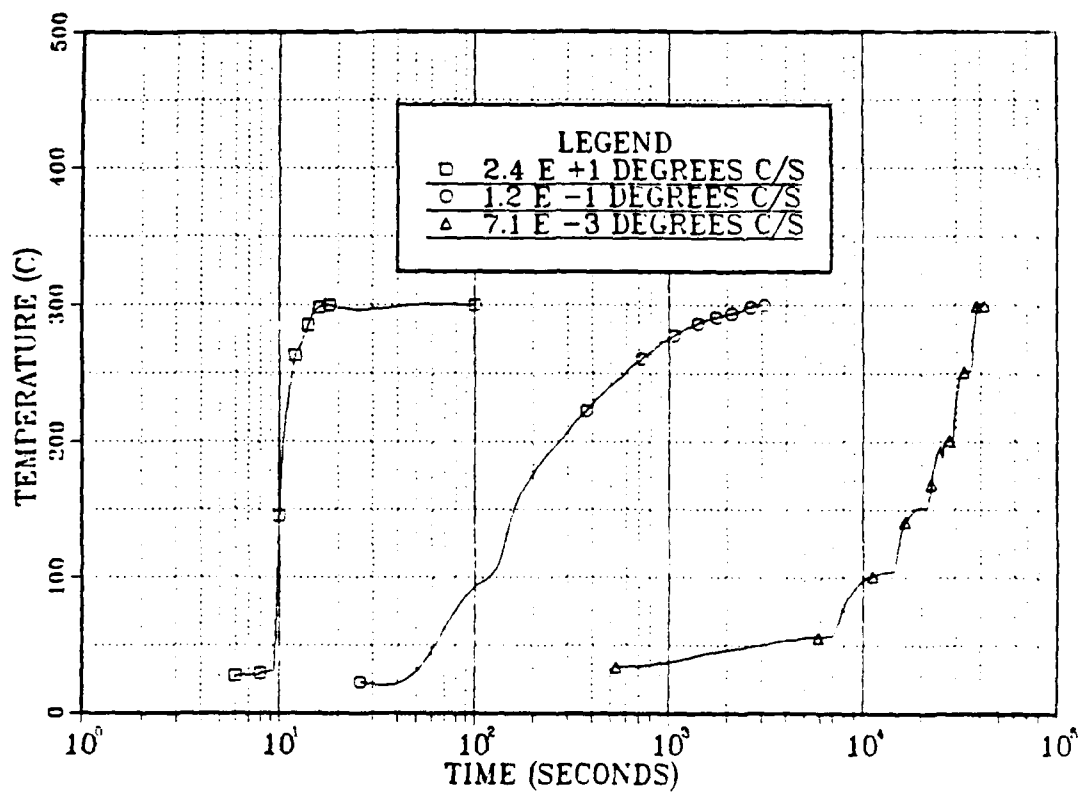


Figure 4.7 Heating Rates Used in Phase I

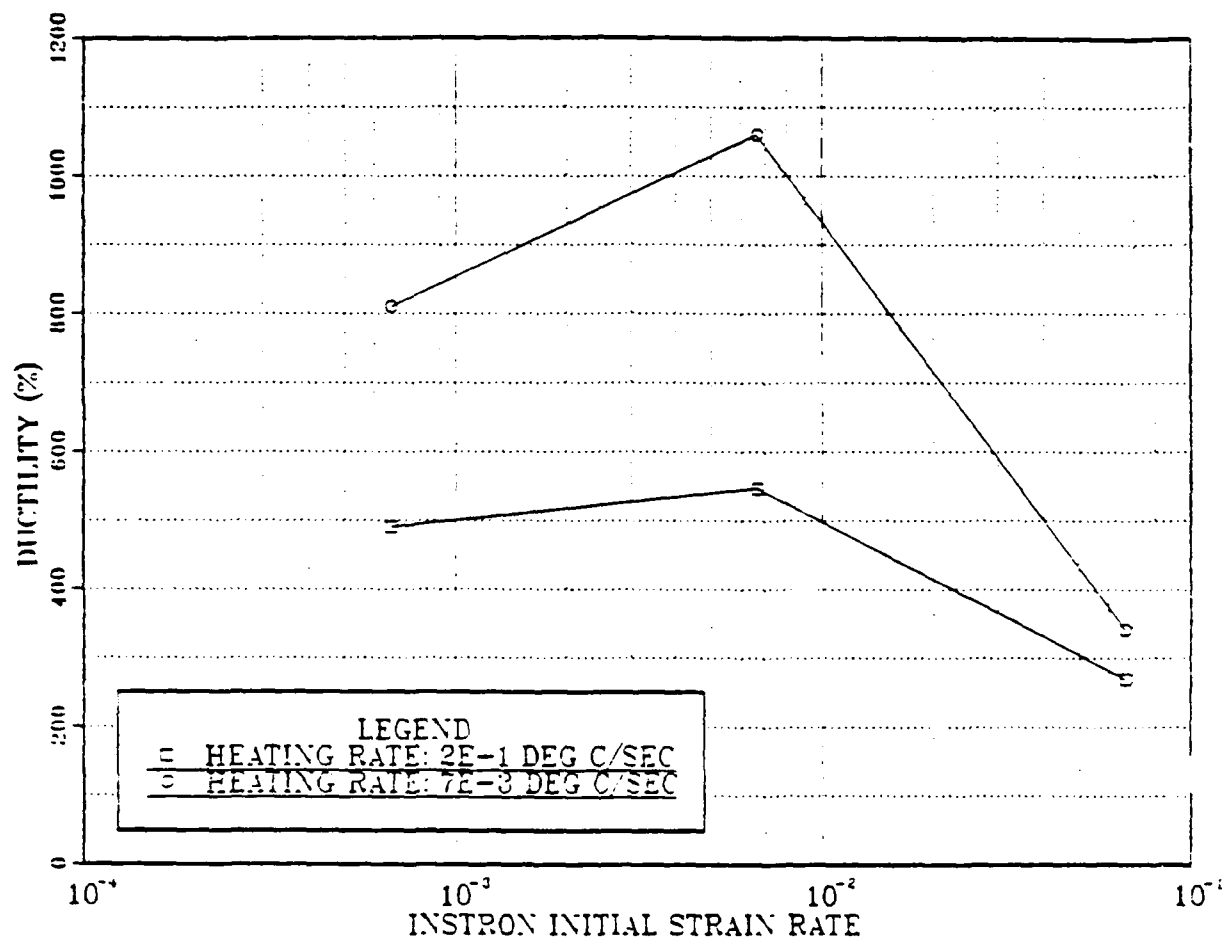


Figure 4.8 Phase I Ductility vs Strain Rate Using Two Heating Rates That Differ by Four Orders of Magnitude. All Samples Prepared by Munro

results Munro reported and these results (see Figure 4.9) confirms that ductility does follow the pattern previously reported by Munro, where superplastic ductility rises and then falls off as the initial strain rate is increased.

In addition, Figure 4.9 reveals another pattern, where ductility decrease is progressive as heating rate is increased for the two extremes of initial strain rate. For the intermediate strain rate, the relationship no longer appears progressive.

The results from this attempt to duplicate Munro's work are not completely consistent with this pattern (see Figure 4.10). Here, the results from the two extremes of initial strain rates are remain consistent with the pattern but the intermediate initial strain rate does not yield a result (I/5/A, 424%) as large as that reported by Munro (1000+%), and also contradicts the pattern seen in Figures 4.8 and 4.9, i.e., slower heating yields better ductility. A second attempt (I/5/B) was made with the last sample remaining and it yielded a slightly better result (454%), which is used in Figure 4.10. However, the two data points (I/5/A, I/5/B) are so close that the net effect is still the same; an almost linear decrease in ductility as initial strain rate is increased, with no peak. No flaw in experimental procedure could be found that could explain why this critical test could not be duplicated, even when done a second time. One possibility is that the time taken to reach equilibration

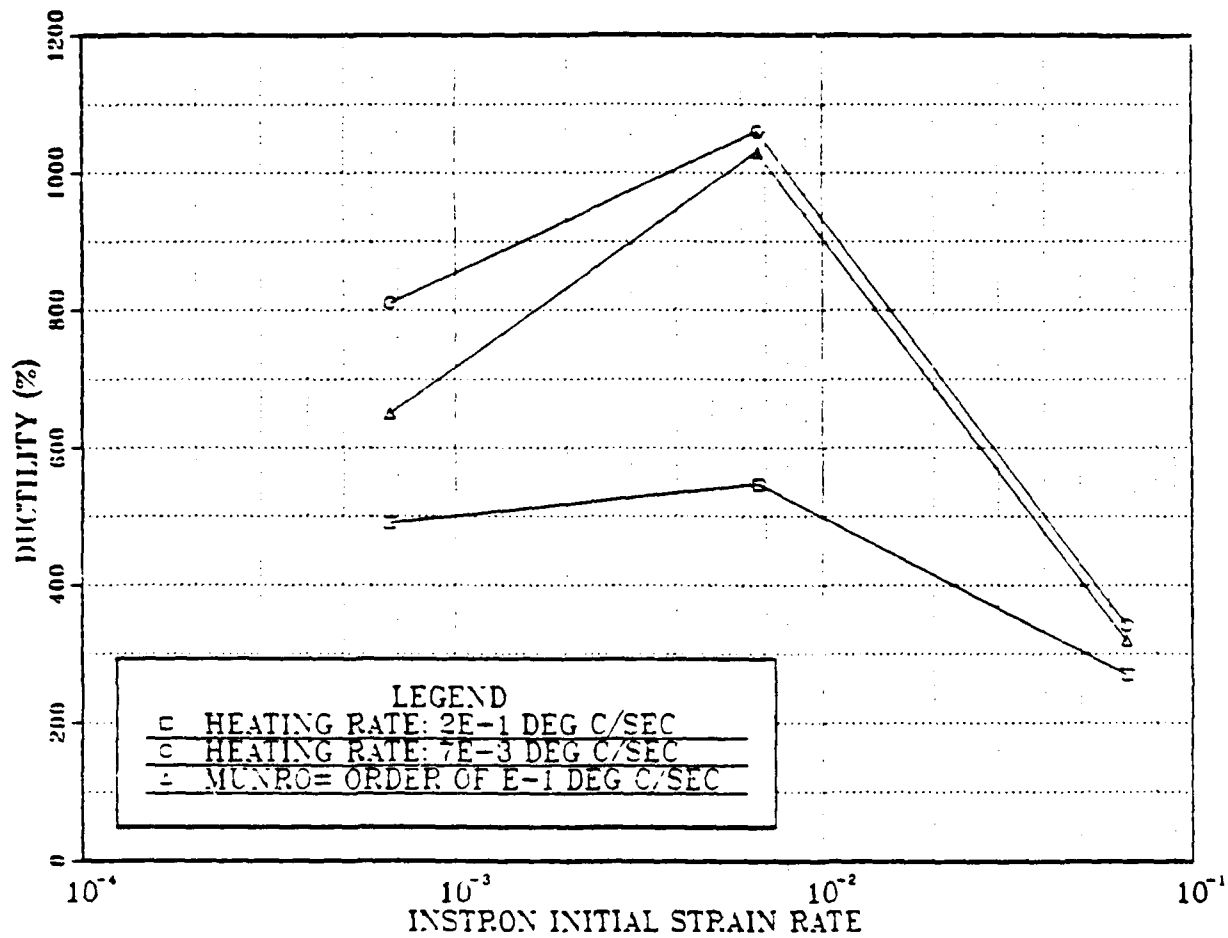


Figure 4.9 Ductility vs Strain Rate Using Three Heating Rates That are Separated by Two Orders of Magnitude. Data Obtained from Munro and Phase I Data. All Samples Prepared by Munro

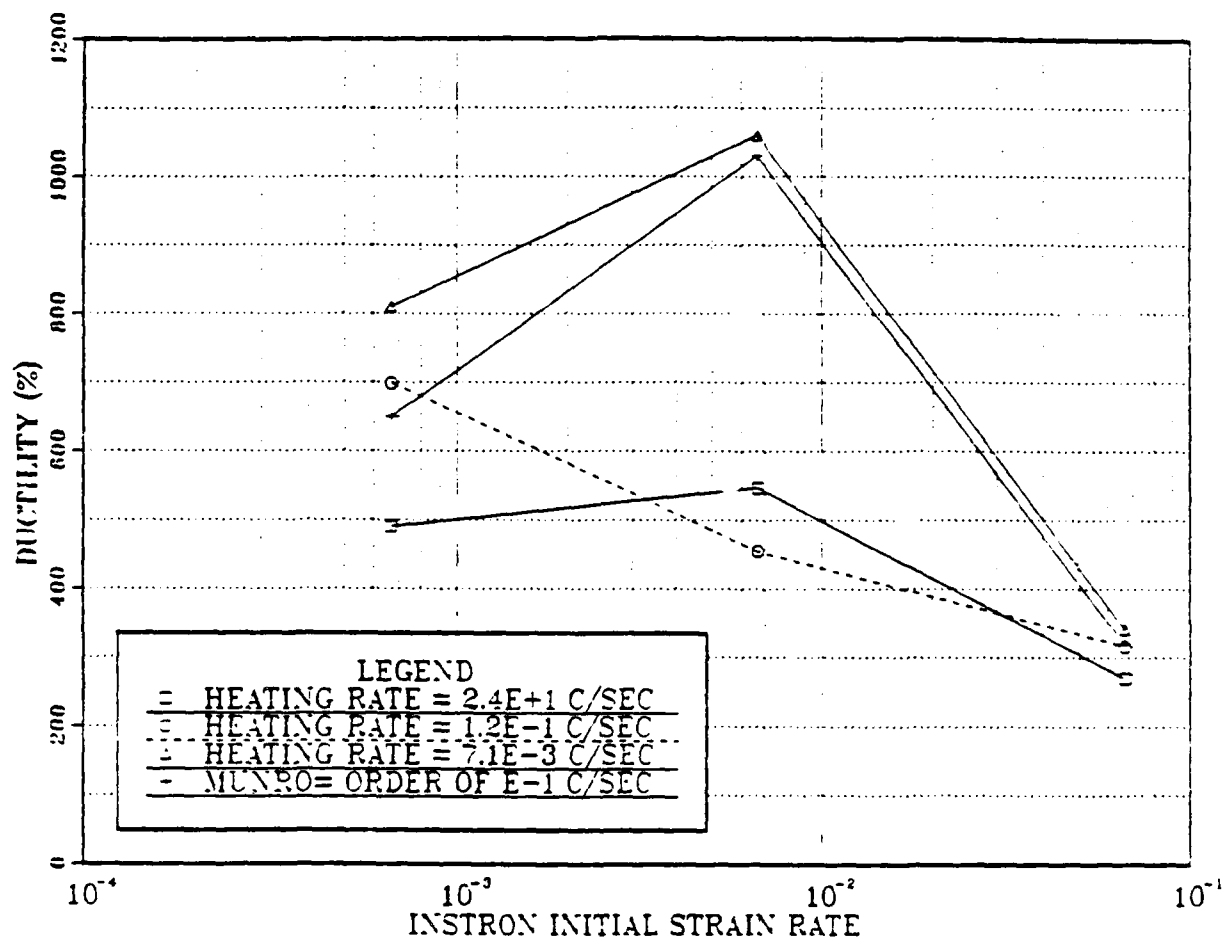


Figure 4.10 Ductility vs Strain Rate Using Three Heating Rates Separated by Two Orders of Magnitude. Data Obtained from Munro and Phase I. All Samples Prepared by Munro

varied from run to run. Sometimes equilibration would occur in ten minutes, and at other times nearly 60 minutes was required, due to a non-linear response of the furnace controllers to settings. Phase I data is found in Appendix B, Table B.6.

2. Phase II

Phase II was designed to repeat part of Phase I with samples prepared from Block 2, in an effort to duplicate the 1,000+% elongation reported by Munro and to gain a better understanding of the indicated inverse relationship between heating rate and ductility. Since equilibration time prior to initiation of straining might have an influence on ductility, the 10^{-2} °C/s heating rate (see Figure 4.4) was added to the three heating rates used in Phase I (see Figure 4.7), since it is very consistent from test to test, and any changes in ductility can be safely correlated with changes in equilibrating times. Three equilibration times were used (see Table 3.3). Since initial strain rates were not varied (only the initial strain rate that yielded peak ductility, $6.67E-3\text{ s}^{-1}$, was used) variations in ductility due to heating rate effects are more apparent.

The data from this phase were ambiguous. Based on results from Phase I, it was expected that the slowest heating rate would give the best ductility, and that faster heating rates would result in decreasing ductility. When the ductility versus heating rate data was plotted, no clear

pattern emerged. However, another pattern was noticed: an inverse relationship was seen between sample gauge thickness and superplastic ductility. The sample's gauge thickness was plotted against ductility (see Figure 4.11). A correlation coefficient for the three slower heating rates was calculated (-0.999) and a linear regression line was generated. Randomness appears to be minimal.

The three samples with varying equilibration times (II/2/A, 45 min.; II/2/B, 10 min.; II/2/C, 20 min.) all showed the same linearity noted above. The three data points plotted on the linear regression line, indicating that equilibration times under 45 minutes will have negligible effect upon superplastic ductility.

The two data points representing the samples using the fastest heating rate (10^{+1} °C/s) clearly indicate that the samples responded in a different manner from the samples experiencing slower heating rates. This suggests that a transition point for ductility in this alloy may occur somewhere between 10^{+1} °C/s and 10^{-1} °C/s. An inverse relation between ductility and thickness was observed, similar to the one seen with the five samples using heating rates slower than 10^{-1} °C/s; but, no other inferences can be drawn with only two data points. Figure 4.11 data is found in Appendix B, Table B.7.

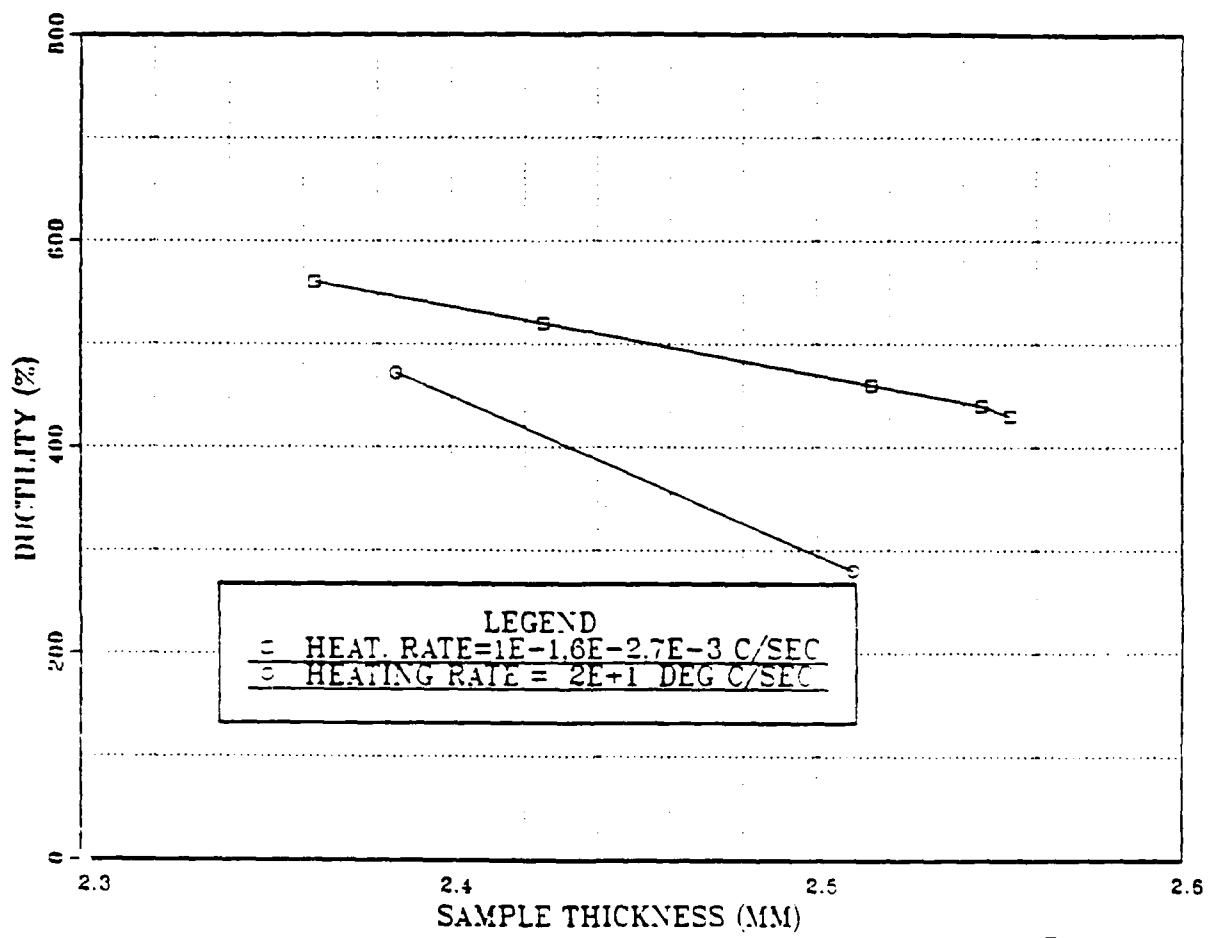


Figure 4.11 Phase II Ductility vs Thickness of Sample Gauge Using Four Different Heating Rates. Strain Rate Used is $6.67E^{-3} s^{-1}$. Samples Fabricated from Block 2 (see Table 3.1)

3. Phase III

This phase of experimentation only involved three samples, which were ranked in order of increasing thickness and increasing heating rate (see Table 3.4). Based on ranking and the patterns noted in Phase II, it was expected that if thickness dominated, then the thinnest sample (III/1/A) would show the most ductility; and, if heating rate dominated then the slowest heating rate (III/3/A) would show the greatest ductility. The three heating rates used in this phase were 10^{-1} °C/s; 10^0 °C/s; and, 10^{+1} °C/s (see Figures 4.1, 4.4 and 4.5).

The results (see Figure 4.12) indicate that, for this limited sample group, heating rate does dominate. That is, the thickest sample with the slowest heating rate (III/3/A) has the greatest ductility, while the fastest heating rate causes the thinnest sample to have the least ductility.

A discontinuity is seen between 10^0 °C/s and 10^{-1} °C/s, indicating that a transition occurs between these two heating rates that affects ductility, which is consistent with the results from Phase II (see Figure 4.11). This is in agreement with Bampton, et al. [Ref. 46], who report that grain refinement of 7xxx aluminum by static DRX requires heating rates greater than 5 °C/s, with longitudinal grain size increasing rapidly for heating rates less than 1 °C/s. Figure 4.12 data is found in Appendix B, Table B.8.

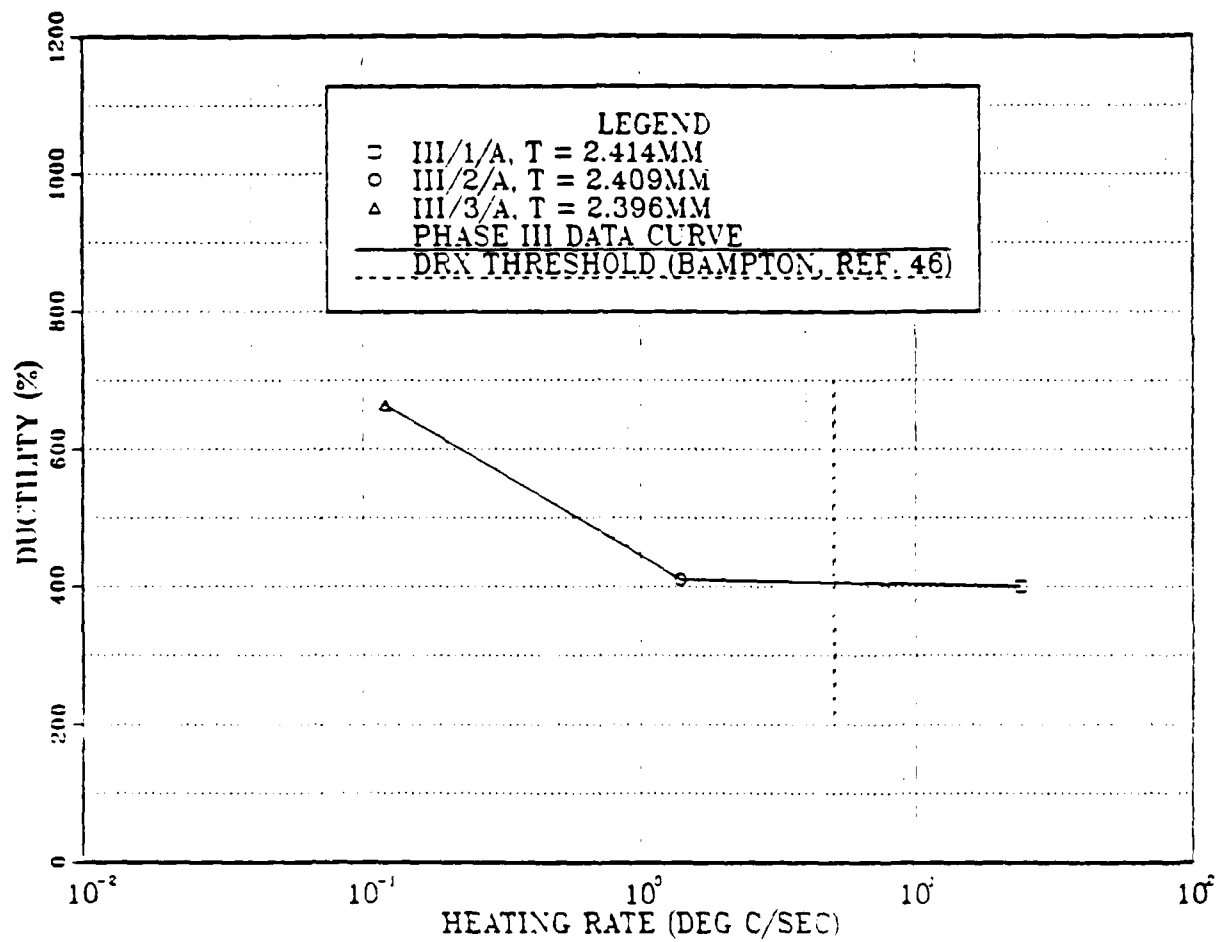


Figure 4.12 Phase III Ductility versus Heating Rates for Al-8%Mg-1%Li-0.2%Zr Alloy, with Sample Gauge Thickness Noted. Strain Rate Used is 6.67×10^{-3} /s. Samples Fabricated from Block 1, Part 1 (see Table 3.1). DRX Threshold for 7xxx Aluminum Indicated as 5 °C/s, from Bampton, et al., who also Report Rapid Grain Growth for Heating Rates Lower than 1 °C/s [Ref. 46]

4. Phase IV

This phase further attempted to explore the relation between sample thickness, heating rate to test temperature and superplastic ductility, while attempting to confirm the existence of a transition with several well documented runs. Since any variations in isothermal TMP conditions were accounted for in the experimental design (see Figure 3.3), ductility was expected to be a function of only thickness and heating rate. Results (see Figures 4.13 and 4.14) did not follow expectations. In some samples, thickness dominated and in others heating rate dominated.

A trend can be seen in the sample row closest to the broken, cut off end (IV/7/A, IV/8/A, IV/9/A), which had the highest average ductility and conformed most to expectations. It was the only row exposed to five surfaces, one of which was a clean surface and not heavily oxidized.

5. Portevin-LeChatelier Effect

In comparing the stress-strain curves generated during tensile testing, it was noted that the curves from Phases II, III and IV all had serrations near the curve peak, while Phase I stress-strain curves did not.

Serrated flow, or the Portevin-LeChatelier effect (PLC), indicates that discontinuous yielding is occurring. This dynamic strain aging behavior is thought to be caused by solute atoms diffusing faster, catching up to, and locking dislocations in place. Loading then increases, due to the

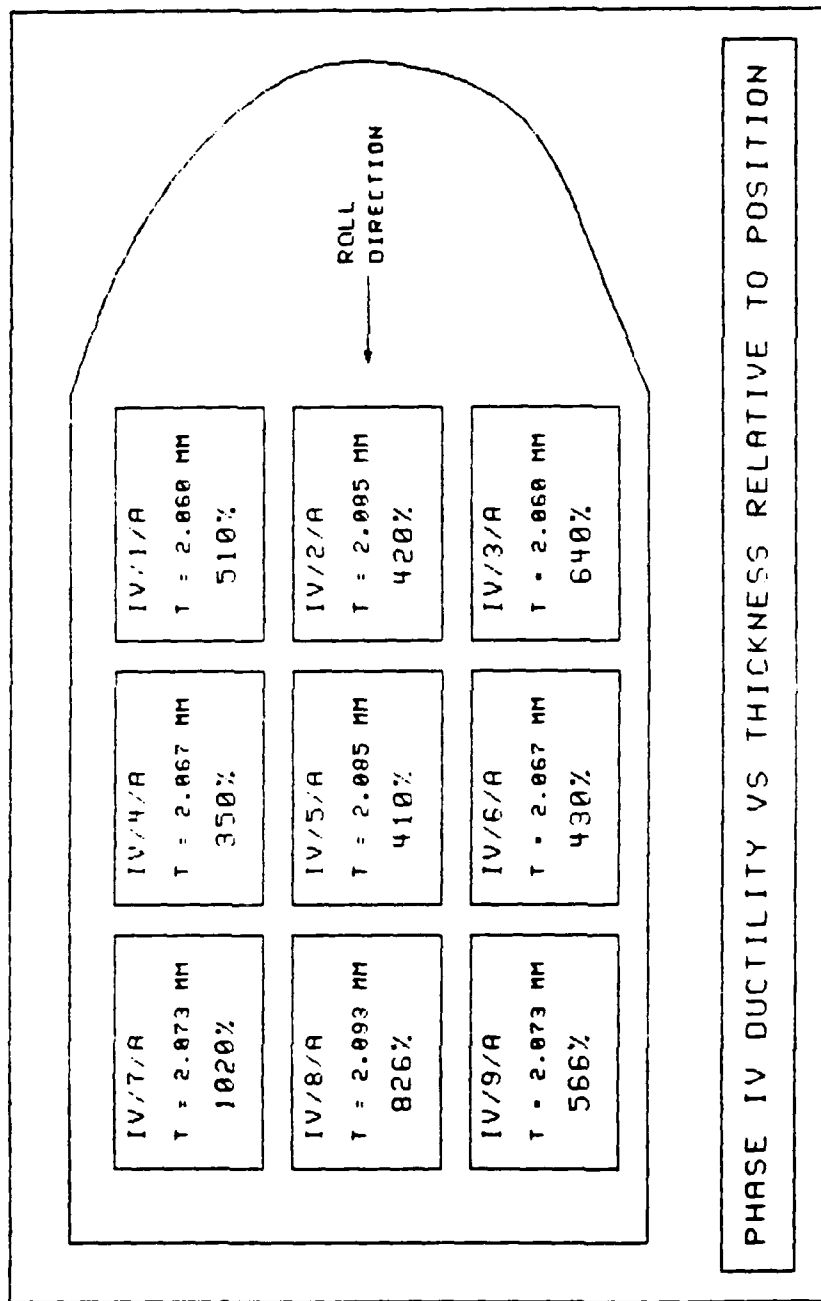


Figure 4.13 Phase IV Ductility as a Function of Thickness of Sample Gauge and Position of Sample, Relative to its Origin in the Rolled Parent Metal. When Comparing within a Row, True Isothermal Conditions Exist. Samples were Fabricated from Block 1, Part 2 (see Table 3.1)

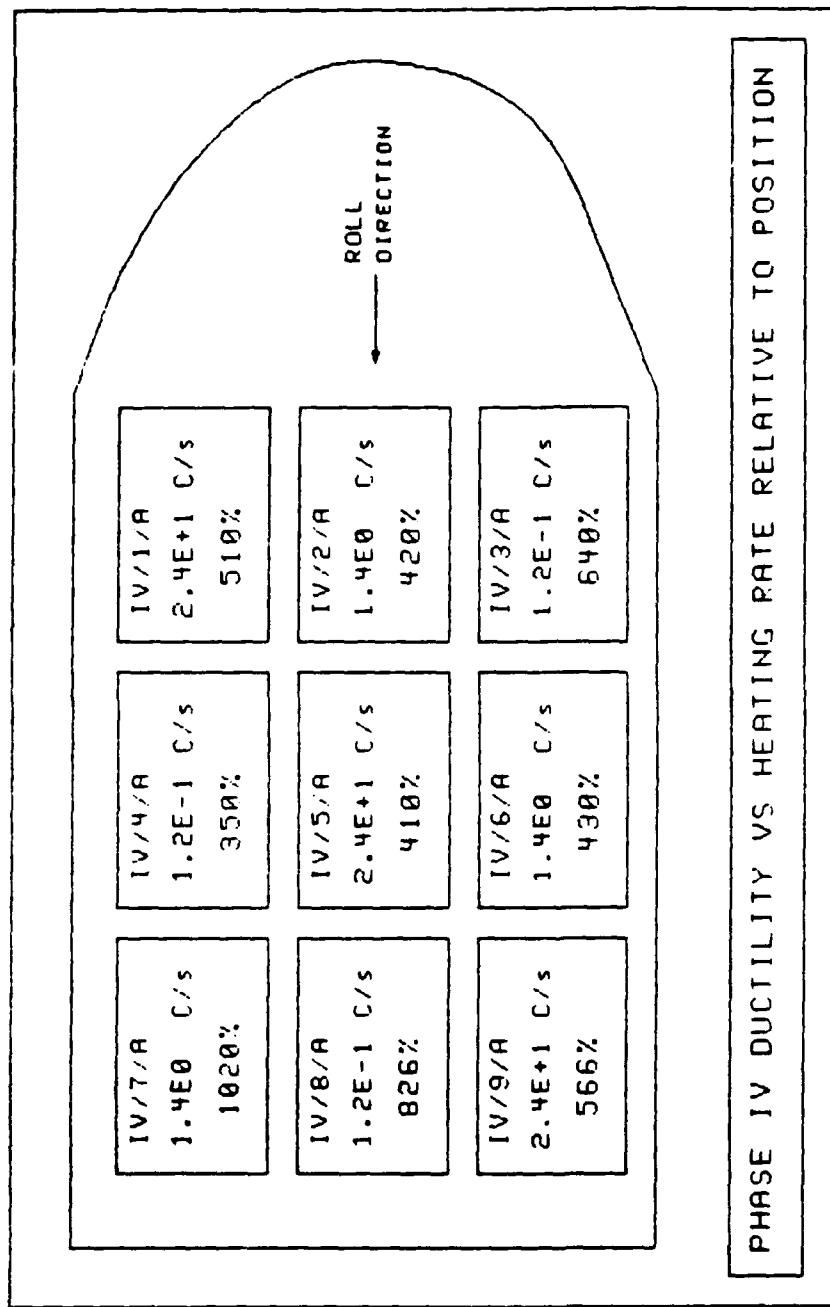


Figure 4.14 Phase IV Ductility as a Function of Heating Rate and Position of Sample, Relative to its Origin in the Rolled Parent Metal. When Comparing within a Row, True Isothermal Conditions Exist. Samples were Fabricated from Block 1, Part 2 (see Table 3.1)

locking, and eventually dislocations are torn away from the solute atoms, causing the load to drop. This cycle repeats itself, causing many serrations to appear in the stress-strain curve [Ref. 39:p. 202].

This phenomenon is usually reported to occur at room temperature when testing aluminum alloys and no reports of this effect at temperatures as high as that of this study were found.

6. Strain Rate Sensitivity Coefficient

The data from Phase I were reduced, using the computer program found in Appendix A, and then was plotted (see Appendix C). Using this data and Equation 3.1, the slopes of the flow stress curves (m -values) were calculated and tabulated in Table C.1 (see Appendix C).

The m -values reach their peak at $6.67E-3\text{ s}^{-1}$ and then drop off for all three heating rates studied, which is in agreement with Munro's data. In addition, a close relationship between peak ductility and maximum m -value was not observed. For the heating rate characteristic of most testing conducted at NPS (see Figure 4.1), ductility increased (from 316-698%) as the m -value decreased (from .36-.31). Munro made a similar observation [Ref. 22:p. 42].

7. Fracture Mode

The fracture mode generally followed the trend noted by Munro [Ref 22:p. 43]. That is, the greater the elongation, the narrower the neck. Some samples (I/3/A, II/1/A, II/3/A,

II/4/B, IV/1/A, IV/7/A) exhibited necking at several points, indicating the existence of strain hardening that prevents further narrowing in one area, while in another area, narrowing occurs due to the existence of a weaker structure.

Fracture surfaces in all samples were flat, with no fracture approaching zero cross-sectional area. Even samples with great elongations (in excess of 800%) had a distinctly flat fracture surface. This observation is also consistent with Munro's [Ref. 22:pp. 45,48]. Ideally, failure during superplastic deformation occurs when unstable plastic flow exists, causing the sample to fail when the neck narrows to a very small cross-sectional area. However, when a flat fracture surface occurs, it indicates that a quasi-brittle condition exists. This condition starts as cracks and decohered interfaces with hard intermetallic phases from the TMP, interlinking and developing into cavities under tensile loading [Ref. 59]. Munro reported that no cavitation was noted in this alloy when he examined sample gauge sections with the transmission electron microscope (TEM) [Ref. 22:pp. 52,70].

V. DISCUSSION

If the microstructures for superplasticity are developed by a discontinuous reaction, then the important feature leading to the fine grain size is a high amount of stored energy produced by cold working, in the presence of a dispersion of 1 micron sized particles, followed by a high rate of heating from ambient to SPF temperature. The particles serve as nucleation sites for DRX. A slower heating rate will facilitate recovery, and strain concentrations will decrease to the extent that recrystallization (DRX) may occur at fewer sites, resulting in a relatively coarser grain structure.

Conversely, continuous reactions seem to require a relatively lower heating rate and more prolonged heating at temperature. It has been proposed that the TMP used in the Al-8%Mg-1%Li-0.2%Zr alloy is one that has a continuous reaction occurring in the reheating between the rolling passes if sufficient reheating time is employed. It is important to realize that in the rolling-reheat cycles during the TMP for this alloy, cooling of the material takes place. When the material is removed from the furnace just prior to rolling, it is at the furnace temperature (300 °C). The material's temperature drops as it is transferred from the furnace to the rolling mill, the more so as the material gets thinner (surface effect). Even though some adiabatic heating may

occur in the rolling mill during the rolling pass, it is certain that the material emerges from the rolling mill at a temperature lower than the furnace. This temperature drop can range from 10 °C, in the early rolling stages, to as much as 30 °C in the later stages [Ref. 60].

In the second to last pass, the material goes back into the furnace and is reheated at some rate from ~270 °C to 300 °C. According to the interpretation of combined reactions (see Section II.D) a continuous reaction will occur upon reheating to 300 °C, since the heating rate is relatively low due to the low temperature gradient involved.

After the last rolling pass, the material is immediately quenched upon emerging from the mill, preserving a high dislocation density. An additional dislocation density is probably generated from quenching a two phase material. The material now has a high dislocation density with a microstructure already refined via CRX during the reheating intervals prior to the final pass.

Subsequently, the material is reheated back to 300 °C. If the heating rate is sufficiently high, the high dislocation density and particles present may initiate a discontinuous reaction (DRX), producing a coarser microstructure than a slower heating rate would.

A. HEATING RATE AND COMBINED REACTIONS

The results of Phases I, II, and III appear to be consistent with the interpretation of the combined reactions model proposed and illustrated in the TTR diagram shown in Figure 2.8. These results indicate that a fast heating rate does initiate DRX, as evidenced by decreased ductility upon subsequent straining. Slower heating rates show an overall increase in ductility, which is consistent with Munro's observation that CRX is favored with the heating rate (10^{-1} °C/s) he used, resulting in the fine grain size required for superplasticity.

A transitional heating rate seems to exist, between 10^{-1} °C/s and 10^{+1} °C/s, as shown in Figures 4.9, 4.11 and 4.12. When samples were heated with the 10^0 °C/s heating rate to further define the transitional heating rate, the results were mixed, as previously discussed. The four key heating rates used in this study are depicted in Figure 5.1.

In Figure 5.2, the TTR diagram in Figure 2.8 has been modified in accordance with the above discussion. The precipitation reaction line has been eliminated since most, if not all, precipitation of β particles has already occurred prior to completion of the last rolling pass. As such, the reaction that occurs in the microstructure of this alloy upon subsequent reheating, prior to straining, is not a combined reaction. Additionally, the discontinuous reaction (DRX) curve is terminated, to reflect the fact that if the material

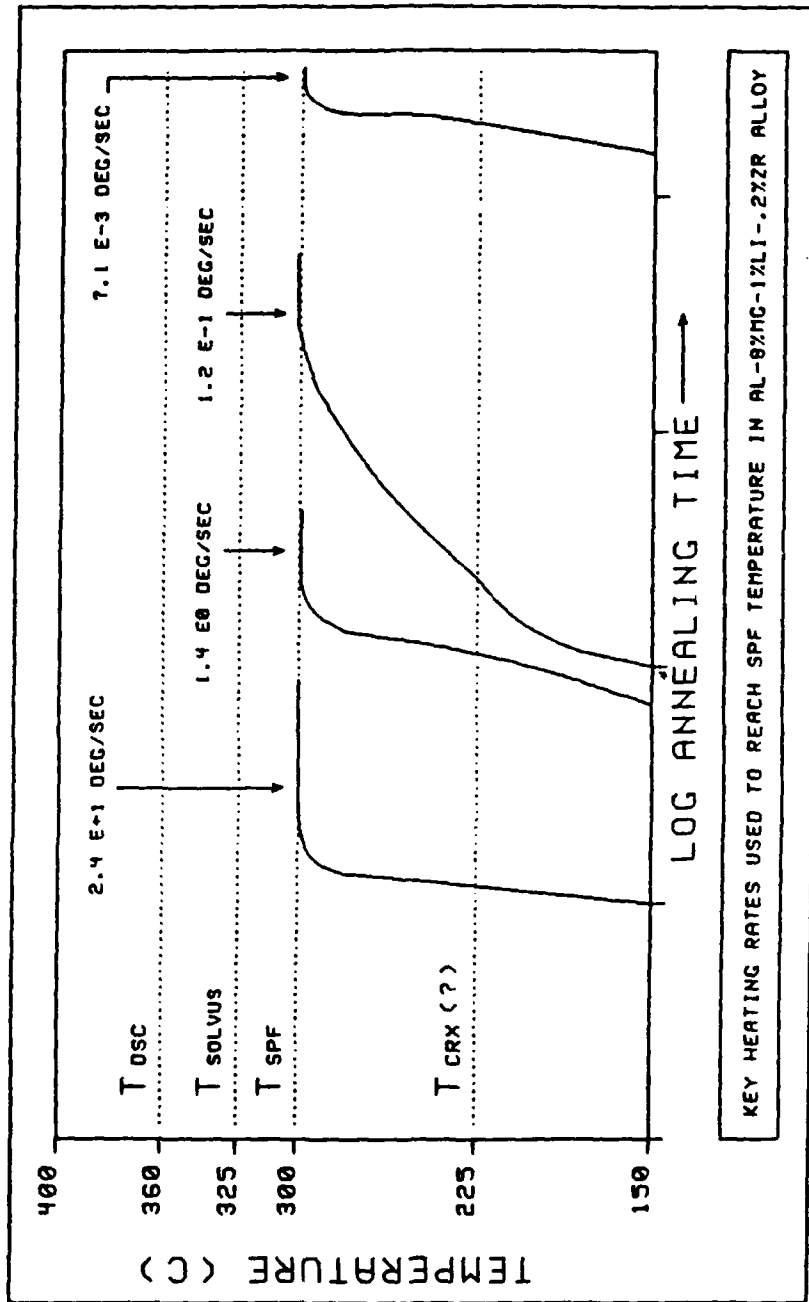


Figure 5.1 Four Key Heating Rates Used in Tensile Testing

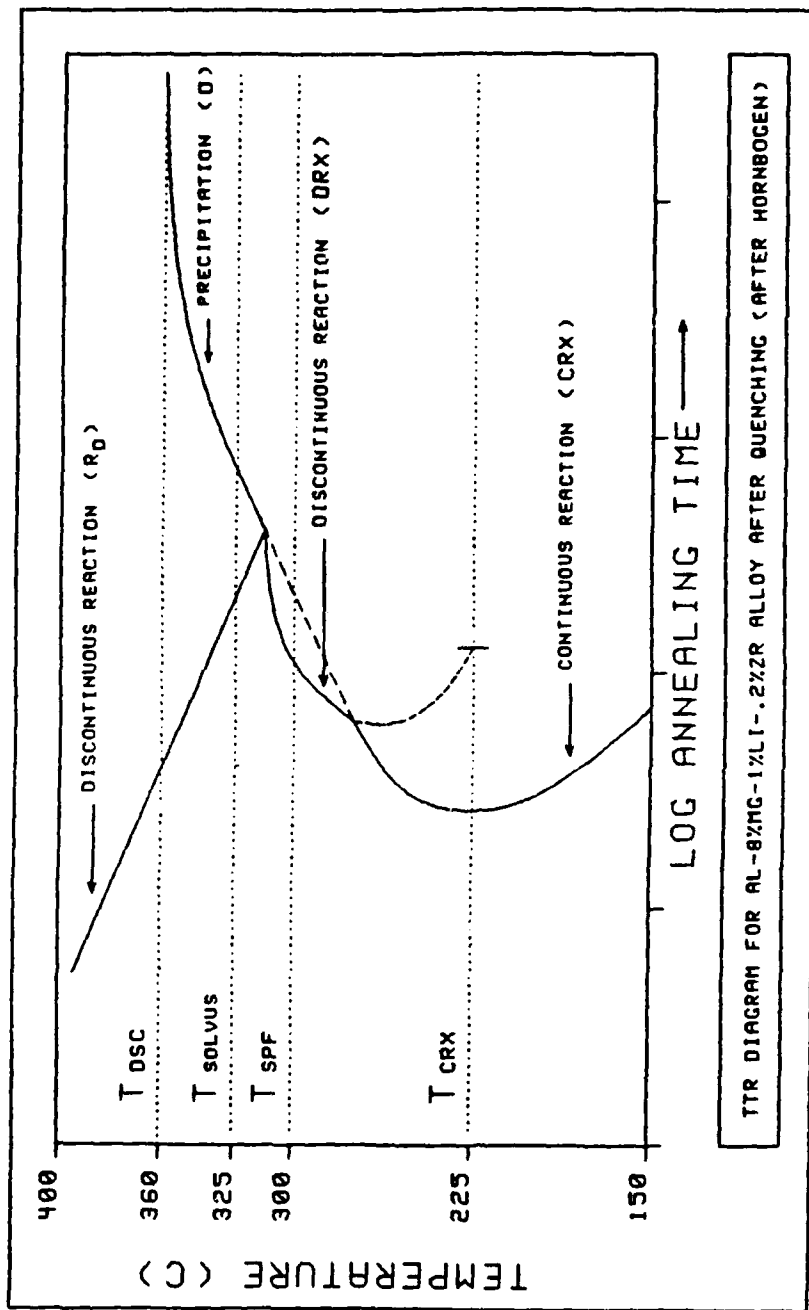


Figure 5.2 Time-Temperature-Reaction Diagram (Schematic)

has undergone a continuous reaction sufficiently, a discontinuous reaction should not be possible.

Superimposing the heating rate curves used in this study (Figure 5.1) upon the TTR diagram (Figure 5.2) combines these concepts into one diagram (Figure 5.3). Figure 5.3 shows that high heating rates characteristic of those attained with a salt bath, result in the material reaching test temperature before the onset of a continuous reaction can occur, with the material passing through a discontinuous reaction upon equilibration.

Conversely, the slower heating rates, such as those attained with the radiant heater or with the NPS test facility used for this research, initially cross the line representing the onset of the continuous reaction first. If the continuous reaction proceeds sufficiently, the stored energy available for a discontinuous reaction is lost, and the slower heating rate will promote the continuous process with no discontinuous reaction occurring while retaining the finer microstructure developed during the warm rolling-and-annealing cycle. The salt bath heating rate was on the order of 10^{+1} °C/s. Bampton [Ref. 46] reported on the processing of 7075 and 7475 alloys and concluded that heating rates of 5 °C/s or greater are required to initiate DRX. A similar conclusion can be made here: that DRX processes are initiated by rates on the order of, but greater than, 1 °C/s and that slower heating rates

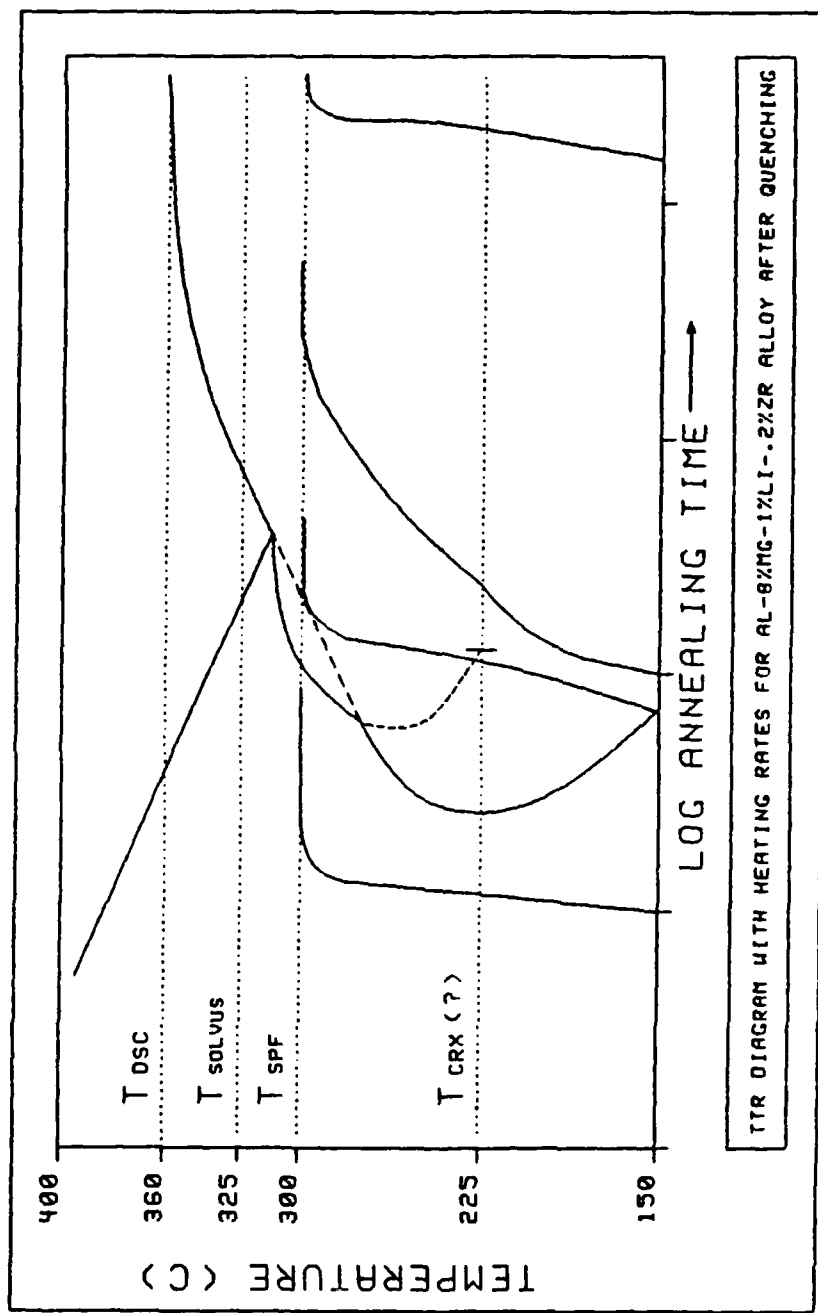


Figure 5.3 T-T-R Diagram with Heating Rate Curves Superimposed.
 T-T-R Curves are Schematic
 TTR DIAGRAM WITH HEATING RATES FOR AL-8%MG-1%LI-2%ZR ALLOY AFTER QUENCHING

provide sufficient time for recovery during heating and thus favor CRX.

B. ADDITIONAL CONSIDERATIONS

As shown in the sequence of Figures 4.6-4.10, the initial phase (Phase I) of this research, with the exception of two data points, is entirely consistent with Figure 5.3 and the concepts proposed. Subsequent attempts to clarify the discrepancy created by these two points, wherein the importance of sample thickness and sample location within the source material was considered, were inconclusive. The data does suggest that some other influences are present, such as sample thickness (total rolling strain) and specifics of rolling procedures. However, the apparent scatter in the data makes it difficult to interpret. Clearly, in terms of the model proposed, there may be additional influences that may not have been accounted for. The data do, however, not directly contradict the initial conclusions of this study.

VI. CONCLUSIONS

1. Heating rate to test temperature has a significant effect upon superplastic response, as measured by ductility.
2. High heating rates on the order of, but greater than, 10°C/s cause a decrease in superplastic ductility in the Al-8%Mg-1%Li-0.2%Zr alloy.
3. Heating rates slower than 1°C/s cause superplastic ductility to be enhanced, with elongations in excess of 1000%, at a relatively low temperature and high strain rate.
4. The enhancement of ductility with slower heating rates is attributed to grain refinement by continuous recrystallization (CRX). It is proposed that the high heating rate's adverse effect upon ductility is due to discontinuous recrystallization (DRX), causing a coarser microstructure to evolve.
5. A model to explain the heating rate effects must consider competition between CRX and DRX reactions in a refined structure with high dislocation density initially present.

VII. RECOMMENDATIONS

1. Process sufficient material to allow a broad range of heating rates and test conditions to be evaluated on material of better defined initial processing history.
2. Conduct microstructural analysis on material used in this study, to determine the effect of heating rate on grain structure.
3. Extend this study by using a rolling mill that allows better control of rolling variables, so as help to clarify the discrepancies and ambiguities noted in this study.
4. A similar study should be conducted, using different aluminum alloys, to evaluate the applicability of the proposed combined reactions-TTR diagram concept.

APPENDIX A

COMPUTER PROGRAM FOR DATA REDUCTION

```

00001 rem: *****
00002 rem: *****
00004 rem: *****
00005 rem: *****
00006 rem: *****
00007 rem: *****
00008 rem: *****
00009 rem: *****
00010 rem: *****
00012 rem: *****
00013 rem: *****
00014 rem: *****
00015 rem: *****
00016 rem: *****
00017 rem: *****
00018 rem: *****
00019 rem: *****
00022 rem: *****
00023 rem: *****
00024 rem: *****
00025 rem: *****
00026 rem: *****
00027 rem: *****
00028 rem: *****
00030 rem: *****
00033 rem: *****
00034 rem: *****
00035 rem: *****
00038 rem: *****
00039 rem: *****
01100 Print
01110 Print '
01120 Print
01130 Print tab(0);'X(in)' ;tab(08);'Y(lbf)' ;tab(16);'Seng(psi)' ;
01000 Read A, N, Xl, ll
01010 For I=1 to N
01020 Read X, Y
01030 S = Y/A
01040 C = (10*Xl)/(X1)
01050 E = (XXC)/(5)
01060 S1= S*(1+E)/1000
01070 E1= log(1+E)
01080 Print tab(0);X ;tab(08);Y ;tab(16);S ;tab(32);E ;tab(43);S1 ;tab(57);E1;
01090 Next I
01100 Print
01110 Print '
01120 Print
01130 Print tab(0);'X(in)' ;tab(08);'Y(lbf)' ;tab(16);'Seng(psi)' ;
01140 Print tab(32);'Eeng("")' ;tab(43);'Strue(psi)' ;tab(57);'Etrue("")';
01145 Print tab(45);'(x 1000)';
01150 Print
01160 Print '
02100 Data .014415, 18, 13.09, 1.02
02110 Data 0 ,60
02111 Data .1 ,96.6
02430 END

```

APPENDIX B
HEATING RATE CURVE DATA

TABLE B.1

$10^{-1} \text{ }^{\circ}\text{C/s}$ HEATING RATE DATA

26	23	960	274	1947	292.9
53	35	987	275	1973	293.1
80	77	1013	276	2000	293.3
107	96	1040	277	2027	293.5
133	112	1067	278	2053	293.7
160	152	1093	279	2080	293.8
187	170	1120	280	2107	293.9
213	183	1147	280.5	2133	294.1
240	192	1173	281.2	2160	294.2
267	199	1200	282	2187	294.4
293	206	1227	282.7	2213	294.6
320	213	1253	283.3	2240	294.6
347	218	1280	284	2267	294.8
373	223	1307	284.5	2293	294.8
400	228	1333	285.1	2320	295
427	232	1360	285.7	2347	295.2
453	235	1387	286.1	2373	295.9
480	239	1413	286.7	2400	296.8
506	242	1440	287.1	2480	298
533	245	1467	287.6	2640	298.5
560	247	1493	288.1	2720	298.8
587	250	1520	288.4	2811	300
613	253	1547	288.8	3000	300
640	255	1573	289.2	3100	300
667	257	1600	289.4		
693	259	1627	289.9	X:SEC	Y:DEGREES
720	261	1653	290.2		
747	263	1680	290.4		
773	264	1707	290.8		
800	266	1733	291		
827	267	1760	291.3	N = 96 POINTS	
853	269	1787	291.6		
880	270	1813	291.7		
907	272	1840	292.1		
933	273	1867	292.2		
		1893	292.4		
		1920	292.7		

TABLE B.2
 10^{-3} °C/s HEATING RATE DATA

533	34	24533	194
1066	38	25066	197
1600	44	25600	188
2133	47	26133	199.7
2666	49	26666	200.6
3200	51	27200	201.6
3733	53	27733	201.1
4266	54	28266	201.4
4800	55	28800	201.1
5333	56	29333	217
5866	55.9	29866	230
6400	56.5	30400	237
6933	56.7	30933	245
7466	68	31466	249.9
8000	80	32000	250
8533	87	32533	250.8
9066	92	33066	251.4
9600	95.6	33600	251.6
10133	98.2	34133	251.9
10666	100	34666	251.9
11200	101.3	35200	251.8
11733	102.3	35733	251.9
12266	102.9	36266	261.2
12800	103.4	36800	277.9
13333	103.8	37333	285.7
13866	104	37866	291.3
14400	104.2	38400	299.4
14933	118.9	38933	299.9
15466	129.3		
16000	136.4	39466	300
16533	141.2	40000	300
17600	146.9	42000	300
18133	148.6		
18666	149.8		
19200	150.6		
19733	151.		
20266	151.2		
20800	151.1		
21333	151.4		
21866	157.1		
22400	168.9		
22933	179		
23466	186		
24000	191		

X:SEC Y:DEG C

N = 75 POINTS

'SLOW #1'
LINEARIZED HEATING RATE

7E-3 DEG C/SEC

TABLE B.3
 $10^{-2} \text{ }^{\circ}\text{C/s}$ HEATING RATE DATA

38.4	22.5
96	28
192	40
288	58
384	79.7
480	104
576	128
672	147
768	165
864	181
960	194
1056	206
1152	217
1248	227
1344	235
1440	243
1536	250
1632	256
1728	261
1824	265
1920	270
2016	273
2112	276
2208	279
2304	282
2400	284
2496	286
2592	287
2688	289
2784	290
2880	291
2976	292
3072	293
3168	294
3264	294.4
3360	295
3456	295.6
3552	296.1
3648	296.4
3744	296.8
3840	297.3
3936	298.2
4032	299.2
4224	299.9
4500	300
4700	300

X:SEC Y:DEG C

N = 46 POINTS

TABLE B.4
 $10^0 \text{ } ^\circ\text{C/s}$ HEATING RATE DATA FOR III/2/A

0	24
10	60
20	71
30	90
40	104
50	121
60	135
70	149
80	164
90	178
100	191
110	204
120	218
130	229
140	243
150	252
160	264
170	275
180	286
190	296
196	300
200	301
210	303
220	304
230	305
240	305
250	304
260	303
270	302
280	301
290	299
300	298
310	302
320	303
330	300
340	296
350	298
360	302
370	303
380	300
390	296
400	298
410	302
420	303
430	300
440	296
450	298
460	302

X:SEC Y:DEGREES C

RADIANT HEATER, SHEET METAL

48 DATA POINTS

TABLE B.5
 10^{+1} °C/S HEATING RATE DATA

6	27.85
6.67	27.88
7.34	28.27
8	29.41
8.67	30.20
9.34	31.11
10	145.24
10.67	213.13
11.34	242.99
12	263.4
12.67	269.33
13.34	276.86
14	285.6
14.67	292.68
15.34	296.59
16	298.33
16.67	299.02
17.34	300.34
18	300
50	300
100	300

X:SEC Y:DEGREES C

SALT 4

21 DATA POINTS

TABLE B.6
PHASE I MECHANICAL PROPERTIES DATA

1A	270	2.125	2.4E1	6.7E-2	-.754
2A	546	2.125	2.4E1	6.7E-3	-.754
3A	490	1.930	2.4E1	6.7E-4	-.658
4A	316	2.177	1.2E-1	6.7E-2	-.778
5A	424	2.230	1.2E-1	6.7E-3	-.802
5B	454	1.930	1.2E-1	6.7E-3	-.658
6A	698	2.122	1.2E-1	6.7E-4	-.752
7A	342	2.175	7.1E-3	6.7E-2	-.777
8A	310	1.923	7.1E-3	6.7E-3	-.685
8B	1060	2.173	7.1E-3	6.7E-3	-.776
9A	810	2.720	7.1E-3	6.7E-4	-.821

SAMPLE	%ELONG	T(MM)	TEMP. RATE	INSTRON INITIAL TESTING STRAIN	LN (1/T0)
--------	--------	-------	---------------	---	-----------

TABLE B.7
PHASE II MECHANICAL PROPERTIES DATA

1A	560	2.363	1.2E-1	2.374	-.860
2A	430	2.553	6.6E-2	2.296	-.937
2B	440	2.545	6.6E-2	2.300	-.934
2C	520	2.425	6.6E-2	2.348	-.886
3A	460	2.515	7.1E-3	2.311	-.922
4A	280	2.510	2.4E1	2.313	-.920
4B	472	2.385	2.4E1	2.365	-.869
<hr/>					
SAMPLE	%ELONG.	T(MM)	TEMP. RATE	TRUE SAMPLE STRAIN	LN (1/T0)
<hr/>					

TABLE B.8
PHASE III MECHANICAL PROPERTIES DATA

1A	400	2.275	2.4E1	2.414	-.822
2A	410	2.285	1.4E0	2.409	-.826
3A	664	2.315	1.2E-1	2.396	-.839

SAMPLE	%ELONG.	T(MM)	TEMP. RATE	TRUE SAMPLE STRAIN	LN (1/T0)
--------	---------	-------	---------------	--------------------------	-----------

APPENDIX C
PHASE I TRUE STRESS-STRAIN DATA

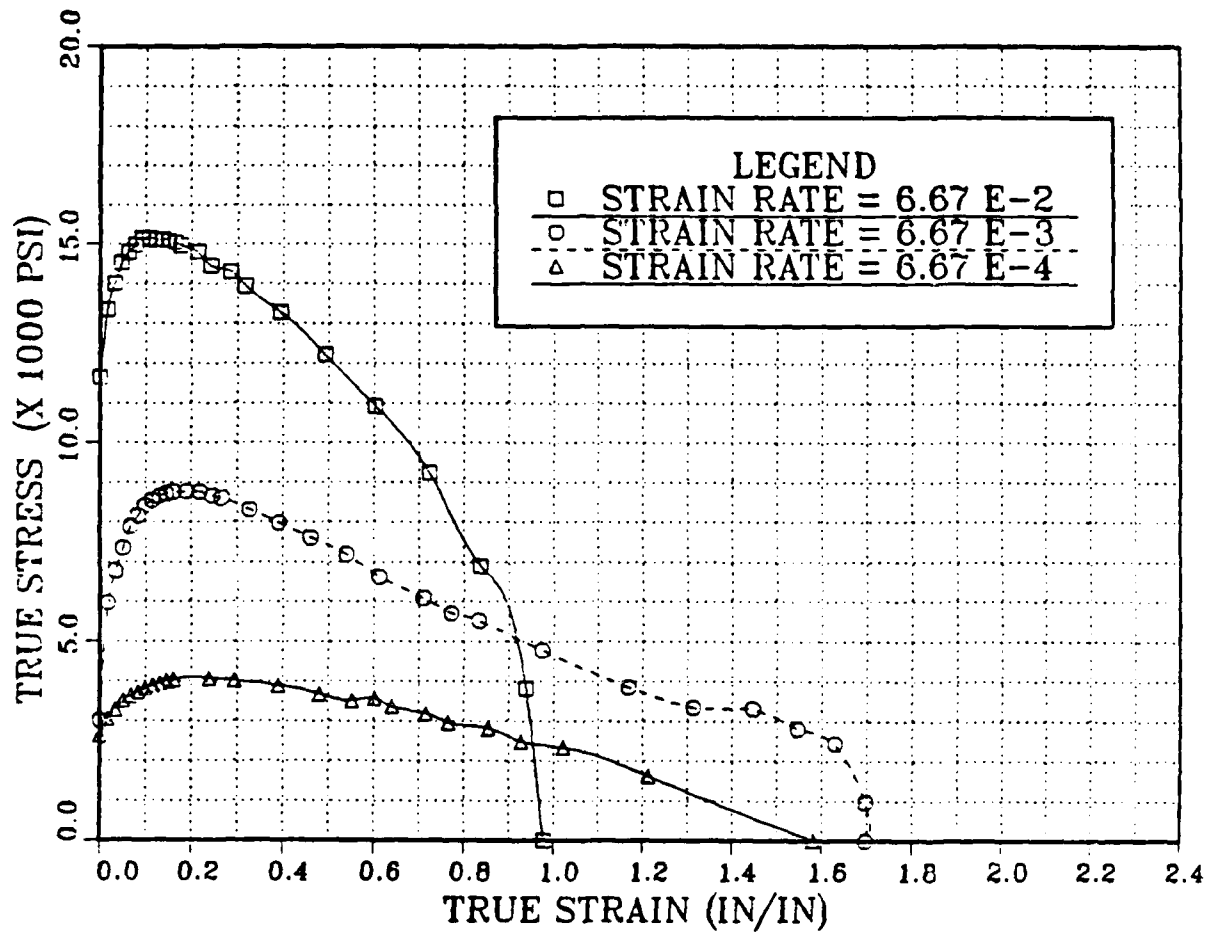


Figure C.1 Phase I True Stress vs True Strain at a Heating Rate of $2.4 (10^{-1}) \text{ } ^\circ\text{C/s}$

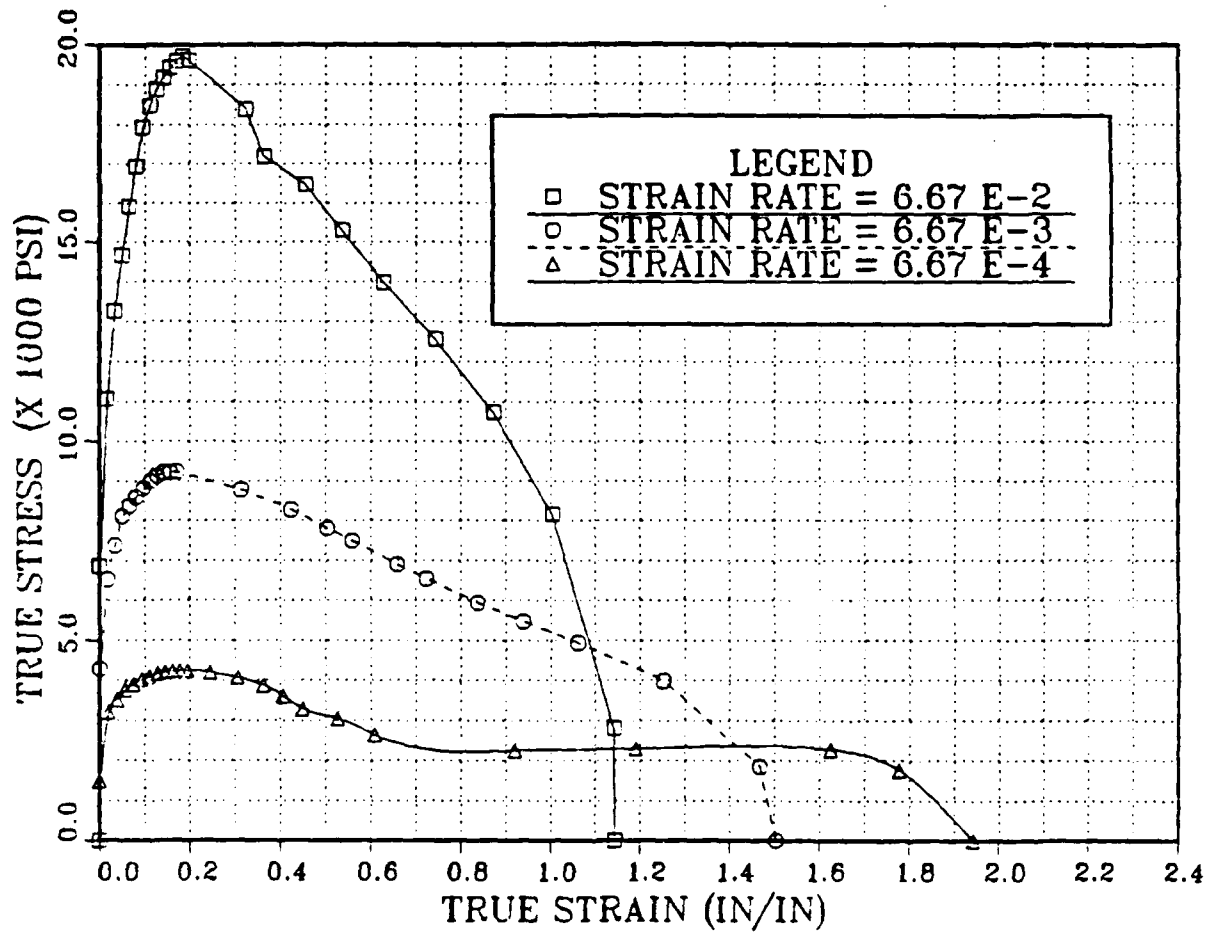


Figure C.2 Phase I True Stress vs True Strain at a Heating Rate of $1.2 (10^{-1})^{\circ}\text{C/s}$

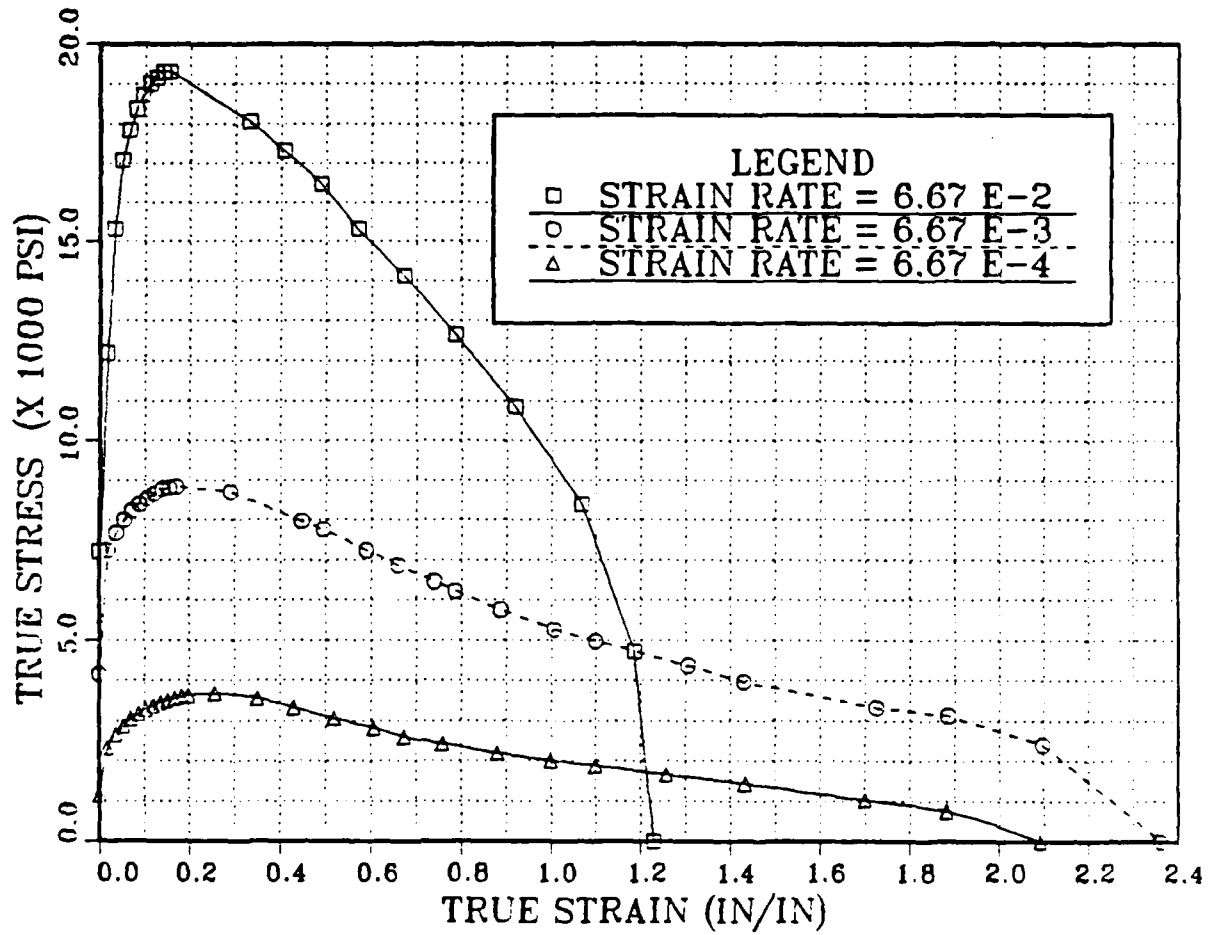


Figure C.3 Phase I True Stress vs True Strain at a Heating Rate of 7.1 (10^{-3}) $^{\circ}\text{C}/\text{s}$

TABLE C.1
FLOW STRESS DATA TAKEN AT 0.1 TRUE STRAIN

PHASE I			
	Strain Rate (kpsi)		
Heating Rate	6.67E-4	6.67E-3	6.67E-2
2.4 (10^{-4}) °C/s	3.8	8.3	15.2
(m-value)	(.34)	(.26)	
1.2 (10^{-4}) °C/s	3.9	8.9	18.3
(m-value)	(.36)	(.31)	
7.1 (10^{-3}) °C/s	3.3	8.5	18.8
(m-value)	(.41)	(.34)	
Munro's data [Ref. 22:p. 44]	3.3	8.5	18.8
(m-value)	(.4)	(.3)	

TABLE C.2
REDUCED DATA FOR SAMPLE I/1/A

0	195	11654.315085	0	11.654315	0
.1	220	13148.458044	.0160542	13.359545	.0159267
.2	227	13566.818073	.0321083	14.002426	.0316036
.3	232	13865.646665	.0481625	14.533451	.0470386
.4	232.5	13895.529524	.0642166	14.787854	.062239
.5	232	13865.646665	.0802708	14.978653	.0772117
.6	231	13805.880947	.096325	15.135732	.0919636
.7	228	13626.583792	.112379	15.157927	.106501
.8	224	13387.520918	.128433	15.106924	.12083
.9	221	13208.223763	.144487	15.116646	.134957
1	217.5	12999.043749	.160542	15.085931	.148887
1.1	214	12789.863734	.176596	15.048499	.162625
1.2	210	12550.800861	.19265	14.968711	.176178
1.48	200	11953.143677	.237602	14.793229	.213175
1.7	190	11355.486493	.272921	14.454634	.241314
2.05	180	10757.829309	.32911	14.298341	.28451
2.32	170	10160.172125	.372456	13.944394	.316602
3	150	8964.257758	.481625	13.282555	.393139
3.96	125	7470.714798	.635745	12.220182	.492098
5.15	100	5976.571838	.826789	10.917937	.60256
6.61	75	4482.428879	1.06118	9.239092	.723279
8.16	50	2988.285919	1.310019	6.902998	.837256
9.7	25	1494.14296	1.557253	3.820902	.938934
10.34	0	0	1.66	0	.978326

X(in)	Y(lbf)	Seng(psi)	Eeng("/*")	Strue(psi) (x 1000)	Etrue("/*")
-------	--------	-----------	------------	------------------------	-------------

TABLE C.3
REDUCED DATA FOR SAMPLE I/2/A

0	50	2997.062878	0	2.997063	0
.1	98	5874.243242	.0173744	5.976304	.0172252
.2	109.3	6551.579452	.0347487	6.779239	.0341586
.3	116.5	6983.156507	.0521231	7.34714	.0508101
.4	123	7372.774681	.0694975	7.885164	.0671889
.5	125.3	7510.639573	.0868718	8.163103	.0833037
.6	127	7612.539711	.104246	8.406118	.0991629
.7	127	7612.539711	.121621	8.538381	.114775
.8	126.5	7582.569082	.138995	8.636508	.130146
.9	125.6	7528.62195	.156369	8.705867	.145285
1	124.5	7462.686567	.173744	8.759281	.160198
1.2	121	7252.892166	.208492	8.765065	.189374
1.4	117.5	7043.097764	.243241	8.756269	.217722
1.6	113	6773.362105	.27799	8.656288	.245288
1.75	110	6593.538332	.304051	8.598313	.265476
2.22	100	5994.125757	.385711	8.306126	.326213
2.75	90	5394.713181	.477795	7.972281	.390551
3.37	80	4795.300605	.585516	7.603027	.46091
4.11	70	4195.88803	.714086	7.192115	.53888
4.85	60	3596.475454	.842657	6.62707	.611208
5.95	50	2997.062878	1.033775	6.095351	.709894
6.7	44	2637.415333	1.164083	5.707585	.771997
7.49	40	2397.650303	1.30134	5.517809	.833492
9.5	30	1798.237727	1.650565	4.766346	.974773
12.74	20	1198.825151	2.213494	3.852418	1.167359
15.65	15	899.118864	2.719088	3.343903	1.313479
18.7	13	779.236348	3.249007	3.31098	1.446685
21.25	10	599.412576	3.692053	2.812476	1.54587
25.61	8	479.530061	4.102088	2.496605	1.62965
25.67	3	179.823773	4.46	.981838	1.697449
25.67	0	0	4.46	0	1.697449

X(in)	Y(lbf)	Seng(psi)	Eeng("/*")	Strue(psi) (x 1000)	Etrue("/*")
-------	--------	-----------	------------	------------------------	-------------

TABLE C.4
REDUCED DATA FOR SAMPLE I/3/A

0	36.7	2635.547576	0	2.635548	0
.1	42	3016.157989	.0174977	3.068934	.0173464
.2	44.2	3174.147217	.0349955	3.285228	.034397
.3	46.4	3332.136445	.0524932	3.507051	.0511618
.4	47.2	3389.587074	.0699909	3.626827	.0676502
.5	47.8	3432.675045	.0874887	3.732995	.0838711
.6	48.1	3454.219031	.104986	3.816865	.099833
.7	48.2	3461.400359	.122484	3.885367	.115544
.8	48.2	3461.400359	.139982	3.945934	.131012
.9	48.1	3454.219031	.15748	3.998188	.146245
1	47.9	3439.856373	.174977	4.041753	.161249
1.54	44.7	3210.05386	.269465	4.075051	.238596
1.95	41.7	2994.614004	.341206	4.016394	.293569
2.72	36.7	2635.547576	.475938	3.889906	.389294
3.52	31.7	2276.481149	.61592	3.678612	.479905
4.21	28.2	2025.13465	.736655	3.516959	.551961
4.72	27.2	1953.321364	.825893	3.566556	.602069
5.13	24.7	1773.788151	.897634	3.366	.640608
5.98	21.7	1558.348294	1.046364	3.188949	.716065
6.57	19.2	1378.815081	1.149601	2.963902	.765282
7.71	16.7	1199.281867	1.349075	2.817203	.854022
8.75	13.7	983.842011	1.531052	2.490155	.928635
10.17	11.7	840.21544	1.779519	2.335395	1.022278
13.5	6.7	481.149013	2.362194	1.617716	1.212594
22.06	0	0	3.86	0	1.581038

X(in)	Y(lbf)	Seng(psi)	Eeng("/*")	Strue(psi) (x 1000)	Etrue("/*")
-------	--------	-----------	------------	------------------------	-------------

TABLE C.5
REDUCED DATA FOR SAMPLE I/4/A

0	115	6864.03247	0	6.864032	0
.1	182.5	10892.921093	.0167187	11.075037	.0165805
.2	215	12832.756357	.0334375	13.261852	.0328906
.3	234	13966.813895	.0501562	14.667337	.048939
.4	250	14921.809717	.066875	15.919706	.0647338
.5	262	15638.056584	.0835937	16.9453	.0802831
.6	275	16294.616211	.100312	17.92917	.0955942
.7	277	16533.365167	.117031	18.468286	.110674
.8	279	16652.739644	.13375	18.880044	.125531
.9	279.5	16682.583264	.150469	19.192791	.140169
1	279	16652.739644	.167187	19.43687	.154597
1.1	277.5	16563.208786	.183906	19.609286	.168819
1.2	275	16413.990689	.200625	19.707048	.182842
1.3	270	16115.554494	.217344	19.61817	.196671
2.28	223	13310.254268	.381187	18.383957	.322944
2.63	200	11937.447774	.439703	17.186381	.364437
3.45	175	10445.266802	.576797	16.470064	.455395
4.24	150	8953.08583	.708875	15.299705	.535835
5.23	125	7460.904859	.874391	13.98465	.628284
6.61	100	5968.723887	1.105109	12.564817	.744367
8.35	75	4476.542915	1.396016	10.725867	.873807
10.35	50	2984.361943	1.730391	8.148474	1.004445
12.76	15	895.302583	2.133312	2.805282	1.142091
12.8	0	0	2.14	0	1.144223

X(in)	Y(lbf)	Seng(psi)	Eeng(“/”)	Strue(psi) (x 1000)	Etrue(“/”)
-------	--------	-----------	-----------	------------------------	------------

TABLE C.6
REDUCED DATA FOR SAMPLE I/5/B

0	60	4279.600571	0	4.279601	0
.1	90	6419.400856	.0169738	6.528363	.0168314
.2	100	7132.667618	.0339476	7.374805	.0333841
.3	108	7703.281027	.0509214	8.095543	.0496673
.4	110	7845.934379	.0678952	8.378636	.0656897
.5	111	7917.261056	.0848691	8.589192	.0814593
.6	112	7988.587732	.101843	8.802168	.0969841
.7	112.5	8024.25107	.118817	8.977666	.112272
.8	112.5	8024.25107	.13579	9.113868	.127329
.9	112	7988.587732	.152764	9.208959	.142163
1	110.5	7881.597718	.169738	9.219405	.15678
1.1	109	7774.607703	.186712	9.22622	.171186
2.16	90	6419.400856	.366634	8.772974	.312351
3.1	76	5420.827389	.526188	8.273203	.422773
3.86	66	4707.560628	.655189	7.791903	.503915
4.41	60	4279.600571	.748545	7.483075	.558784
5.5	50	3566.333809	.93356	6.895719	.659363
6.25	44.5	3174.03709	1.060863	6.541256	.723125
7.74	36	2567.760342	1.313773	5.941215	.83888
9.18	30	2139.800285	1.558196	5.474028	.939302
11.12	24	1711.840228	1.887488	4.942918	1.060387
14.7	16	1141.226819	2.49515	3.988759	1.251376
19.66	6	427.960057	3.337051	1.856085	1.467195
20.62	0	0	3.5	0	1.504077

X(in)	Y(lbf)	Seng(psi)	Eeng("/")	Strue(psi) (x 1000)	Etrue("/")
-------	--------	-----------	-----------	------------------------	------------

TABLE C.7
REDUCED DATA FOR SAMPLE I/6/A

0	25	1497.364638	0	1.497365	0
.1	52.5	3144.46574	.0194219	3.205537	.0192357
.2	56.5	3384.044082	.0388438	3.515493	.0381083
.3	59.5	3563.727839	.0582657	3.771371	.0566314
.4	60.3	3611.643507	.0776876	3.892223	.0748176
.5	61	3653.569717	.0971095	4.008366	.0926789
.6	61.1	3659.559176	.116531	4.086013	.110227
.7	61.2	3665.548634	.135953	4.163892	.127472
.8	60.7	3635.601342	.155375	4.200483	.144425
.9	60.1	3599.66459	.174797	4.228875	.161095
1	59.1	3539.770005	.194219	4.22726	.177492
1.1	58.3	3491.854336	.213641	4.237857	.193625
1.42	55	3294.202204	.275791	4.202713	.243566
1.84	50	2994.729276	.357363	4.064934	.305544
2.25	45	2695.256349	.436993	3.873063	.362552
2.58	40	2395.783421	.501085	3.596274	.406188
2.92	35	2096.310494	.567119	3.285168	.449239
3.57	30	1796.837566	.693361	3.042696	.526716
4.31	24	1437.470053	.837083	2.640752	.608179
7.77	15	898.418783	1.509081	2.254205	.919916
11.78	11.7	700.766651	2.287899	2.30405	1.190249
20.99	7.5	449.209391	4.076655	2.280481	1.624653
25.3	5	299.472928	4.913738	1.771005	1.777278
30.79	0	0	5.98	0	1.943049

X(in)	Y(lbf)	Seng(psi)	Eeng("/*")	Strue(psi) (x 1000)	Etrue("/*")
-------	--------	-----------	------------	------------------------	-------------

TABLE C.8
REDUCED DATA FOR SAMPLE I/7/A

X(in)	Y(lbf)	Seng(psi)	Eeng("/*")	Strue(psi) (x 1000)	Etrue("/*")	
0	125	7208.765859	0	7.208766	0	
.1	208	11995.38639	.0167127	12.195862	.0165746	
.2	257	14821.222607	.0334254	15.316628	.0328789	
.3	282	16262.975779	.0501381	17.078371	.0489217	
.4	290	16724.336794	.0668508	17.842373	.0647112	
.5	294	16955.017301	.0835635	18.371838	.0802552	
.6	295	17012.687428	.100276	18.718656	.0955613	
.7	295	17012.687428	.116989	19.002984	.110637	
.8	293	16897.347174	.133702	19.15655	.125488	
.9	291	16782.00692	.150414	19.306262	.140122	
1	287	16551.326413	.167127	19.317501	.154545	
2.34	225	12975.778547	.391077	18.050312	.330079	
3	200	11534.025375	.501381	17.316969	.406385	
3.78	175	10092.272203	.63174	16.467968	.489647	
4.61	150	8650.519031	.770456	15.315362	.571237	
5.75	125	7208.765859	.960981	14.13625	.673445	
7.15	100	5767.012687	1.194959	12.658354	.786163	
9.03	75	4325.259516	1.509157	10.852757	.919947	
11.43	50	2883.506344	1.910262	8.39176	1.068243	
13.6	25	1441.753172	2.272928	4.718755	1.185685	
14.48	0	0	2.42	0	1.229641	

TABLE C.9
REDUCED DATA FOR SAMPLE I/8/B

0	70	4144.46418	0	4.144464	0
.1	120	7104.795737	.0183908	7.235459	.0182237
.2	125	7400.828893	.0367816	7.673043	.0361213
.3	128	7578.448786	.0551724	7.99657	.0537042
.4	129.5	7667.258733	.0735632	8.231287	.0709832
.5	129.8	7685.020722	.091954	8.391689	.0879688
.6	129.8	7685.020722	.110345	8.533023	.104671
.7	129.5	7667.258733	.128736	8.654308	.121098
.8	129	7637.655417	.147126	8.761356	.13726
.9	127.5	7548.845471	.165517	8.79831	.153165
1	126	7460.035524	.183908	8.831996	.168821
1.82	110	6512.729426	.334713	8.692622	.288716
3.06	86	5091.770278	.562759	7.957208	.446453
3.47	80	4736.530491	.638161	7.759199	.493574
4.37	67.7	4008.288928	.803678	7.229663	.589828
5.07	60	3552.397869	.932414	6.864703	.65877
5.96	52	3078.744819	1.096092	6.453332	.740075
6.51	47.8	2830.076969	1.197241	6.218362	.787203
7.77	40	2368.265246	1.428966	5.752435	.887465
9.44	32.5	1924.215512	1.736092	5.264831	1.006531
10.87	28	1657.785672	1.99908	4.971833	1.098306
14.62	20	1184.132623	2.688736	4.367952	1.305284
17.27	16	947.306098	3.176092	3.956037	1.429376
25.11	10	592.066311	4.617931	3.326188	1.725963
30.42	8	473.653049	5.594483	3.123497	1.886233
38.85	5	296.033156	7.144828	2.411139	2.097383
52.2	0	0	9.6	0	2.360854

X(in)	Y(lbf)	Seng(psi)	Eeng("/*")	Strue(psi) (x 1000)	Etrue("/*")
-------	--------	-----------	------------	------------------------	-------------

TABLE C.10
REDUCED DATA FOR SAMPLE I/9/A

X(in)	Y(lbf)	Seng(psi)	Eeng("/*")	Strue(psi) (x 1000)	Etrue("/*")
0	20	1137.980085	0	1.13798	0
.1	40	2275.960171	.0182191	2.317426	.0180552
.2	45	2560.455192	.0364383	2.653754	.0357901
.3	47.7	2714.082504	.0546574	2.862427	.053216
.4	50	2844.950213	.0728766	3.05228	.0703434
.5	51	2901.849218	.0910957	3.166195	.0871824
.6	52	2958.748222	.109315	3.282183	.103743
.7	52.5	2987.197724	.127534	3.368167	.120033
.8	52.8	3004.267425	.145753	3.442149	.136062
.9	52.8	3004.267425	.163972	3.496884	.151839
1	52.7	2998.577525	.182191	3.544893	.16737
1.1	52.6	2992.887624	.200411	3.592694	.182664
1.2	52.3	2975.817923	.21863	3.62642	.197727
1.6	50	2844.950213	.291506	3.674271	.255809
2.3	44	2503.556188	.41904	3.552647	.349981
2.95	38	2162.162162	.537465	3.324248	.430155
3.73	32	1820.768137	.679574	3.058115	.51854
4.57	27	1536.273115	.832615	2.815397	.605744
5.27	23.3	1325.746799	.960149	2.598661	.67302
6.23	20	1137.980085	1.135053	2.429647	.758491
7.75	16	910.384068	1.411984	2.195831	.880449
9.42	13	739.687055	1.716243	2.00917	.99925
10.99	11	625.889047	2.002284	1.879097	1.099373
13.81	8.3	472.261735	2.516064	1.660502	1.257342
17.53	6	341.394026	3.193816	1.431744	1.433611
24.55	3.3	187.766714	4.4728	1.02761	1.69979
30.57	2	113.798009	5.569592	.747606	1.882452
38.97	0	0	7.1	0	2.091864

LIST OF REFERENCES

1. Kalpakjian, S., Manufacturing Processes for Engineering Materials, p. 153, Addison-Wesley Co., 1984.
2. Askelund, D.R., The Science and Engineering of Materials, p. 313, PWS Publishers, 1984.
3. Quist, W.E, Narayanan, G.H., Wingert, A.L., "Aluminum-Lithium Alloys for Aircraft Structure--An Overview," Aluminum-Lithium Alloys II, Sanders, T.H., and Starke, E.A., eds., pp. 313-323, The Metallurgical Society of AIME, 1984.
4. Lamping, B., "Short Reports: Al-Li forgings Tested," Materials Engineering, pp. 57-58, September 1986.
5. Hunt, M., "New Frontiers in Superlightweight Alloys," Materials Engineering, pp. 29-32, August 1988.
6. Kubel, E.J., "Al-Li Alloys: New Hope for Weight Watchers," Materials Engineering, pp. 41-44, April 1985.
7. Parson, N.C., and Sheppard, T., "Extrusion Processing of Al-Mg-Li Alloys," Aluminum-Lithium Alloys III, Baker, C., Gregson, P.J., Harris, S.J., and Peel, C.J., eds., pp. 222-232, The Institute of Metals, 1986.
8. Shoji, Y., Yoshida, H., Uno, T., Baba, Y., Kamada, K., "Development of Al-Mg-Li Alloys for Fusion Reactor," Engineering Abstracts, p. 406, 1986-004869, Keikinzoku, V. 35, N. 4, April 1985, pp. 197-202.
9. Shoji, Y., Yoshida, H., Uno, T., Baba, Y., Kamada, K., "Development of Al-Mg-Li Alloys for Fusion Reactor," Engineering Abstracts, p. 406, 1986-004870, Sumitomo Keikinzoku Giho, V. 26, N.2, April 1985, pp. 61-67.
10. Harris, S.J., Noble, B., Dinsdale, K., "Effect of Composition and Heat Treatment on Strength and Fracture Characteristics of Al-Mg-Li Alloys," Aluminum-Lithium Alloys II, Starke, E.A., Sanders, T.H., eds., The Metallurgical Society of AIME, 1984.
11. East, W.R., "Superplastic Forming for Tomorrow's Metal Manufacturing," Materials Engineering, pp. 37-40, April 1988.

12. Arieli, A., Vastava, R.B., "Superplastic Forming Technology Applications to Fighter Aircraft," Superplastic Forming, Agrawal, S.P., ed., pp. 70-75, The American Society for Metals, 1985.
13. Barnes, A.J., "Advances in Superplastic Aluminum Forming," Superplasticity in Aerospace, Heikkenen, H.C., and McNelley, T.R., eds., pp. 301-314, AIME Conference Proceedings, January, 25-28, 1988.
14. Comley, P.N., "Putting Parts onto Planes--SPF Comes of Age," Superplasticity in Aerospace, Heikkenen, H.C., and McNelley, T.R., eds., pp. 361-370, AIME Conference Proceedings, January 26-28, 1988.
15. "Materials for the Products of Tomorrow," Materials Engineering, p. 69, May 1982.
16. Lavoie, F.J., "Materials in Aerospace," Materials Engineering, pp. 27-33, September 1986.
17. Bampton, C., McQuilkin, F., Stacher, G., "Superplastic Forming Applications to Bomber Aircraft," Superplastic Forming, Agrawal, S.P., ed., pp. 78-83, The American Society for Metals, 1985.
18. Salama, A.A., Analysis of Grain Refinement and Superplasticity in Aluminum-Magnesium Alloys, Doctoral Thesis, Naval Postgraduate School, Monterey, California, December 1987.
19. Oster, S.B., Effect of Thermomechanical Processing on the Elevated Temperature Behavior of Lithium-Containing High-Mg. Al-Mg Alloys, Master's Thesis, Naval Postgraduate School, Monterey, California, June 1986.
20. Sanchez, B.W., Processing and Superplasticity in Lithium Containing Al-Mg Alloys, Master's Thesis, Naval Postgraduate School, Monterey, California, March 1987.
21. Ferris, W.F., The Age Hardening Response of Thermomechanically Processed Al-Mg-Li Alloys, Master's Thesis, Naval Postgraduate School, Monterey, California, December 1987.
22. Munro, I.G., Optimizing Superplasticity in Lithium Containing Aluminum-Magnesium Alloys, Master's Thesis, Naval Postgraduate School, Monterey, California, December 1987.
23. Hansen, M., Constitution of Binary Alloys, 2nd. ed., pp. 105-109, McGraw-Hill, 1958.

24. Mondolfo, L.F., Aluminum Alloys: Structure and Properties, pp. 806-819, Butterworths, 1976.
25. Lee, E.W., and McNelley, T.R., "Microstructure Evolution during Processing and Superplastic Flow in a High Magnesium Al-Mg Alloy," Materials Science and Engineering, V. 93, pp. 45-55, 1987.
26. McNelley, T.R., and Hales, S.J., "Materials Research at NPS," Naval Research Reviews, V. XXXIX, pp. 51-56, One/1987.
27. Fridlyander, A.N., Sandler, V.S., and Nikol'skaya, T.I., "Investigation of the Aging of Aluminum-Magnesium-Lithium Alloys," Phys. Met. Metallog., V. 32, pp. 93-100, 1971.
28. Sanders, T.H., and Starke, E.A., "Overview of the Physical Metallurgy in the Al-Li-X Systems," Aluminum-Lithium Alloys II, Sanders, T.H., and Starke, E.A., eds., pp. 1-15, The Metallurgical Society of AIME, 1984.
29. Sigili, C., and Sanchez, J.M., "Calculation of Phase Equilibrium in Al-Li Alloys," Acta Metallurgica, V. 34, pp. 1021-1028, 1986.
30. Lloyd, D.J., and Moore, D.M., "Aluminum Alloy Design for Superplasticity," Superplastic Forming of Structural Alloys, Paton, N.E., and Hamilton, C.H., eds., pp. 147-169, The Metallurgical Society of AIME, 1983.
31. Gayle, F.W., and Vandersande, J.S., "Composite Precipitates in an Al-Li-Zr Alloy," Scripta Met., V. 18, pp. 473-478, 1984.
32. Hales, S.J., and McNelley, T.R., "Microstructural Evolution by Continuous Recrystallization in a Superplastic Al-Mg Alloy," Acta Metall., V. 36, N. 5, pp. 1299-1239, 1988.
33. Grimes, R., and Butler, R.G., "The Forming Behavior of Commercially Available Superplastic Aluminum Alloys," Superplasticity in Aerospace, Heikkinen, H.C., and McNelley, T.R., eds., pp. 97-114, AIME Conference Proceedings, January 25-28, 1988.
34. Gu, B.P., Mahalingam, K., and Sanders, T.H., "The δ' Particle Size Distribution in a Variety of Al-Li-Zr Systems," Aluminum-Lithium Alloys III, Baker, C., Gregson, P.J., Harris, S.J., and Peel, C.J., eds., pp. 360-368, The Institute of Metals, 1986.

35. Gayle, F.W., and Vander Sande, J.B., "Composite Precipitates in an Al-Li-Zr Alloy," Scripta Met., 18, pp. 473-478, 1984.
36. Dinsdale, K., Harris, S.J., and Noble, B., "Relationship Between Microstructure and Mechanical Properties of Aluminum-Lithium-Magnesium Alloys," Aluminum-Lithium Alloys, Sanders, T.H., and Starke, E.A., eds., pp. 101-118, TMS-AIME, Pennsylvania, 1981.
37. Noble, B., Harris, S.J., and Harlow, K., "Mechanical Properties of Al-Li-Mg Alloys at Elevated Temperatures," Aluminum-Lithium Alloys II, Sanders, T.H., and Starke, E.A., eds., pp. 65-77, The Metallurgical Society of AIME, 1984.
38. Sherby, O.D., and Wadsworth, J., "New Superplastic Materials," Superplasticity in Aerospace, Heikkinen, H.C., and McNelley, T.R., eds., pp. 3-28, AIME Conference Proceedings, January 25-28, 1988.
39. Dieter, G.E., Mechanical Metallurgy, 3rd ed., chap. 8, McGraw-Hill, 1986.
40. Sherby, O.D., Ruano, O.A., "Synthesis and Characteristics of Superplastic Alloys," Superplastic Forming of Structural Alloys, Paton, N.E., and Hamilton, C.H., eds., pp. 241-252, The Metallurgical Society of AIME, 1983.
41. Nix, W.D., "On Some Fundamental Aspects of Superplastic Flow," Superplastic Forming, Agrawal, S.P., ed., pp. 7-12, The American Society for Metals, 1985.
42. Shewmon, P.G., Transformations in Metals, chap. 3, J. Williams Book Co., 1983.
43. Cahn, R.W., "Recovery and Recrystallization," Physical Metallurgy. Part II, 3rd ed., Cahn, R.W., and Haasen, P., eds., chap. 25, Elsevier Pub., 1983.
44. Wert, J.A., "Thermomechanical Processing of Heat Treatable Aluminum Alloys for Grain Size Control," Microstructural Control in Aluminum Alloys, Chia, E.H., and McQueen, H.J., eds., pp. 67-94, The Metallurgical Society for the AIME, 1986.
45. Wert, J.A., "Grain Refinement and Grain Size Control," Superplastic Forming of Structural Alloys, Paton, N.E., and Hamilton, C.H., eds., pp. 69-83, The Metallurgical Society of AIME, 1983.

46. Bampton, C.C., Wert, J.A., and Mahoney, M.W., "Heating Rate Effects on Recrystallized Grain Size in Two Al-Zn-Mg-Cu Alloys," Metallurgical Transactions A, V. 13A, pp. 193-198, February 1982.
47. Nes, E., "Continuous Recrystallization and Grain Growth During Superplastic Flow," Superplasticity, Baudelet, B., and Suery, M., eds., pp. 7.1-7.14, Editions du C.N.R.S., Paris, 1985.
48. Hales, S.J., and McNelley, T.R., "Fine-Grained Superplasticity at 300°C in a Wrought Al-Mg Alloy," Superplasticity in Aerospace, Heikkenen, H.C., and McNelley, T.R., eds., pp. 3-28, AIME Conference Proceedings, 61-76, January, 1988.
49. Hornbogen, E., "Combined Reactions: 1979 Institute of Metals Lecture," Metallurgica Transactions A, V. 10A, pp. 947-972, August 1979.
50. Naval Surface Weapons Center, Silver Springs, Maryland, invoice 010244, November 15, 1985.
51. Anamet Laboratories, Inc., Berkeley, California, laboratory report of January 23, 1986.
52. Wise, J.E., The Influence of Total Strain, Strain Rate and Reheating Time During Warm Rolling on the Superplastic Ductility of an Al-Mg-Zr Alloy, Master's Thesis, Naval Postgraduate School, Monterey, California, March 1987.
53. Spiropoulos, P.T., Thermomechanical Processing of Al Alloy 2090 for Grain Refinement and Superplasticity, Master's Thesis, Naval Postgraduate School, Monterey, California, December 1987.
54. Meyers, M.A., and Chawla, K.K., Mechanical Metallurgy, Chapter. 16, Prentice-Hall, 1984.
55. Metals Handbook, Volume 4: Heat Treating, Ninth Edition, pp. 675-718, American Society for Metals, 1985.
56. Vander Voort, G.F., Metallography, McGraw-Hill, 1984.
57. Beckwith, T.G., Buck, N.L., and Marangoni, R.D., Mechanical Measurements, 3rd ed., Addison-Wesley, 1982.
58. Spiegel, M.R., Statistics, p. 246, Schaum's Outline Series, McGraw-Hill, 1961.

59. Pilling, J., and Ridley, N., "Cavitation in Aluminum Alloys During Superplastic Flow," Superplasticity in Aerospace, Heikkenen, H.C., and McNelley, T.R., eds., pp. K1-F16, AIME Conference Proceedings, January 25-28, 1988.
60. McNelley, T.R., Naval Postgraduate School, Monterey, California, 1988, unpublished research.

INITIAL DISTRIBUTION LIST

	No. Copies
1. Defense Technical Information Center Cameron Station Alexandria, Virginia 22304-6145	2
2. Library, Code 0142 Naval Postgraduate School Monterey, California 93943-5002	2
3. Department Chairman, Code 69Hy Department of Mechanical Engineering Naval Postgraduate School Monterey, California 93943-5000	1
4. Professor T.R. McNelley, Code 69Mc Department of Mechanical Engineering Naval Postgraduate School Monterey, California 93943-5000	5
5. Curricular Officer, Code 34 Department of Naval/Mechanical Engineering Naval Postgraduate School Monterey, California 93943-5000	2
6. Dr. S.J. Hales NASA--Langley Research Center Mail Stop 188A Hampton, Virginia 23655-5225	1
7. Naval Air Systems Command, Code AIR 921 Naval Air Systems Command Headquarters Washington, DC 20361	1
8. Dr. E.W. Lee, Code 6063 Naval Air Development Center Warminster, Pennsylvania 18974	1
9. LT D.F. O'Mara P.O. Box 4153 Middletown, Rhode Island 02840	2